Additive Manufacturing of Ceramic $Li_7La_3Zr_2O_{12}$ Solid Electrolytes for Solid-State Battery Applications

by

Kshiti Patel

A thesis

presented to the University of Waterloo

in fulfillment of the

thesis requirement for the degree of

Master of Applied Science

in

Mechanical & Mechatronics Engineering

Waterloo, Ontario, Canada, 2024

Author's Declaration

I hereby declare that I am the sole author of this thesis. This is a true copy of the thesis, including any required final revisions, as accepted by my examiners.

I understand that my thesis may be made electronically available to the public.

Abstract

Solid-state lithium-ion batteries (SSLIB) are increasingly attracting attention due to their advantageous properties, including enhanced safety, non-flammability, higher energy density, durability, and lightweight design, which are achieved by eliminating the toxic and flammable electrolyte material present in conventional lithium-ion batteries. However, a significant obstacle to the commercialization of SSLIB lies in the processing methods. While electrodes are typically processed similarly for both conventional and solid-state batteries, the processing of thin solid electrolytes presents unique challenges. Inorganic ceramic solid electrolytes, particularly garnet-based Lithium lanthanum zirconium oxide (LLZO) ceramic solid electrolytes, are gaining interest due to their high ionic conductivity and thermal stability.

Additive manufacturing (AM) is a studied fabrication method for processing various materials including ceramics. Direct ink writing (DIW), an extrusion-based AM method, is known for its material versatility, ease of operation, and capability for multi-material printing making it suitable for battery applications. The advantages of using AM for manufacturing batteries, notably ceramic electrolytes, are high freedom of design, increased areal energy density, and volumetric density.

In this thesis, a novel sintering set-up was developed to densify ~150-250 µm thin $Li_{6.4}La_3Zr_{1.4}Ta_{0.6}O_{12}$ (Ta-doped LLZO, LLZTO) ceramic electrolytes prepared via DIW fabrication. The challenges encountered in ink synthesis, DIW printing, and sintering are outlined along with effective solutions. This research aims to investigate these effects on LLZO ceramic solid electrolytes for applications in all-SSLIB.

The ink synthesis and optimization greatly impact the drying properties of the ceramic and processability. The properties of the ink such as viscosity, flowability, and its homogeneity need to be controlled to ensure optimal shear thinning behaviour. A volumetric flow rate model is developed using four different suitable dispensing tips to analyze the flow rate with respect to pressure applied for extrusion. This work uncovers the optimized ink composition consists of a solid loading of 30-35 wt%, 0.35 wt% dispersant (equivalent to 1 wt% concerning the solid loading), a 3:7 solvent ratio, and a 1:1 binder-plasticizer ratio (both at 6.45 wt%) suitable for DIW.

Subsequently, the solid electrolytes undergo sintering at temperatures exceeding 1100℃ to promote particle bonding and form a solid, conductive electrolyte. The properties of the final LLZO ceramic, including density, grain size, and ionic conductivity, are highly dependent on the sintering process. The phase, relative density, and ionic conductivity properties of sintered LLZTO are evaluated using

techniques such as powder x-ray diffraction (XRD), scanning electron microscopy (SEM), and electrochemical impedance spectroscopy (EIS).

Preliminary findings in this thesis highlight the need for refining the processing techniques for fabrication and sintering of ceramic electrolytes to overcome challenges associated with lithium loss at temperatures exceeding 1000℃, sintering conditions, and poor reproducibility. This research thesis identified optimized sintering conditions, and set-up required to address the common sintering challenges to reproduce flat, high density thin solid electrolyte with the desired crystal cubic phase. The sintering results show optimal conditions are de-binding at 700℃ for 12 hours and sintering at 1100℃ for 1.5 hours with 10 wt% excess LiOH. The thin solid electrolytes are sandwiched between graphite and MgO plates within the MgO crucible. The EIS results show a high ionic conductivity comparable to literature findings and commercially available LLZTO ceramic electrolytes.

Keywords: Lithium Lanthanum Zirconium Oxide, LLZO, Garnet, Sintering, Direct Ink Writing, Solid-State Electrolytes, Ceramic Electrolytes.

Acknowledgements

At first, I would like to express my sincerest gratitude to my supervisors, Professor Saeed Maleksaeedi and Professor Mihaela Vlasea, in Department of Mechanical and Mechatronics Engineering. Additionally, I would like to acknowledge Professor Michael Pope of the Department of Chemical Engineering for his invaluable support of this project, and Professor XiaYu Wu in the Mechanical and Mechatronics Engineering department for being a valuable committee member. Thank you all for providing me the chance to conduct this research and offering me valuable suggestions during my study.

Next, I would like to acknowledge the entire team at Multi-Scale Additive Manufacturing (MSAM) Lab and 2D Materials and Electrochemical Devices Lab Group. Thank you for consistently supporting me, my research, and providing such a positive collaborative environment. Love and light to all the amazing hard-working members. Additionally, I would like to thank Cara Kolb PhD, Marianna Uceda PhD, Manyou Sun, Yifan Yang, and Xinmei Yan for supporting this project.

I would also like to express my acknowledgements to Panasonic North America for funding this research project and providing me the opportunity to work on this topic.

Last but not the least, I would like to thank my fiancé, parents, brother, sister-in-law, and friends for their consistent support. Thank you for always keeping me motivated, loved, and happy.

Table of Contents

List of Figures

List of Tables

List of Abbreviations

AM	Additive Manufacturing
BBP	Butyl Benzyl Phthalate
DFT	Density Functional Theory
DIW	Direct Ink Writing
DOD	Drop-on-Demand
DOE	Design of Experiment
DSC	Differential Scanning Calorimetry
EIS	Electrochemical Impedance Spectroscopy
EL	Excess Lithium
FDM	Fused Deposition Modelling
FFF	Fused Filament Fabrication
GO	Graphene Oxide
IJP	Ink Jet Printing
LCO	Lithium Cobalt Oxide
LFP	Lithium Iron Phosphate Oxide
Li	Lithium
Li-ion	Lithium-Ion
LIB	Lithium-Ion Battery
LLZO	Lithium Lanthanum Zirconium Oxide
LLZTO	Ta doped Lithium Lanthanum Zirconium Oxide
LMO	Lithium Manganese Oxide
LMR-K	Lithium Potassium Manganese Nickel Cobalt Oxide
LTO	Lithium Titanium Oxide
LZO	Lanthanum Zirconium Oxide
MFO	Menhaden Fish Oil
MgO	Magnesium Oxide
nB	n-Butanol
PBF-LB/P	Laser-based Powder Bed Fusion
PET	Polyethylene Terephthalate
PVB	Polyvinyl Butyral
PVDF	Polyvinylidene Fluoride
SE	Solid Electrolyte
SEM	Scanning Electron Microscopy
SLA	Stereolithography
SOP	Standard Operating Procedure

SSB	Solid-State Batteries
SSE	Solid State Electrolyte
SSLIB	Solid-State Lithium-Ion Batteries
Ta-LLZO	Ta doped- Lithium Lanthanum Zirconium Oxide
TGA	Thermogravimetric Analysis
wt%	Weight Percentage
XRD	X-Ray Diffraction
αT	Alpha-Terpineol

Chapter 1 Introduction

In this chapter, the motivation of the research project presented in this thesis is briefly introduced. The research challenges are outlined with research process objectives and goals. Finally, the structure of the thesis is described.

1.1 Motivation

In today's world, batteries are essential for numerous applications, including consumer electronics, e-vehicles, renewable energy storage, and smart home devices [1,2]. Presently, lead-acid, nickel-metal hydride, sodium-ion, and lithium-ion batteries are commercially available, however, they do not satisfy the stringent increasing demands of portable electronics, electric vehicles, and grid energy storage systems [1]. It is critical for batteries to have higher energy densities, longer cycle lives, and enhanced safety at a reasonable cost of production [1]. In recent decades, lithium-ion (Li-ion) batteries have been continuously researched to improve properties to meet these increasing demands.

Since the development of the Li-ion battery, liquid electrolytes have been used in providing excellent wetting of electrode surfaces and high conductivity but have disadvantages such as inadequate electrochemical and thermal stabilities, and safety concerns [1]. In more recent research, replacing a liquid electrolyte with a solid-electrolyte separator has been favoured to overcome such disadvantages of the liquid electrolyte and develop new battery chemistries [1,3].

Garnet-based $Li_7La_3Zr_2O_{12}$ (LLZO) ceramic solid electrolyte (SE) has gained particular interest due to its good Li-ion conductivity, wide electrochemical stability window, and excellent stability against Li metal [4]. One of the primary obstacles hindering the widespread adoption of ceramic SE is the difficulty of reproducing and handling thin, high-density electrolytes with the desired crystal phase through high-temperature sintering. The manufacturing process used for the SE significantly impacts the ability to achieve the desired SE density and geometric freedom.

Additive manufacturing (AM) emerges as a promising processing route to manufacture SE offering design flexibility, customization, and the potential for enhanced performance. AM of ceramic materials has been studied for many years providing new geometries for various applications. Similarly, a ceramic SE can be printed using similar processing route to enable a novel fabrication method with more flexible and customizable designs [5–10]. Direct ink writing (DIW) or extrusion-based AM can play a promising role in optimizing the manufacturing process, ultimately leading to superior results in the development of smaller, lighter, and wearable designs of solid-state batteries [11–14].

The entire research project includes formulation of ceramic electrolyte ink, DIW printing, sintering, and material characterization of garnet-type SE.

1.2 Research Challenge

Current processing of ceramic solid-electrolytes has challenges in high-temperature sintering, cracking during shrinkage, achieving controlled grain boundaries essential for optimizing processing, achieving cubic crystal phase, and poor reproducibility in manufacturing.

DIW is a promising technique to manufacture batteries due to its multi-material printing capability, and material diversity suitable for active battery materials. In recent years, it has gained attention to successfully manufacture 3D-printed electrodes and ceramic electrolyte with enhanced electrochemical properties [14–18]. Despite the promises, processing of thin high-quality ceramic electrolytes has outlined many challenges during coating/printing and sintering stages [19].

The first challenge relies in ink formulation and processing with DIW. The rheological properties of the ink greatly affect the printability of the ink. It is crucial to ensure a completely homogenous ink with the suitable viscosity range is developed for DIW [9]. A large particle size ink or large agglomerates in the ink impedes smooth flow printing adding challenges. The formulation of the ink also directly impacts the drying properties for the ceramic electrolyte, leading to cracking during shrinkage [5]. Thus, the formation of a suitable ink formulation that can be smoothly processed using direct ink writing and does not crack during drying process is the first challenge.

The second challenge is post-processing of the ceramic electrolyte. After successful preparation of electrolyte, sintering of ceramics is critical to ensuring a high-density ceramic electrolyte is formed [19–32]. During this high-temperature sintering process, Li loss is experienced depleting the cubic crystal phase responsible for Li transport further impeding the electrochemical properties [19]. Despite, many research groups reporting successful sintering of LLZO ceramic electrolyte to achieve a high-density part, the poorly controlled sintering process impedes reproducibility [19]. Other processing challenges include sintering conditions and set-ups, limited knowledge between composition and microstructure, and H_2O/CO_2 reactivity [19]. Thus, innovative approaches need to be developed to ensure reliable, and reproducible sintering processes for LLZO ceramic electrolytes.

This thesis aims to address and provide effective solutions to the two major challenges regarding processing thin, high-density LLZO ceramic electrolytes.

1.3 Objectives and Goals

Considering the research challenges outlined in section 1.2, the following objectives are outlined:

Objective 1 – Ceramic Electrolyte Ink Formulation: Develop an optimized methodology for ceramic electrolyte ink formulation, synthesis, and direct ink writing processing. Address printing, drying, and sinterability to prevent cracks (section 4.1).

Objective 2 – LLZO Solid Electrolyte Additive Manufacturing: Demonstrate fabrication of 150-250 µm solid ceramic electrolytes using direct ink writing. Analyze flow behavior with tapered and needle nozzle tips (section 4.2).

Objective 3 – Sintering Parameter Exploration: Investigate sintering parameters (temperature, duration, setup) for high-density (>95%) solid electrolytes with a cubic crystal phase (section 4.3).

Objective 4 – Electrochemical Characterization: Evaluate electrochemical performance, including ionic conductivity (>10^4 S/cm), of the working solid electrolyte (section 4.4).

1.4 Research Steps

The research steps included in this thesis are as follows:

1. Formulation and synthesis of LLZO ceramic electrolyte ink
2. Direct ink writing printing of LLZO ceramic electrolyte
3. De-binding and sintering of LLZO ceramic electrolyte
4. Characterization of final ceramic electrolyte

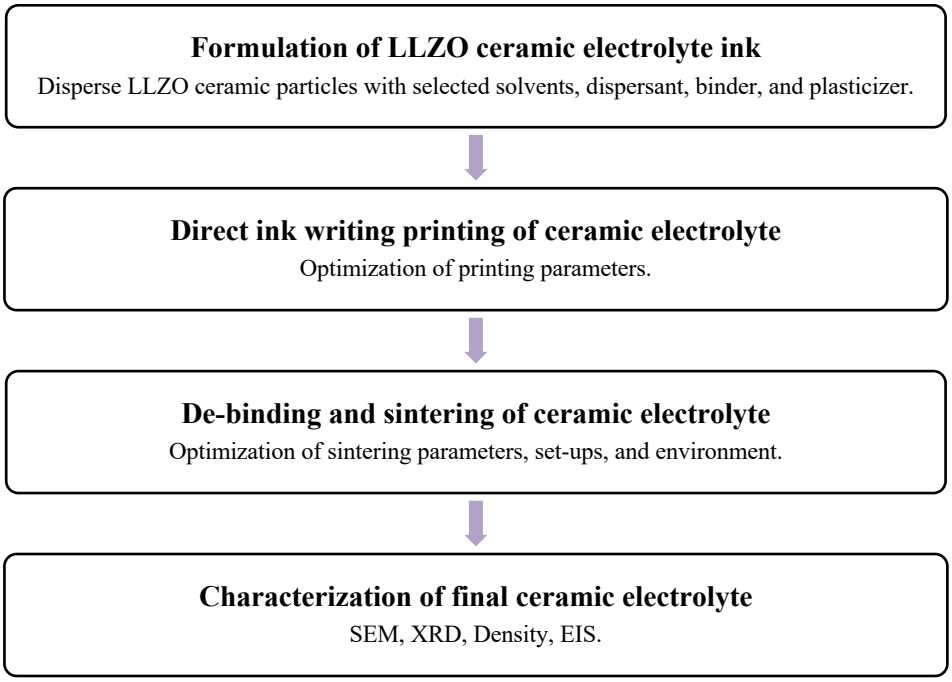

Figure 1: Project flow chart.

1.5 Thesis Layout

This thesis is divided into 6 chapters. Chapter 1 is the general introduction of the project including motivation, challenges and goals, and research steps. Chapter 2 is the state of the art and literature review for the solid-state-lithium-ion-battery, AM of batteries, particle ink synthesis and post-processing sintering of LLZO SE. Chapter 3 details the methodology for the ink synthesis, DIW printing, and sintering procedures applied in this study. The results and discussions for each research step is presented in Chapter 4. The innovative new approach sintering set-up developed and electrochemical results are also described in Chapter 4. Lastly, Chapter 5 presents the summary of the thesis.

Chapter 2 State of the Art & Literature Review

The contents of this chapter provide background knowledge on the Li-ion battery components, additive manufacturing technologies for batteries including direct ink writing, particle ink components and synthesis, and LLZO ceramic electrolyte sintering.

2.1 Significance of Energy Storage in Contemporary Society

Section 2.1 presents a summary of traditional Li-ion batteries, solid-state batteries, and the classification of solid-state electrolytes, as well as highlighting the advantageous characteristics of Li-ion conductive polymer, and inorganic Li-ion conductive ceramic solid electrolyte.

2.1.1 Overview of Conventional Lithium-Ion Batteries

Over the past few decades, Li-ion batteries have drawn a lot of interest due to their use in handheld devices like laptops, tablets, and smart phones. Their exceptional capabilities, in particular energy storage and power, have facilitated the advancement of electronics in modern society. Further investigation into battery cell safety and materials is required as Li-ion battery technology develops [33].

The main components of a Li-ion battery are as presented:

Cathode: positive electrode containing active materials such as mixed oxides.

Anode: negative electrode where Li is deintercalated from during discharging.

Electrolyte: ion-conducting liquid located between two electrodes.

Separator: A porous membrane separating the two electrodes.

2.1.2 Benefits of Solid-State Batteries

While conventional Li-ion batteries have revolutionized various sectors, they face limitations that solid-state batteries (SSB) aim to address. Table 1 outlines the comparative attributes, including energy density, charging capabilities, dimensions, lifespan, durability, and environmentally friendliness, distinguishing of SSB from conventional Li-ion batteries counterparts.

Table 1: Advantages of solid-state batteries.

Feature	Advantage	Ref
Safety	Solid electrolytes are non-flammable, unlike liquid electrolytes in conventional batteries, which can pose a fire hazard if they leak.	[1,19,34,35]
Energy Density	Solid-state batteries have the potential to store significantly more energy per unit volume compared to traditional Li-ion batteries, leading to longer range for electric vehicles and longer life for portable devices.	[1,19,36,37]
Charging	Solid-state batteries may enable faster charging times due to their higher ionic conductivity and reduced internal resistance.	[35,36,38]
Size & Weight	Solid electrolyte replaces the need for a separator requiring less space than liquid electrolyte. Therefore, solid-state batteries can be made smaller than conventional lithium-ion batteries. Additionally, Li metal anode can carry higher energy density while being lighter.	[34,39–42]
Lifespan	Solid-state batteries are expected to have a longer lifespan than conventional Li-ion batteries due to their improved stability and reduced degradation mechanisms.	[37]
Durability	Solid electrolytes in solid-state batteries are generally more robust, making them less susceptible to damage from vibration or shock.	[1,34]
Environmental Impact	The production and disposal of solid-state batteries may be more environmentally friendly compared to traditional batteries due to the elimination of flammable and toxic liquid electrolytes.	[35,37,39,43,44]

Conventional Li-ion batteries have several drawbacks requiring improved design to overcome safety issues associated with a liquid electrolyte which helps transport Li ions to and from cathode and anode. Over time, continuous cycles of charging and discharging diminish the quality of the battery and are frequently accompanied by risk of flammability, electrolyte breakdown, and Li dendrite formation. The development of all-solid-state batteries has shown promise in resolving these issues. The liquid electrolyte is replaced with a solid electrolyte (SE) eliminating chances of leakage, and formation of Li dendrite prone to explosion. SE have demonstrated advantageous properties including greater energy output, better efficiency from easy transfer of Li ions, and minimal wear and tear [3,33].

2.1.3 Classification of Solid-State Batteries

The components of a Li-ion SSB include the anode, cathode, and the SE (Figure 2). The cathode is the positive electrode supplying necessary ions during charging and discharging process. It is critical for

cathode material to have a high ionic conductivity aiding transference of ions across charging and discharging processes. The most used cathode materials in SSB include lithium cobalt oxide (LCO), lithium manganese oxide (LMO), and lithium iron phosphate oxide (LFP) (Figure 3). LCO processes an octahedral arrangement, layered structure suitable for lithiation/delithiation with a high specific energy of about 150 mAh/g. The spinal structure in LMO produces very little resistance during lithiation/delithiation process. Lastly, LFP has an olivine structure which assists the transfer of ions and provides less resistance to the path of ions [33,45].

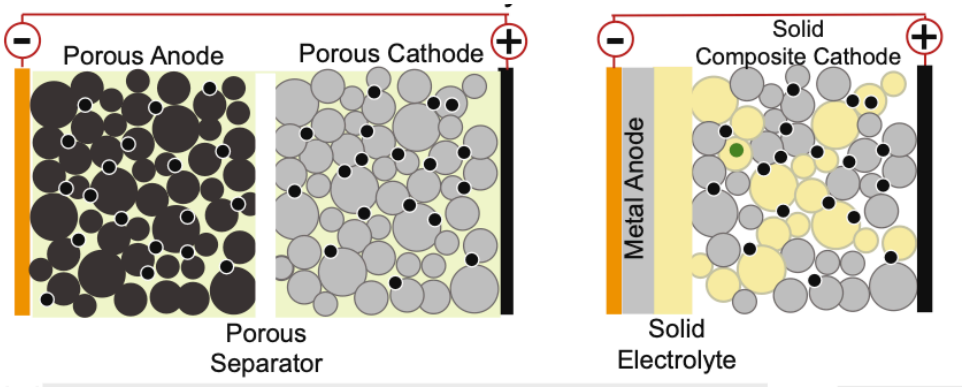

Figure 2: Schematic illustration of conventional Li-ion battery (left) and all SSB (right). Retrieved from [46].

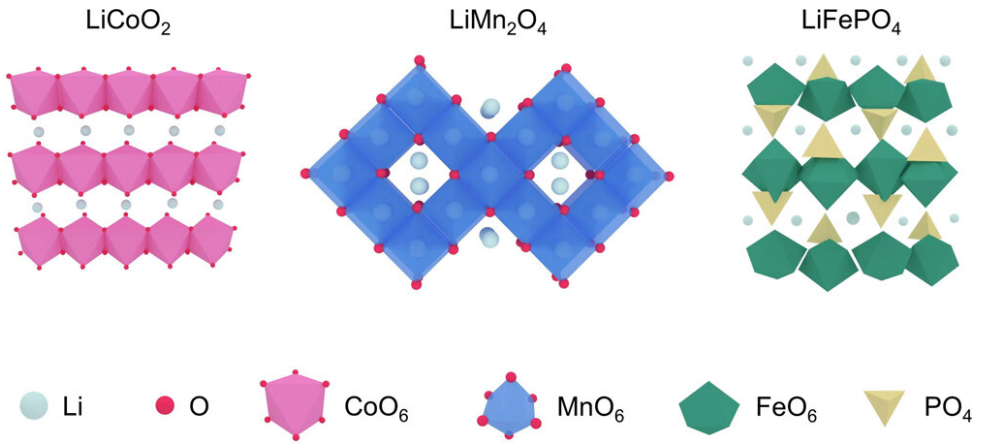

Figure 3: Crystal structure of LCO, LMO, and LPF cathode materials. Retrieved from [47].

The anode is the negative electrode where lithiation takes place during the charging process. It also stores Li/Li^+ to great capacity. Lithium-based metal oxides such as $Li_4T_5O_{12}$ (LTO) are common. The octahedral structure easily integrates Li ions during the lithiation process. It has a low specific energy of 175 mAh/g. Other materials such as carbon- and carbon-based materials, are also good anode materials in SSB [33]. To

boost energy density, the SSB combines a solid-state cathode with a Li metal anode. Recently, many research groups have studied using pure Li leading to a higher energy density (3860 mAh/g) [48].

The SE allows the diffusion of ions between anode and cathode. The performance of the electrolyte is critical to the performance of the solid-state battery. Consequently, great chemical stability, low electronic conductivity, and strong ionic conductivity are necessary for SE. Furthermore, a lightweight solid-state battery with high-cycle life, high energy density, and non-flammability are desirable for microelectronics and electric vehicle applications. The substitution of liquid electrolyte with a SE enables modification of the cell structure alleviating restrictions in architecture and safety [33]. Table 2 shows the advantages and disadvantages of SE.

Table 2: Advantages and disadvantages of solid electrolytes in practice. Data retrieved from [49].

Advantages	Disadvantages
• Decreased wear and tear during operation. • Larger operation window (temperature range up to 200°C).	• Unsuitable performance in low and ambient temperature conditions. • At normal temperature, solid oxide has a high resistance to ionic conductivity.

2.1.4 Promising Features of Solid Electrolytes

Several lithium halides, sulfides, lithium nitride, and oxy-salts crystalline materials are researched as good SE candidates [1,33]. Different types of SE can be used based on the electrode/electrolyte material set-ups: bulk SE and thin SE. The thickness range for bulk SE is in several hundred microns whereas thin SE is in range of several hundred nanometers to several microns [19,33].

The solid-state electrolytes used in Li-ion batteries can be categorized into Li-ion conductive polymers and inorganic Li-ion conductive ceramics [1].

2.1.4.1 Lithium-Ion Conductive Polymer Electrolytes

Dry solid polymer electrolytes and composite polymer electrolytes are the two primary categories into which SE based on polymers can be further categorized. At room temperature, dry polymer systems typically have very low ionic conductivity. In contrast, by adding ceramic fillers to the organic polymer host, composite polymer electrolytes show improved ionic conductivity [1].

2.1.4.2 Inorganic Lithium-Ion Conductive Ceramics

Inorganic SE are promising in providing a high ionic conductivity at room temperature. The main SE being studied are perovskite-type, NASICON-type (sodium supersonic conductor), sulfide-type materials, and

garnet-type. Although SE materials with a perovskite structure, such as $Li_{3x}La_{2/3-x}TiO_3$, have attracted considerable attention, they are found to be unsuitable for use in Li batteries due to reduction of Ti_4^+ on contact with Li metal. NASICON-type, $LiTi(PO_4)_3$, is considered a suitable SE for high-voltage batteries. Sulfide-type SE, LiS-SiS_2, including LISCON (lithium supersonic conductor) demonstrate high Li-ion conductivity although chemical stability is a known challenge [33,50]. Lastly, garnet type, $Li_{7.06}M_3Y_{0.06}Zr_{1.94}O_{12}$ (M=La, Nb, or Ta), are promising SE exhibiting high ionic conductivities at room temperature [1,19–28,40,50–62]. The properties of these SE are shown in radar plots (Figure 4).

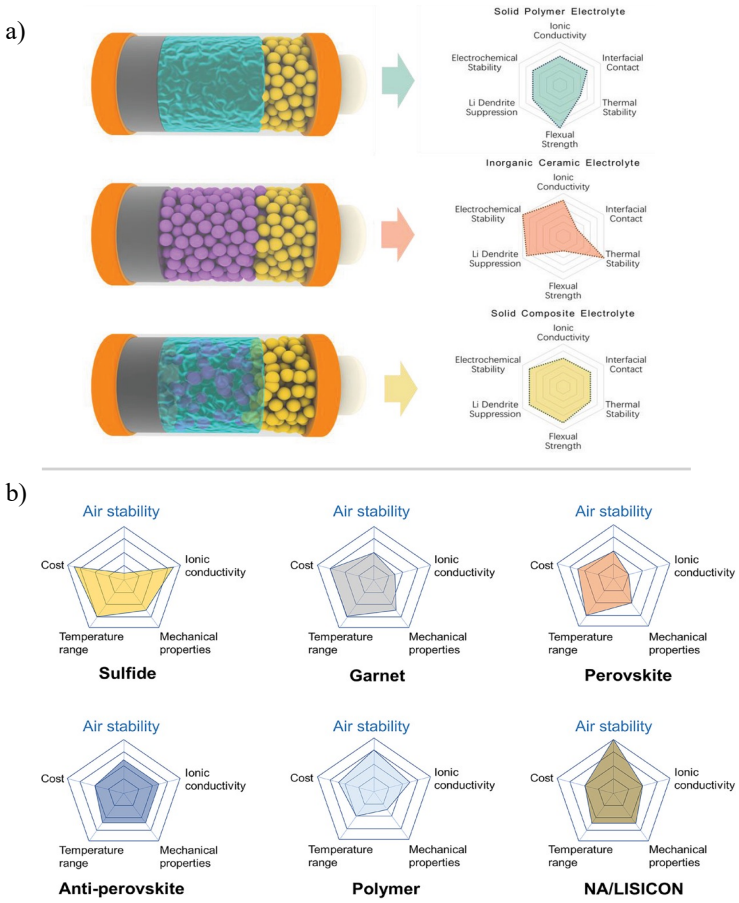

Figure 4: a) Radar plots of properties of liquid electrolyte, solid polymer electrolyte, inorganic ceramic electrolyte, and solid composite electrolyte. Retrieved from [63]; b) Radar plots of properties of different solid-state electrolyte materials including sulfide, garnet, perovskite, anti-perovskite, polymer, NA/LISICON. Retrieved from [64].

2.1.4.3 Garnet-Type Electrolytes

Garnet-type solid-state electrolytes have a high ionic conductivity (10^{-4} to 10^{-3} S/cm), wide electrochemical window, high density, and mechanical strength. The general chemical formula for garnet material is

$A_3B_3(XO_4)_3$ (A = Ca, Mg, Y; B = Al, Cr, Fe; X = Si, Ge, Al). The A, B and X hold 8, 6, 4 oxygen-coordinated cation sites respectively. This garnet can be filled with Li to become a Li-rich garnet. This garnet crystallizes in cubic structure with space group Ia3-d. Increasing Li content in solid-state electrolytes can improve electrochemical performance. $Li_7La_3Zr_2O_{12}$ (LLZO) garnet structure made of ZrO_6 octahedron and LaO_8 dodecahedron and tetragonal and cubic crystal structures (Figure 5). The cubic LLZO structure has the highest ionic conductivity ($3x10^{-4}$ S/cm) and lowest activation energy (0.3 eV) [3,65].

In literature, it is made evident the synthesis of LLZO with desired properties is a challenge. Therefore, studying and understanding the interfacial stability is important [66]. Stoichiometric LLZO with a tetragonal crystal structure at room temperature has a significantly lower ionic conductivity (~10^{-6} S/cm) [1]. Since dopants enhance the degree of vacancy disorder within the Li sublattice, they can be employed to stabilize the cubic crystal structure by creating paths for Li^+ diffusion and increasing conductivity. The concentration of dopants can be varied depending on dopant choice and dopant substitution in lattice to yield the highest conductivity. Typically, 0.4-0.6 per LLZO formula unit is used [65,67,68]. The selected dopants may be substituted on the Li, La, or the Zr site. Depending on the choice of dopants (Al, Ta, Ga, Fe, Nb, Sb etc.), the dopants will occupy either one of the sites to create a cubic structure as shown in Figure 6 [3,53,67,69]. Extensive research has been conducted regarding this topic including density functional theory (DFT) calculations to suggest accurate concentration range for Li vacancy and the effects of dopants in the phase transition. However, this is beyond the scope of this work.

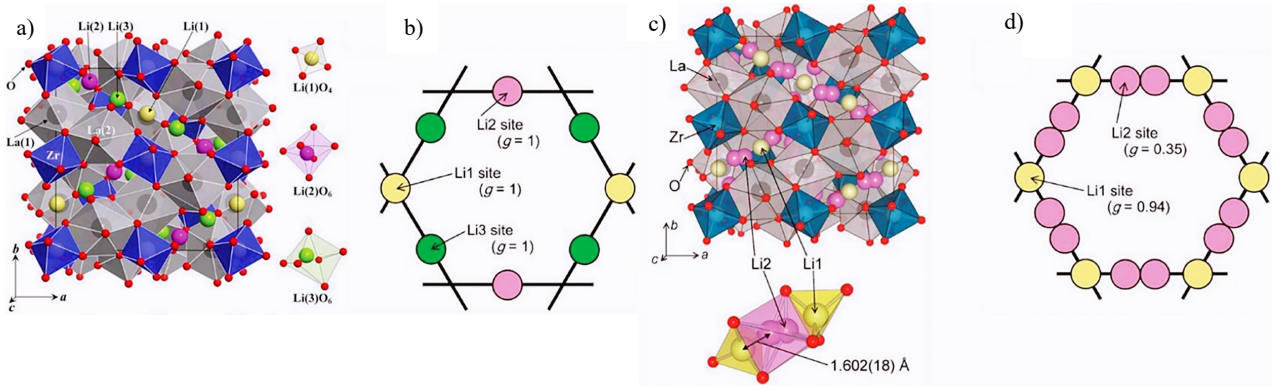

Figure 5: Crystal structure and Li atom loop structures of a,b) tetragonal and c,d) cubic LLZO. Retrieved from [3].

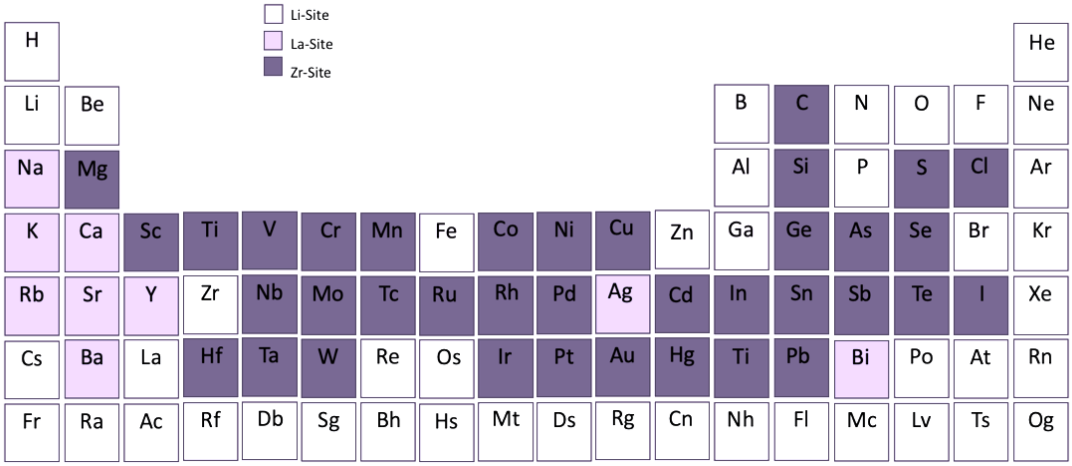

Figure 6: Dopant Stability in LLZO Garnet. Recreated from [70].

2.1.5 Evaluating the Role of Electrolyte Thickness in Solid-State Electrolytes

In oxide-based SSBs, employing thin electrolytes approaching the thickness range of separators in LIB (~20 μm) can enhance battery performance and functionality by reducing internal resistance, improving interfacial contact between electrolyte and cathode, and increasing energy density. However, reducing the thickness to less than 200 μm exacerbates the mechanical challenges associated with ceramic electrolytes. Techniques such as spin coating, sputtering, and physical vapor deposition, through wet-chemical and vacuum-based methods, are used to achieve film thicknesses of up to 10 μm. Further research, spanning approximately ten years, is necessary to comprehensively grasp the chemistry, deposition processes, and characterization of ceramic oxide films before they can be commercially viable [19,34]. Furthermore, reducing the thickness of LLZO electrolytes results in a higher surface area to volume ratio, leading to increased Li loss at sintering temperatures surpassing 1000℃. Further analysis on this phenomenon is explained in 2.4 Sintering of LLZO & Challenges.

2.2 Manufacturing of Inorganic Solid-State Batteries

Section 2.2 presents a summary of conventional manufacturing of batteries, and critical analysis for state-of-the-art additive manufacturing technologies for batteries including direct ink writing, fused filament deposition, and inkjet printing.

2.2.1 Conventional Manufacturing of Batteries

The fabrication of conventional Li-ion batteries typically involves a complex series of steps. This includes synthesizing electrode slurries, casting them onto current collectors, and then filling liquid electrolyte

between the electrodes. To facilitate mass production of Li-ion batteries, significant research has been dedicated to refining processes such as slurry mixing, coating, drying, calendaring, slitting, vacuum drying, jelly roll fabrication, welding, packaging, and electrolyte filling [71]. Typically, electrode fabrication for solid-state batteries involves similar coating processes as those used in conventional batteries. SE are often produced through methods such as powder pressing, chemical vapor deposition, sputtering, aerosol deposition, and additive manufacturing [3,18,19,71,72].

2.2.2 Additive Manufacturing of Batteries

Additive manufacturing (AM), or 3D printing, is a growingly popular technique with uses in a variety of sectors, including the automobile, aerospace, food, and especially the battery business. The demand for energy is predicted to increase globally in the next years (50% between 2018 and 2050), while major industrial sectors including manufacturing, refining, mining, and building are expected to increase more than 30% energy usage since 2017 [16].

AM technology is capable of quickly creating geometrically complex designs utilizing an inventive layer-by-layer fabrication process that meets new unique needs for wearable and flexible electronics [17,73]. This cutting-edge technology also can design freeform, boost areal energy density (amount of energy stored per unite of area), and decrease material waste by removing machining processes [16,17,73–76].

Table 3: Advantages of 3D-Printed Batteries. Data retrieved from [75].

Feature	**Advantages**
Design Freedom	Much-enhanced design freedom in micron-sized dimensions and able to fabricate complex architectures of almost any desired shapes
Areal Energy Density	Higher-areal-loading densities lead to higher areal energy densities and high-aspect ratio of 3D electrodes
Areal Volumetric Density	Higher-areal-loading densities lead to higher areal volumetric densities and high-aspect ratio of 3D electrodes
Power Density	Shorter ion or electron diffusion pathways of 3D-structural electrodes lead to higher power density
Manufacturing Cost	3D printing can dramatically reduce material wastage and save production time by eliminating assembly and packaging steps

The ability to fabricate a wide range of materials, including metals, ceramics, glass, and polymer materials, is provided by several AM processes. The 3D printing technologies are classified into seven categories by the American Society for Testing and Materials:

(1) Material Extrusion (direct ink writing, fused deposition modelling)
(2) Vat photopolymerization (stereolithography, digital light processing, two photon lithography)
(3) Material jetting (inkjet printing, aerosol jet printing)
(4) Powder bed fusion
(5) Sheet lamination
(6) Binder jetting
(7) Directed energy deposition

However, each of these methods has unique technological benefits and drawbacks not compatible with manufacturing a customized battery [15,17,46,73,74,77]. According to a review paper, the top-performing printing methods for cathode, anode, and electrolytes are direct ink writing, fused filament fabrication, and ink jet printing [75]. Therefore, the following sections summarize AM of batteries using these additive manufacturing methods.

2.2.2.1 Direct Ink Writing

Direct ink writing (DIW) also known as robocasting is an extrusion-based deposition technique that used a viscoelastic ink for fabrication. A typical configuration includes a nozzle with regulated pressure and a 2-axis plane movement in which the printhead moves in the z-direction can extrude the intended 3D architecture. The printed resolution can be altered by changing the nozzle diameter and the applied pressure [17,75,78]. The process parameters of DIW include nozzle diameter, geometry, inclination, and material. Additionally, the extrusion pressure, layer thickness, nozzle-substrate distance, and substrate temperature are also process parameters to consider.

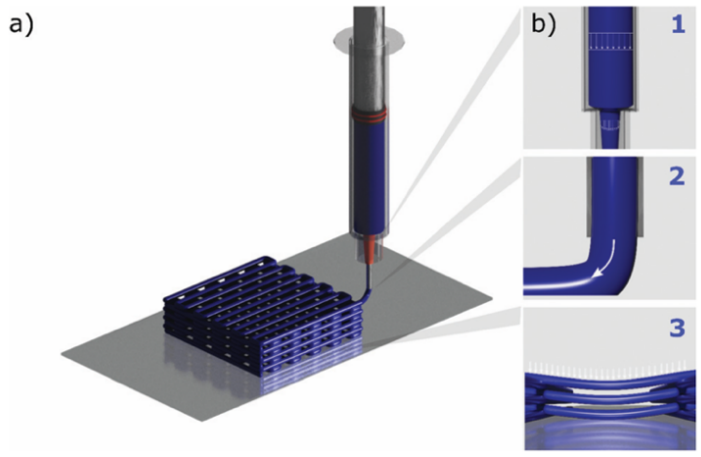

Figure 7: a) and b) Schematic showing main steps of printing process. 1) Flow of ink inside syringe barrel and nozzle; 2) ejection of ink through nozzle; 3) deposition onto substrate to form self-standing structure. Retrieved from [79].

To create pastes with a ceramic foundation, Joseph Cesarani and colleagues at Sandia National Laboratories developed this method in the year 1997. Since then, several DIW bedded printing methods, such as robocasting, micro-pen writing, and fused deposition, have been developed [80]. The prepared gel or ceramic-based viscosity inks are extruded directly from a nozzle in the form of continuous filament. This deposition process is divided into three steps as shown in the Figure 7: (1) flow of ink through syringe and printing nozzle; (2) ejection of ink from nozzle and (3) deposition of ink onto substrate of choice.

For the inks to flow smoothly, these inks must have good shear-thinning behaviour. To ensure ink extrudability, shear-thinning behaviour entails reducing viscosity with increasing shear rate. The desired ink viscosity for DIW application is 10^{-1} to 10^{3} Pa s. To maintain its shape after deposition, ink must change from a shear-thinning liquid to a solid-like material as it is ejected from the nozzle. Many yield stress fluids exhibit elastic or viscoelastic solid behaviour when subjected to a yield stress threshold. When this yield stress threshold is exceeded, the ink can flow [17,75,79–81]. The ideal yield-stress ink has features that depend on immediate rate, but when thixotropic inks are used, these properties can also be modified by shear history. The maximum shar rate (γ; s^{-1}) is calculated by using the following equation where Q (mm^3/s) is the volumetric flow rare, and r (mm) is the nozzle diameter [82].

$$\gamma_{max} = \frac{4Q}{\pi r^3} \tag{1}$$

Understanding the ink's characteristics, particularly its rheological characteristics, is crucial. There are several mathematical models proposed to investigate printability of inks. One of the most common is the Herschel-Bulkey model proposed below:

$$\tau = \tau_y + K\gamma^n \tag{2}$$

where τ (Pa) is the shear stress, K (Pa s) the viscosity parameter, n the flow index and τ_y (Pa) yield stress. The shear-thinning behaviour has n < 1 whereas shear thickening behaviour if n > 1. The shear rate profile and pressure gradient necessary to print ceramic inks can be predicted using this model [79,82]. The loss modulus (G'') and storage modulus (G') represent the ink viscous and elastic behaviour. The ratio of between loss and storage modulus define the viscoelasticity of the ink [82]. Figure 8 demonstrated how the Hershel-Bulkey equation is interpreted on a shear rate vs. shear stress plot to interpret shear-thinning, shear-thickening, and Bingham plastic behaviour.

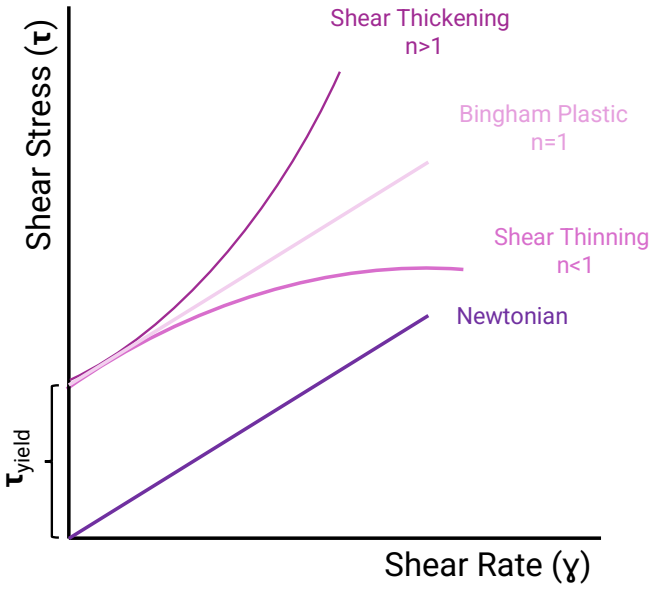

Figure 8: Plot demonstrating shear-thinning, shear-thickening, Newtonian and Bingham plastic behaviour.

The characterization of the rheology parameters can be done by using a rotational rheometer as show in Figure 9.

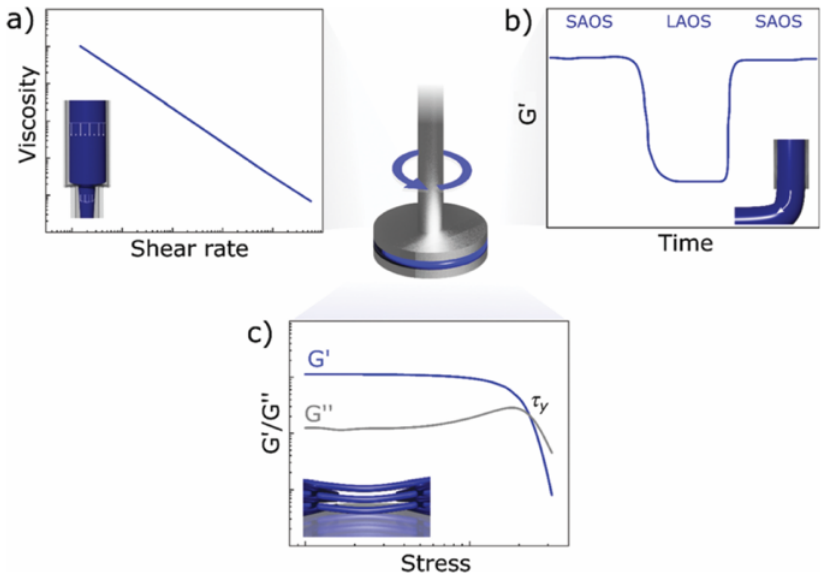

Figure 9: Schematic diagram showing the ideal rheology of a printable ink a) flow curve with highly shear-thinning behaviour; b) rapid recovery of elastic modulus; c) solid-like behaviour below yield stress. Retrieved from [79].

Nozzle Diameter

An important analysis in DIW processing involves examining how process parameters and ink rheology affect extruding filament. One of the most important factors is the nozzle diameter since it influences the printed filament's shape, form retention, and line width. The nozzle, which comes in a variety of nozzle diameters commercially, allows the ink to flow under shear stress. The shear-thinning feature of ink increases as the nozzle diameter decreases distorting the contour of the structure. Furthermore, the probability of clogging in the nozzle increases as the nozzle diameter decreases. Commercially, two different types of tips are available with varying nozzle diameters, the needle and tapered tip (Figure 10). Concave or convex nozzles at the needle tip, affects the extruding swell impact. In comparison to convex nozzles, concave nozzles have a lesser extruding swell impact. However, the tapered nozzle has possibility of filament diameter modulation [80].

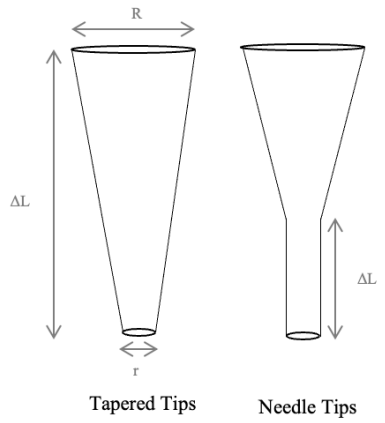

Figure 10: Schematic diagram of tapered and needle tip geometries.

Extrusion Pressure

The extrusion pressure is another critical process parameter and influences the rate/flow of the extrusion. As the extrusion pressure increases, the ink flow increases as well as the increase in shearing of ink that decreases the viscosity of the ink [80].

Extrusion Flow Rate

Excess material can be deposited because extrusion pressure affects extrusion flow rate; this needs to be controlled through line speed and moderate extrusion rate. By doing this, filament breakdown in the printed lines will be lessened. As opposed to a high extrusion rate, a low extrusion rate can produce continuous filament with a greater viscosity ink and fewer pores. With a higher extrusion rate, the filament will become increasingly thinner overall because the extrusion rate is correlated with the ink's shear-thinning property [80].

Nozzle-Substrate Distance

The last critical process parameter of DIW is the nozzle substrate distance. If the nozzle – substrate height is greater than the height of filament layer, the ink will not extrude in a confined line as expected and is more prone to being forced in other directions. On the contrary if the nozzle-substrate height is too small, the nozzle tip will drag the ink or filament while printing [80].

Layer Thickness

The layer thickness or filament width is frequently associated with speed, pressure, and temperature. Illustrations of these trends are shown in Figure 11 below.

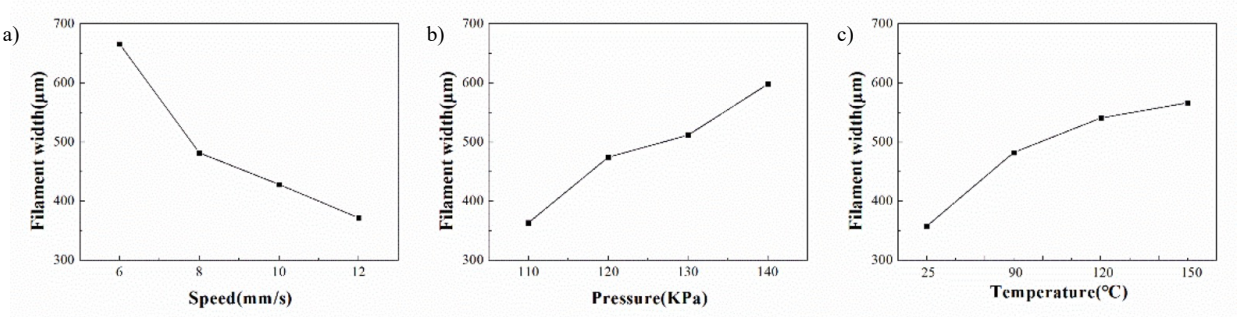

Figure 11: Trend plot of filament width with respect to a) speed, b) pressure, and c) temperature. Retrieved from [83].

In summary, DIW has advantages in material diversity of ink synthesis, high printing throughput, easy operation and relatively affordable cost. In the past decade or so, DIW has proved to be a feasible method to additive manufacture components of the battery such as anode, cathode and polymer and ceramic electrolytes.

In 2016, Fu Kun et al. demonstrated DIW of graphene oxide-based electrode inks using a Benchtop Robot Fisnar F4200n printer to print prepared anode and cathode ink in an inter-digited pattern on a glass substrate (Figure 12). The line speed of printing was set to 5 mm/s with 60 psi nozzle pressure. The thickness of electrodes can be increased by printing more layers on the glass substrate with each layer thickness measured to be 0.18 mm. Up to 18 layers were printing providing an overall thickness of 3.24 mm for electrodes. The printed electrode inks were further freeze-dried to remove solvent and annealed at 600℃ for 2 hours in argon/hydrogen gas before depositing the composite electrolyte ink between the printed anodes. This was done at the same 5 mm/s line speed with 60 psi nozzle pressure [84]. The schematic of printing is shown in which achieves a battery of 3 mm by 7 mm size.

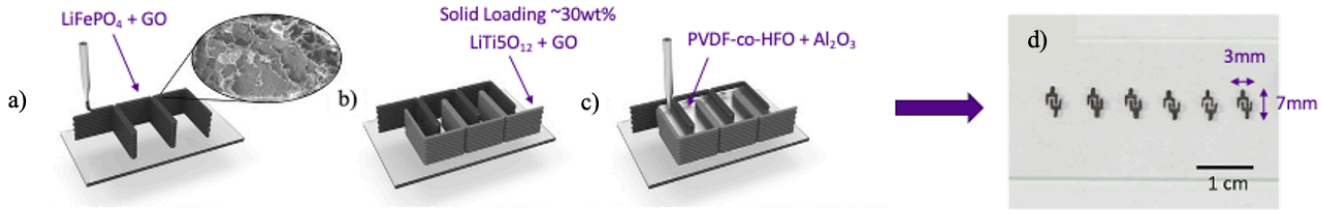

Figure 12: a) Printing LFP+GO anode ink; b) Printing LTO+GO cathode ink; c) Printing composite electrolyte; d) Final printed Li-ion batteries. Retrieved from [84].

In 2018, McOwen et al. demonstrated the first garnet LLZO solid-state-electrolyte for an all-solid-state battery printed via DIW [14]. In this study, two types of ink were synthesized, conformal and self-supporting inks. Various binders, and solvents were used to alter rheological properties of these inks. The conformal ink has a lower viscosity (1090 cP) with Newtonian behaviour indicating the printed ink will not retain its shape under high shear stress whereas the self-supporting ink has a higher viscosity (1500 cP) with Bingham plastic behaviour indicating the printed ink will retain its shape under high shear stress (Figure 13a). The solvent fraction can be adjusted to either increase or decrease the viscosity of the ink (Figure 13b) [14].

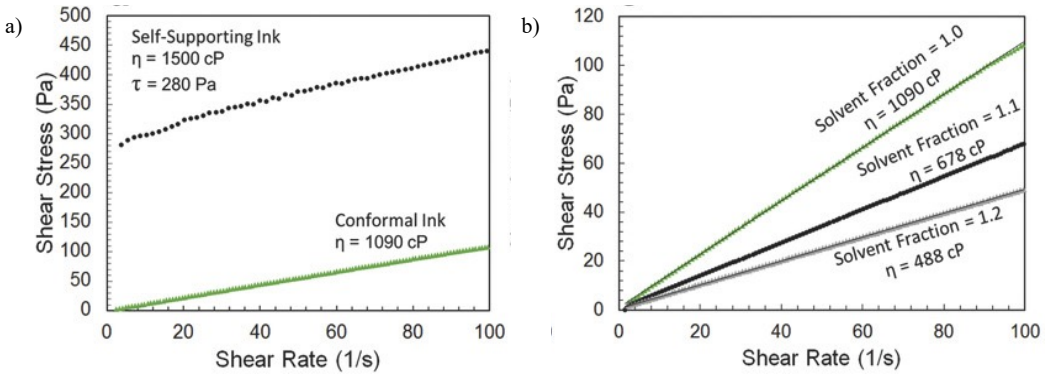

Figure 13: a) Shear rate vs. shear stress plot for conformal and self-supporting ink; b) shear rate vs. shear stress plot for various solvent fractions in conformal ink. Retrieved from [14].

The prepared conformal and self-supporting inks were printed using the nScryt 3Dn-300 printer with SmartPumps and 12.5, 25, or 125 µm diameter nozzles. While printing, the stage was heated to 30-35°C to facilitate solvent drying evenly and reduce stresses caused by drying on the printed part. Lines, grids, and columns patterns were printed on LLZO tape substrate in layers to increase height on both sides of the LLZO tapes before sintering at higher temperature for annealing (unpublished). The sintered scaffold can then be used to create a solid-state battery by filling electrodes (Figure 14) [14].

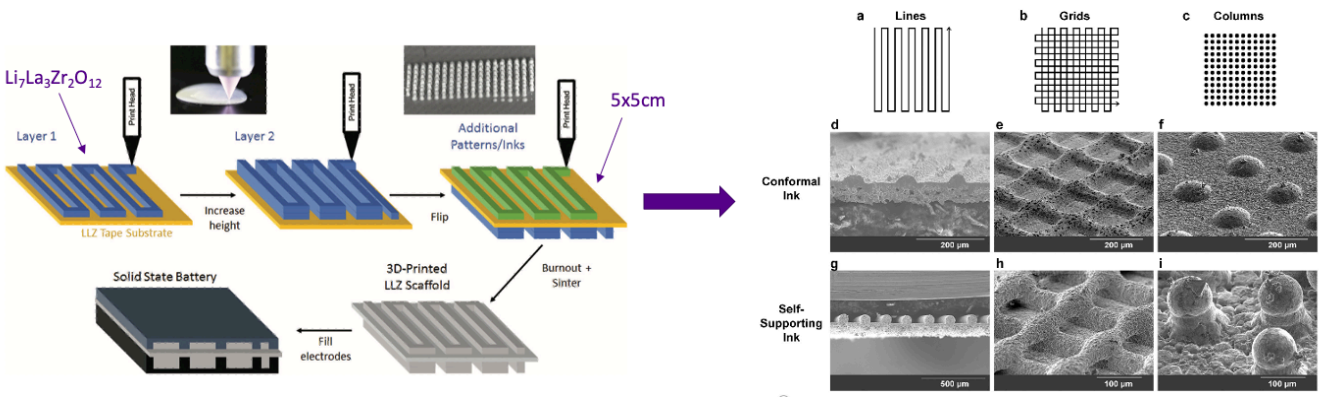

Figure 14: Schematic diagram of the printed solid-state electrolyte; a-c) lines, grids, columns printed designs with d-f) conformal ink, and g-i) self-supporting ink. Retrieved from [14].

The applications of DIW on printing battery components in solid-state, composite, or traditional Li-ion batteries is vast. There are numerous studies published outlining success in 3D printing various architectures to improve battery performance. However, more research and analysis is required to commercialize such technique and understand how to optimize and improve the ink synthesis and printing process.

2.2.2.2 Fused Filament Fabrication

Fused Filament Fabrication (FFF) is a filament-based extrusion technology that is widely employed in AM due to its ease of use and ability to print things of varying sizes. DIW provides better resolutions than FFF, although as previously stated ink preparation and handling might be challenging. FFF, on the other hand, employs solid thermoplastic-based filament that is heated to a semi-molten condition at the fine nozzle tip prior to extrusion, resulting in a comparatively straightforward 3D printing method. Despite the benefits of FFF, the available filaments for battery applications are limited to polymer-based composites and electrode filaments [75,85]. Despite these obstacles, entire ceramic electrodes for Li-ion batteries were created using a standard desktop FFF 3D printer, the i3 Hephestos (Figure 15). The anode and cathode of choice were lithium titanium oxide (LTO) and lithium cobalt oxide (LCO) printed with different architecture designs into 10 mm diameter by 1.5 mm height and 6 mm diameter by 7 mm height, respectively. Table 4 details the printing parameters. Following the successful prints, de-binding was performed at 550°C and sintering at 900°C x 6h in a N_2 and 5% H_2/Ar atmosphere [85].

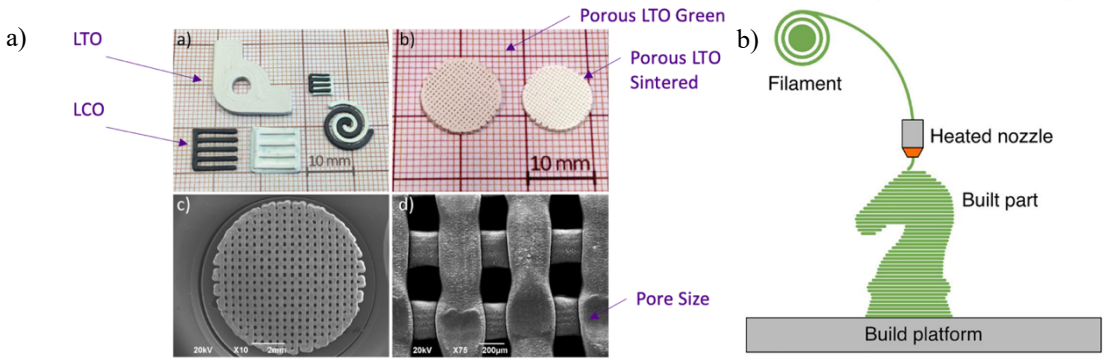

Figure 15: a) Full ceramic LTO (white) and LCO (black) electrodes printed and sintered, b) LTO porous electrodes in green and sintered states; SEM image of c) LTO electrode, d) pore size of grid-shaped electrodes; Retrieved from [85]. e) Schematic diagram of FFF; Retrieved from [17].

This study reported the first-ever success in creating ceramic electrodes for Li-ion batteries using FFF 3D printing. This approach may create a wide range of designs, from macroscale to microscale. More research and filament development are required to ensure the successful production of solid-state Li-ion batteries using FFF 3D printing.

Table 4: FFF printing parameters for LTO and LCO ceramic electrodes [85].

Process Parameter	**Value**
Nozzle Temperature	210°C
Nozzle Diameter	0.2 mm
Line Speed	5-40 mm/s
Flow Rate	0.1 and 0.4 mm^3/s
Layer height	0.1 mm

2.2.2.3 Ink Jet Printing

Ink jet printing (IJP) is a printing process that allows for the deposition of functional inks by continuous drop-on-demand (DOD) printing. A constant stream of droplets produced by a pressure pump and piezoelectric crystals or plates is used to extrude the ink [73,86]. It is worth noting that there are many versions of IJP based on the manufacturer, which defines the printing capability. As the particle size may be controlled, the DOD printing method is the principal approach used [87]. DOD printers can be further divided into thermal, piezoelectric, acoustic, and electrostatic systems; however, the piezoelectric DOD

system will be the subject of this report. When a pressure pulse is produced, the piezo-crystal plates contract and compress, producing droplets that range from 1 to 1000 pL. A high resolution of printed patterns is possible with DOD printers with a fast speed of 500 mm/s with resolution of 5 µm x 5 µm [86]. The process parameters of IJP include nozzle diameter, ink concentration, substrate temperature, layer thickness, droplet spacing, printing repetition, and pressure.

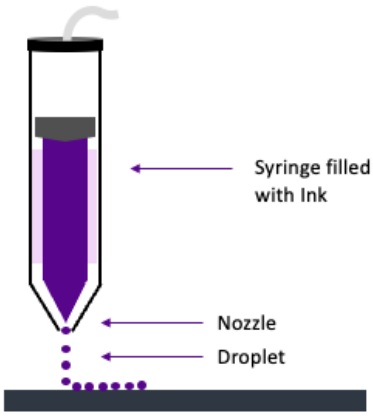

Figure 16: Schematic diagram of IJP.

Similar to DIW, rheology of ink is a critical aspect to determining drop ejection behaviour during IJP. Wolfgang von Ohnesorge demonstrated how viscosity, surface tension and fluid inertia affect the flow behaviour. The Reynolds (R_e) and Weber (W_e) number can be correlated using the Ohnesorge number to print the printability of ink (Z) as shown in equations below [86].

$$\text{Reynolds Number; } R_e = \frac{v\rho a}{\eta} \tag{3}$$

$$\text{Weber Number; } W_e = \frac{v^2\rho a}{\gamma} \tag{4}$$

$$\text{Ohnesorge Number; } O_h = \frac{\sqrt{W_e}}{R_e} \tag{5}$$

$$\text{Printability of Ink; } Z = \frac{1}{O_h} \tag{6}$$

These equations establish a straightforward approach for determining the printability of the ink by taking into consideration the velocity, density, characteristic length, dynamic viscosity, and surface tension. Although $Z > 2$ produces a stable drop, the printability region for DOD printing is more often referred to as the Z range from 1 to 10 (Figure 17a) [16,73,86].

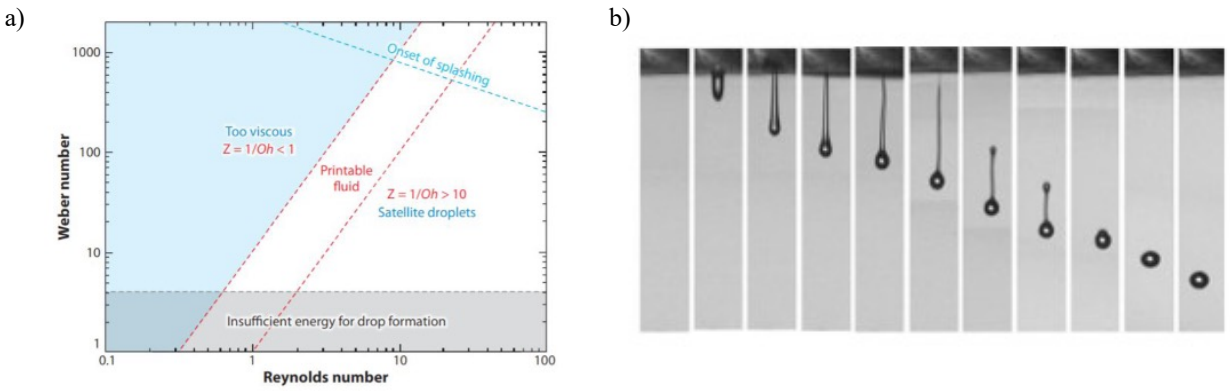

Figure 17: a) Parameter space for drop on demand printing by correlating Reynold's and Weber number; b) Ideal droplet ejection process for IJP. Retrieved from [86].

When Z is too high, satellite droplets form, whereas when Z is too low, viscous forces prohibit drop formation. It should be noted that a few research support slightly varying printability ranges. For instance, according to Jun et al., the printability region for DOD is 1 to 14. [87]. The Ohnesorge number has provided a way of prediction for high-quality printing in straightforward Newtonian fluids, regardless of the range utilized. A drop's ability to break free of a liquid's surface tension and form at the slowest feasible speed suggests that printing is conceivable when the Weber number is larger than 4. Complex inks with the proper range of surface tension, viscosity, and stability may not eject the desired drop. Therefore, to predict printing behaviour, each formulation still needs its unique analysis [86].

Sztymela et al. have studied the fabrication process of electrode inks in order to further analyze the viability of IJP. Particle size, viscoelasticity, rheological properties, and dispersion state are the primary issues with IJP that need to be explored. The nozzle diameter sets a restriction on the particle size. To enable these smaller particle sizes needed for smaller nozzle diameters in IJP, nanoparticles are frequently used. Since insufficient physical contact between the particles might reduce electrochemical performance and electrical conductivity, a binder is frequently added to the ink to connect active materials with conductive agents and ensure adhesion to current collectors. To enhance drop formation, ink surface tension and viscosity (rheological properties of inks) should also be modified [86]. For printability, a viscosity range of 3 to 20 cP and a surface tension range of 25 to 34 mN/m are preferred [88]. The choice of solvents, binders, and other additives can affect these properties. Finally, the printing process may be hindered by bigger agglomerates that form due to the dispersion state. Functional inks must be sufficiently well dispersed and stable to overcome these obstacles [86]. The ideal droplet ejection process is shown in Figure 17b.

The advantages of high accuracy thin-film electrodes coupled with higher electrochemical performance make IJP applications in the field of Li-ion batteries beneficial. It can be difficult to formulate ink to create

ideal droplets without drag or satellite droplets formation. Additionally, rheological characteristics of ink created to print thin-film electrodes must be discussed in new research publications in relation to printability.

In 2020, Denis S. et al. have successfully printed a Li-rich cathode for thin-film micro-batteries. IJP's high resolution, adaptability, and cost-effective benefits were the driving forces behind this decision to employ it as a printing technique. In contrast to other deposition processes, the jetted drop can provide precision material deposition with a diameter of 20 µm and a structure height of 100 nm. The ink was synthesized using $Li_{1.15}K_{0.05}Mn_{0.54}Ni_{0.13}Co_{0.13}O_2$ (LMR-K) cathode material with polyvinylidene fluoride (PVDF) binder and carbon black as the additive using an 8:1:1 ratio ensuring homogenous distribution in the ink. The viscosity and surface tension of the inks were measured to determine the printability of the ink, as shown in Figure 18a [88].

a)

Active component concentration [wt.%]	PVDF	η, cPs[a)]	γ [mN m^{-1}][a)]	Re[b)]	We[b)]	Oh[b)]	Z[b)]
0.01	Solef 5130	3.2	27	50.9	49.8	0.14	7.2
	HSV 900	3.1	27	54.2	49.8	0.13	7.7
0.02	Solef 5130	3.8	28	44.2	48	0.16	6.4
	HSV 900	3.3	27	50.9	48	0.14	7.3
0.03	Solef 5130	4.2	26	40.1	57.6	0.18	5.6
	HSV 900	3.5	28	48	51.7	0.15	6.7
0.04	Solef 5130	4.9	28	34.3	48	0.2	4.9
	HSV 900	3.7	28	45.4	48	0.15	6.5
0.05	Solef 5130	6.1	28	27.5	48	0.25	3.9
	HSV 900	3.9	27	43.1	49.7	0.16	6.1

[a)]Measured. [b)]Calculated.

b)

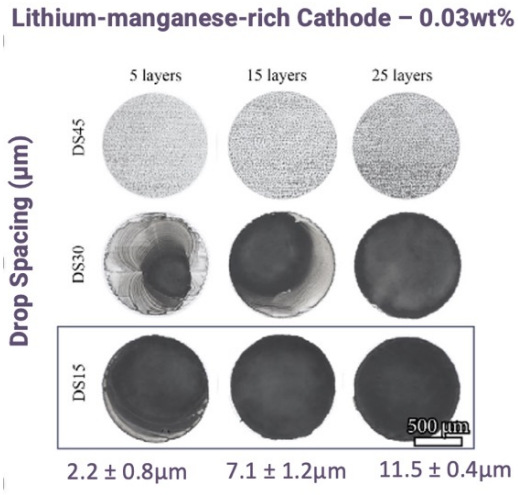

Figure 18: a) Rheological parameters with varying LMR-K active component cathode ink; b) printed cathodes with varying drop spacing and layers. Retrieved from [88].

The ink was processed using the FujiFilm Dimatix Materials Printer DMP-2841 on a heated stage to 45°C with 20 µm aluminum substate (current collector). Figure 18b illustrates the printing process using different drop spacing (15, 30, and 45 µm) and 5, 15, and 25 layers. The optimal drop spacing was 15 µm while increasing layer thickness from five layers to 25 layers increased the printed height from 2.2 ± 0.8 µm to 11.5 ± 0.4 µm. Therefore, the average deposition was 0.46 µm per layer with a jetting velocity of 8 m/s. The ink was filtered through a silicon dioxide membrane to minimize the effects of nozzle clogging, and the shape of the jetted drops was controlled by a voltage impulse. The printed ink cathode was dried in an oven at 200°C to evaporate remaining solvents [88]. This simple process flow in IJP was able to produce

precise thickness cathodes with good electrochemical properties showing potential to fabricate thinner and lightweight batteries in the medicinal, and aerospace applications.

2.2.3 Critical Analysis of AM of Batteries & Summary

New manufacturing processes ought to be investigated to satisfy the requirements as solid-state batteries become more widely used to boost energy density and battery lifetime. In solid-state batteries, ions are transported from the anode to the cathode using a SE rather than a flammable liquid electrolyte. To boost energy density, the SSB combines a solid-state cathode with a Li metal anode. Despite its many difficulties, AM has emerged as a viable alternative to the current coating techniques (tape-casting, doctor-blade) for custom-shaped conventional and solid-state batteries [41,46,89,90].

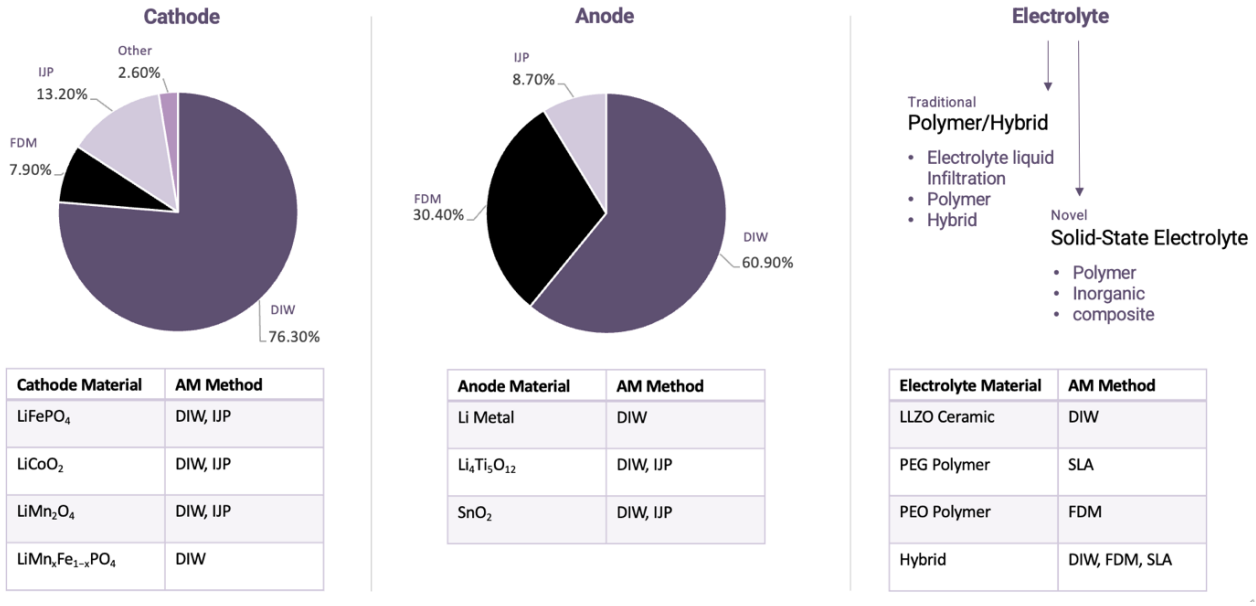

Cathode Material	AM Method
$LiFePO_4$	DIW, IJP
$LiCoO_2$	DIW, IJP
$LiMn_2O_4$	DIW, IJP
$LiMn_xFe_{1-x}PO_4$	DIW

Anode Material	AM Method
Li Metal	DIW
$Li_4Ti_5O_{12}$	DIW, IJP
SnO_2	DIW, IJP

Electrolyte Material	AM Method
LLZO Ceramic	DIW
PEG Polymer	SLA
PEO Polymer	FDM
Hybrid	DIW, FDM, SLA

Figure 19: Summary of cathode, anode, and electrolyte AM fabrication. Data Retrieved from [75].

Figure 19 combines information about AM techniques for anode, cathode, and electrolyte materials from published review paper. The current top-performing printing method for cathode and anode materials is DIW dominating by 76 and 61 percent, respectively. This information applies to all types of batteries rather than just Li-ion batteries. A polymer/hybrid electrolyte is typically printed with DIW, FDM, or SLA for whereas a solid-state ceramic electrolyte was fabricated with DIW [75]. It should be noted that other AM techniques, such as binder jetting and laser-based powder bed fusion of polymers (PBF-LB/P), have also been investigated for printing batteries but are not included in this review. PBF-LB/P is an established technology with a nearly one-step production process that has been commercialized in numerous industrial applications (Figure 20). This method has a high degree of geometric printing freedom and does not require any post-processing processes [90]. Further discussion on these methods is beyond the scope of this report.

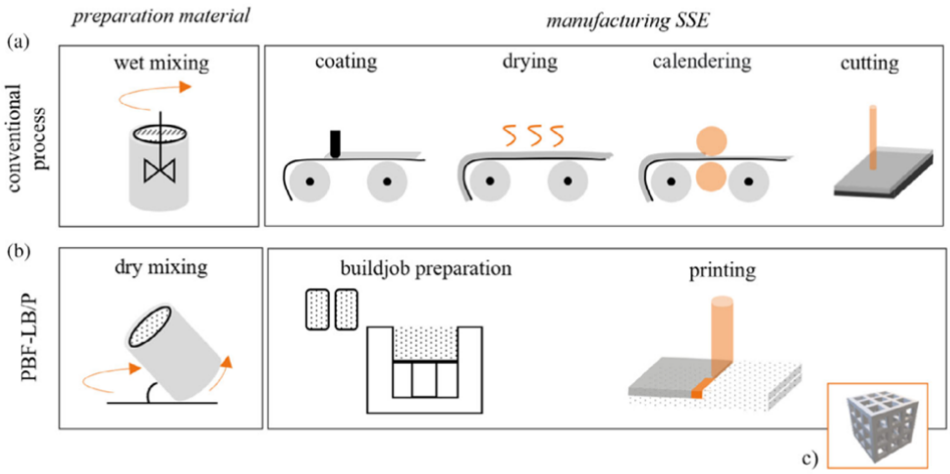

Figure 20: a) Conventional battery fabrication process; b) PBP-LB/P fabrication process; c) SE geometry. Retrieved from [90].

Numerous fabrication methods for AM were covered in this review, including DIW, IJP, and FDM. Due to the wide range of rheological parameters required, DIW was said to be the widely used approach. The advantages of its straightforward operation include quick, high-resolution printing at a low cost. Similarly, IJP can print high-resolution battery components that include active elements already incorporated into the ink. However, synthesizing the ink with the appropriate rheological characteristics for DIW and IJP has proven to be challenging, making commercialization of these approaches complicated. In Figure 21 and Table 5 below, a comprehensive summary of the comparison of different methodologies is presented.

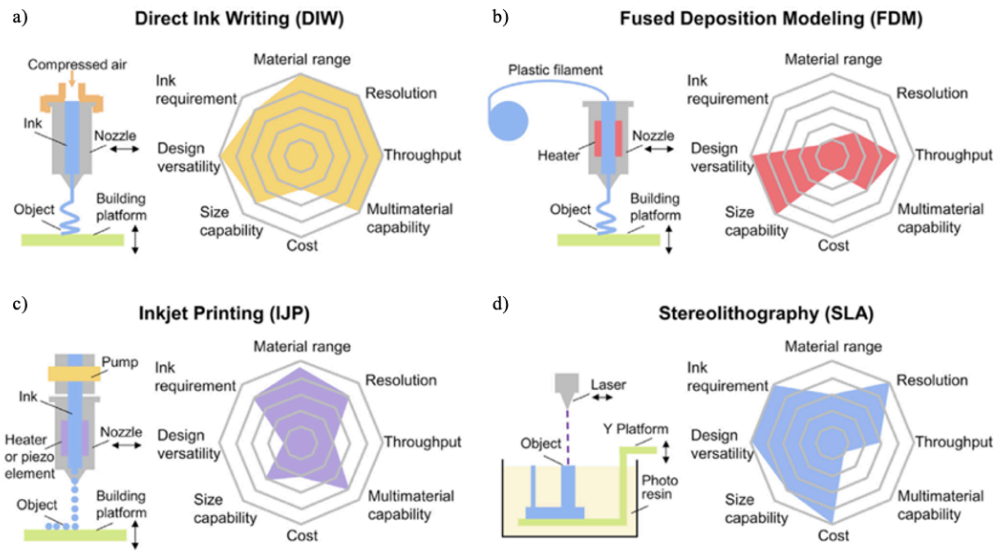

Figure 21: Radar Plots for DIW, IJP, FDM, and SLA fabrication methods. Retrieved from [75].

Table 5: Summary for DIW, IJP, FDM, and SLA fabrication methods. Table recreated from [15].

Method	Available materials	Printing Resolution	Advantages	Disadvantages
DIW	• Plastic • Metal • Ceramic • Food	50 µm	• affordable cost • easy operation • large material diversity	• Weak mechanical properties • High requirement in materials • Shrinkage and warping
IJP	• Metal • Conductive polymers • Carbon-based materials	20 µm	• low cost • multi-material printing capability	• low printing speed • not good for high-volume printing • print head is less durable
FDM	Thermoplastic	50 - 200 µm	• user-friendly • high speed • large size capability	• limited resolution on z-axis • weak mechanical properties • low surface quality
SLA	Photopolymers	0.25 - 10 µm	• high resolution • high surface finish • high efficiency	• strong limitation in multi-material deposition

Further comparison of fabrication techniques can be done with fabrication speed, thickness of produced film, and material wastage. DIW, IJP, FDM and SLA printing techniques all have fast fabrication speed, micron range of film thickness, and less material wastage. Conventional battery fabrication techniques such as casting and coating can have fast fabrication speed, similar film thickness but higher material wastage compared to AM techniques with significantly low design freedom [41,91]. Table 6 below reiterates the benefits of design freedom, areal energy density, power density and volumetric energy density in 3D printed batteries compared to tape casting for conventional batteries. To further highlight critical reporting metrics required for successful battery manufacturing meeting current demands, Narita K. et al. have published a chart with rationale as shown in Table 7 [17].

Table 6: Summary of 3D printing and tape-casting batteries. Table recreated from [75].

Manufacturing Process	Design Freedom	Areal Energy Density	Areal Power Density	Volumetric Energy Density	Manufacturing Cost
3D Printing Batteries	high	high	high	high	moderate
Tape Casting for conventional batteries	low	low	low	low	low
Deposition techniques for 3D micro batteries	moderate	moderate	moderate	low	high

Table 7: Summary of reporting metrics required for future studies of AM of batteries. Table recreated from [17].

Category	Reporting Metric	Rationale
Electrochemical Performance	Gravimetric Capacity (mAh/g)	• Asses electrochemical performance of material • Discharge capacity should be normalized by active material mass
	Areal Capacity	• Useful comparison to conventional batteries • 3D printed batteries can have high areal capacities → reduce need for current collectors • Normalized by battery footprint area
	Rate Capability (%)	• Rate capability at high rates (e.g. 2C) should be reported • 3D printed battery is promising by optimizing ion and electron trajectories • Capability at high rate should be normalized by theoretical capacity
	Capacity retention (%)	• Capacity retention after long cycling should be reported to assess cycle life and degradation • Number of cycles before 80% initial capacity is reached
Constituent materials	Active material fraction. (wt and vol%)	• Delineate between AM approaches which superfluous electrochemically inactive material for printing
	Minimum feature size (μm)	• Assess the potential for reported AM method to reduce ion/electron length
3D structure design	Relative Density (%)	• Practically void space is filled with electrolyte and should be minimized
	Interfacial area ratio (unitless)	• $\frac{A_{interface}}{A_{footprint}}$ • Assess degree to which 3D geometry improves ion transport pathways and quantify benefits of interdigital fully 3D battery structures

In summary, new developments in advanced coating technologies will be required to produce controlled interfaces, microstructures, and form factors as the battery industry continues to expand quickly, notably with the growing usage of solid-state batteries in electric vehicles [46]. The manufacturing of Li-ion batteries has several critical problems that must be resolved to boost production efficiency, decrease cost, and permit innovative designs.

A collaboration between academia and can help bridge the gap in theory and practical innovation [76,92] In the past few years many start-ups have emerged promoting the commercialization of battery manufacturing with AM technologies. With new advances in technology and research in AM methods, applications in battery manufacturing are feasible.

2.3 Ink Synthesis & Challenges

Section 2.3 includes a review of ink components and its synthesis techniques, and DIW printing of ceramics.

2.3.1 Components of a Printable Ink

The ink prepared for DIW printing is critical to obtaining a well-printed sample. The properties of the ink such as viscosity (10^{-1} to 10^{3} Pa s) and homogeneity determine how well the ink can be dispensed uniformly without clogging the nozzle tips. The components of the ink and their respected functions are summarized in Table 8.

Table 8: Components of ceramic ink with its respective function.

Component of Ink	Function
Solid Particles	Determine solid loading of ink
Dispersant	Aid solid particles to disperse evenly in the ink
Solvent(s)	Liquid substance(s) in which other components of ink can dissolve or disperse in
Binder	Enhance the strength of the green body by establishing connections or bridges between particles
Plasticizer	Soften binder to increase the flexibility of green body

Solid Loading

The solid loading of the ink is dependent on the amount of solid particles are dispersed in the ink. A higher solid loading will increase the viscosity of ink and the density of green part [93].

Dispersant

A dispersant, also known as a deflocculant, is a chemical additive designed to facilitate the even dispersion of solid particles within ink, by enhancing the repulsion between these particles. Dispersants also play a crucial role in stabilizing colloidal suspensions. Typically, only a very small concentration of dispersant is required, ranging from 0.5% to 2% by weight [93].

Dispersants can be categorized into three groups based on their chemical structure: simple ions and molecules, short-chain polymers featuring functional head or end groups, and low to medium molecular weight polymers. Simple ions and molecules are effective in aqueous solvents, aiding the dissociation of dissolved inorganic compounds. Surfactants, characterized by short-chain polymers with functional head or end groups, have a brief organic tail (50-100 carbon atoms long) and a functional head group that can be either non-ionic or ionic. Surfactants can reduce the surface tension between phases of substance whereas dispersants prevent large particle agglomerates. Non-ionic surfactants are typically used in organic solvents,

whereas ionic surfactants are more commonly employed in aqueous solvents. The adsorption of these polymers can take place through weaker van der Waals bonding or hydrogen bonding [93].

In SE inks, a few common dispersants include menhaden fish oil [94,95], castor oil phosphate [12,96,97], and ethylene glycol [12], among others.

The viscosity of the ink is influenced by the content of dispersant (Figure 22a). Yu Mingxian et al. demonstrated that the viscosity of alumina ink initially decreased with an increase in dispersant content, and then reached a minimum point. This decrease in viscosity corresponds to the absorption of dispersant on the surface of the ceramic powder. After reaching a point of dispersant saturation, any excess dispersant remaining in the solvent, leads to an increased viscosity [97].

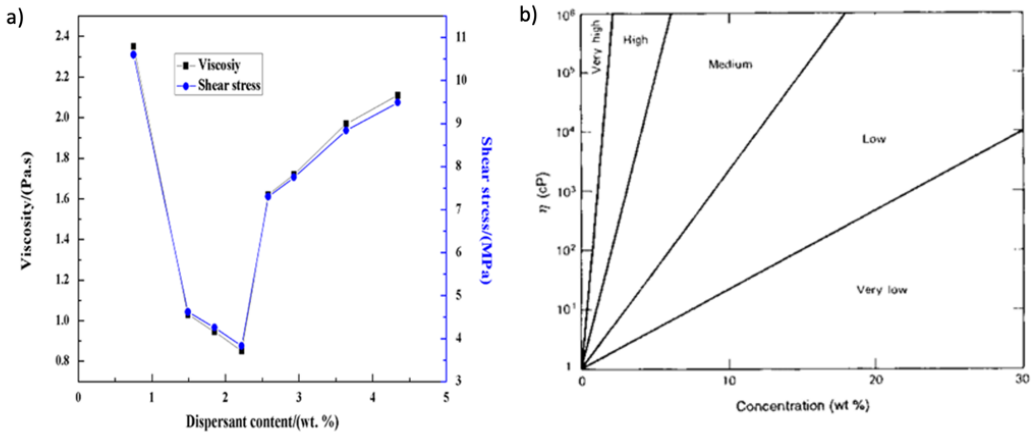

Figure 22: a) Plotted relationship between dispersant content and viscosity. Retrieved from [97]; b) Plotted relationship between binder concentration and viscosity of ink. Retrieved from [93].

Solvents

Solvents are liquid substances in which the other ink components can either dissolve or disperse, facilitating solution-based processing [9,12,93,98]. The choice of solvent(s) has a direct impact on the drying process of the printed or tape-casted ceramic. It is crucial to consider the physical characteristics of the solvents, including viscosity and vapor pressure, when selecting the most appropriate solvents. Neglecting to consider these properties can result in premature cracking during the drying process.

Binder

A binder serves as an additive that imparts strength to the green body by forming connections or bridges between particles and facilitating effective dispersion [93,98]. Typically, binders are long-chain polymers composed of ring-type monomers. A wide array of organic substances can be used as binders, and they may be soluble in either water or organic solvents. It is crucial to conduct a thorough analysis of how binders

influence the rheology of a solvent. The addition of an organic binder can elevate the viscosity of the ink. Binder concentrations can be categorized into low, medium, and high viscosity grades as outlined in Figure 22b. However, it is important that the binder does not cause a rapid increase in solvent viscosity as its concentration rises. This can restrict the amount of powder that can be incorporated into the ink [93].

The binder plays a pivotal role in governing the interactions between solid particles and aids in achieving the desired shape, density, and strength prior to its removal through burning [99]. In ceramics, an effective binder should possess a slow burn rate to maintain structural integrity during pyrolysis or binder elimination. Inadequate organic burnout can lead to issues such as reduced density, diminished mechanical strength, and compromised electrical properties [98]. In the case of SE inks, a commonly used binder is polyvinyl butyral (PVB) which has a boiling point of 660°C [14,93–96,98,99].

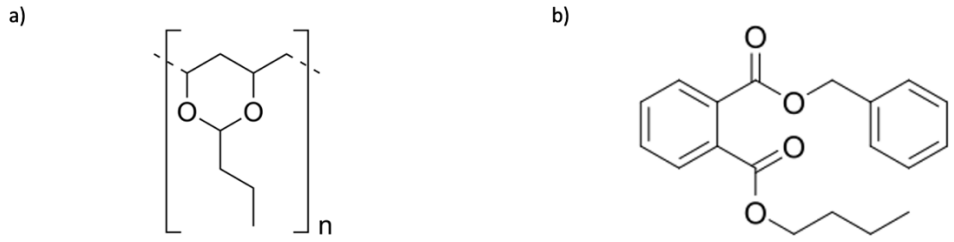

Figure 23: a) Chemical structure of PVB and b) BBP.

Plasticizer

A plasticizer is an additive that increases the flexibility of the green body by softening the binder. Generally, plasticizers are organic compounds with a lower molecular weight than the binder. These plasticizer molecules position themselves between the polymer chains, reducing the van der Waals bonding of the binders and disrupting their alignment [93]. In the case of SE inks, one commonly used plasticizer is butyl benzyl phthalate (BBP), which has a boiling point of 370°C [14,94–96].

Analyzing the ratio of binder to plasticizer in an ink can provide valuable insights into the impact on the density and strength of green tapes, while keeping the binder content and solid loading constant. For instance, in a study by Yu Mingxian et al., it was observed that the density and strength of green tapes gradually increased up to a 1:1 ratio of binder to plasticizer (using PVB as the binder and BBP as the plasticizer). However, beyond this 1:1 ratio, both the density and strength of the green tapes decreased (Figure 24). The incorporation of BBP plasticizer into the slurry was determined to be successful in reducing the glass transition temperature of PVB. This proved advantageous in reorganizing particles to attain microstructure homogeneity in the green tapes, ultimately leading to higher density and strength.

However, excessive plasticizer content had the opposite effect, leading to a decrease in the strength and density of the green components [97].

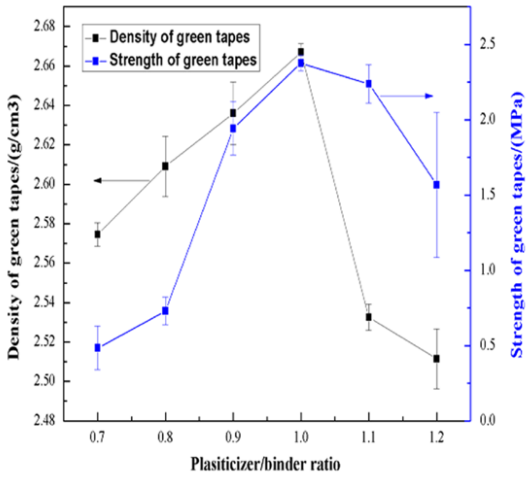

Figure 24: Plotted plasticizer/binder ratio relationship with density and strength of green tapes. Retrieved from [97].

2.3.2 Mixing of Ink Components

The preparation of inks hinges on the interactions between solids and liquids and can be categorized into several distinct stages: (1) mixing of solids, (2) mixture wetting, and (3) stable suspension formation. It's essential to differentiate between wetting and dispersing, a concept referred to as mixture wetting (Figure 25). When a solvent is introduced to solids, this process is termed wetting. Conversely, when solids are added to a solvent, it is referred to as dispersing. Saturation of the components can lead to adhesion stress, resulting in the formation of agglomerates. Various mixing techniques can be employed to break down these agglomerates, ultimately achieving a stable and uniform mixture [72,100].

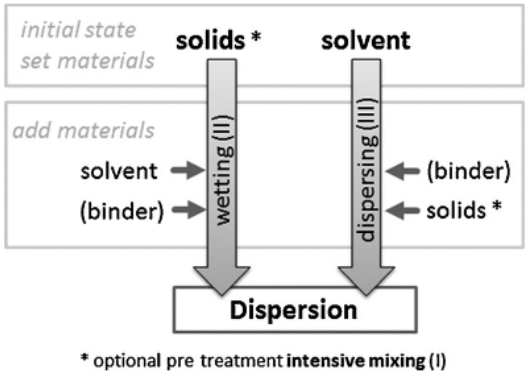

Figure 25: Depiction of dispersion of solids and solvents. Retrieved from [72].

The dispersion of solid particles within liquid mediums can take various forms, each contingent upon the energy requirements involved. These forms are typically categorized as follows: impeller mills, ball mills, stirred media mills, vibratory mills, and ultrasonic dispersers, ordered by increasing breakage energy for particle dispersion. The choice of mixing equipment required for dispersion is determined by factors such as ink viscosity, particle size, and the strength of agglomerates [94,101].

In the preparation of ceramic ink, it is a common practice to employ ball mills to disperse solid particles and binders within a solvent mixture. The effectiveness of dispersion can be adjusted by varying factors such as the rotational speed, ball size, ball type, and ball density. This allows for the dispersion of inks with low to medium viscosity [101].

To ensure sufficient shear stress for dispersion, typically, milling media fills approximately 40-60% of the mill volume. However, it is important to note that as the liquid volume within the mill increases, the efficiency of dispersion decreases slightly. This decrease in efficiency occurs because the mixing balls need to emerge from the liquid phase during the duration of the process to achieve good dispersion [101].

2.3.3 Preparation of Ceramic Inks for DIW

There are three primary ink types used in DIW: colloidal, hydrogel, and organogel suspensions. Colloidal suspensions are comprised of densely concentrated inks that contain ceramic particles suspended in a low-viscosity liquid, along with a small quantity of organic additives. In this composition, electrostatic, steric, or electrosteric interaction forces can occur among the particles. Introducing dispersants and plasticizing agents into the ink improves extrudability. In contrast, gel-embedded inks like hydrogels and organogels demonstrate unique rheological properties primarily determined by the characteristics of the gel phase rather than interactions among particle [5,9]. It is important to note that this thesis focuses on the synthesis and printing of colloidal inks.

Ceramic materials, including zirconia, alumina, and carbides, exhibit favorable physical and mechanical properties such as electrical conductivities, hardness, strength, and wear resistance across different temperatures. These characteristics make ceramics suitable for diverse applications in the biomedical, aerospace, automotive, and energy sectors. The typical production methods for ceramics involve die pressing and tape casting, employing additives and binders. However, AM presents an innovative approach for creating intricate and precise three-dimensional structures. [5]. A brief comparison of ceramic materials printed with DIW is presented in Table 9.

Table 9: Summary of common ceramic particles printed with DIW.

Ceramic Material	Additives	DIW Printing Parameters	Sintering method	Ref
$Li_{6.4}La_3Zr_{1.4}Ta_{0.6}O_{12}$	PDMS, Ethylene glycol, wax Paraffin oil, DMF, wax Castor oil, Span80, wax	Nozzle size: 150 - 400 µm Size: 5.7 × 5.7 × 3 mm	1050°C x 2h + 1260°C x 12h	[12]
8Y-ZrO_2	Pluronic® F-127 + distilled water	Nozzle size: 580 µm Size: 10 mm diameter, 10.44 mm height	700°C x 1h + 1450°C x 2h	[102]
rutile titania powder	deionized water, sodium hexametaphosphate and sodium alginate	Nozzle size: 1- 2 mm Size: 20 mm diameter, 40 mm height	1300°C x 3h	[103]
ZrO_2	ammonium citrate, polyvinyl alcohol (PVA), deionized water	-	1250°C x 4h	[104]
$Y_{2.97}Nd_{0.03}Al_{5.00}O_{12.00}$ (Nd:YAG)	poly(ethylene glycol), ether-based solvent, ether-derivatized carboxylic acid	Nozzle size: 610 µm Size: 4 mm, x 20 mm Line speed: 5 mm/s	1750°C x 4h; Hot isostatically press	[105]
α-SiC powders	PEG, TMAH, guar gum, short carbon fibres	Nozzle size: 500 µm Size: 4.5 × 4.5 × 52 mm Line speed: 12.5 mm/s	1600°C x 2h under vacuum	[106]
alumina-zirconia-silica	sodium hydroxide, sodium silicate and distilled water	Nozzle diameter: 840 µm Size: 50 × 5.88 × 5.04 mm^3	1200°C - 1400°C	[107]
SiO_2–Al_2O_3	silica fume, water	Nozzle diameter: 2 mm Layer height: 0.8 - 1.8 mm Line speed: 35 mm/s	1600 °C x 3h	[108]

In summary, the biggest processing challenge of the ink synthesis and printing process is associated with the ink synthesis and composition. The ink synthesis route is designed to yield a homogenous ink with minimal agglomerates. The mixing method of choice influences the ability to break down large agglomerates during the synthesis process due the breakage energy. Failure to relieve large agglomerates can cause the printing nozzle tips to clog impeding the flow. The composition of the ink including solid loading, solvent, ratios, and binder-plasticizer ratios can impact the drying of the printed ceramic part. Therefore, another challenge identified with the ceramic ink composition is the cracking associated with shrinking, and the adhesion to the printing substrate. These challenges must be resolved by optimizing the ink synthesis, composition, and processing procedure.

After ceramic fabrication, the green bodies must undergo post-processing treatments such as thermal de-binding and sintering to achieve hardening and consolidation [5].

2.4 Sintering of LLZO & Challenges

There are multiple methods available for achieving dense sintered LLZO ceramics, encompassing various preparation, processing, and sintering techniques such as hot pressing, field-assisted sintering, and spark plasma sintering [19]. Nevertheless, these approaches come with considerations regarding equipment expenses, reproducibility, and intricate processes.

The processing of LLZO ceramics presents notable complexities. While most literature reviews delve into topics like crystal chemistry, doping, electrochemical attributes, and interface manipulation, the discourse on LLZO processing remains scarce [19].

Some common challenges are:

- inadequate sintering capabilities due to Li loss experienced at temperatures exceeding 1000℃.
- intricacies surrounding sintering conditions and set-ups.
- susceptibilities to H_2O/CO_2 reactivity.
- a limited grasp of the relationship between composition and microstructure.

2.4.1 Poor Sinterability of LLZO

Traditionally, the successful sintering of LLZO ceramics has demanded elevated temperatures ranging from 1100°C to 1300°C for extended periods [19,21,109]. Despite the straightforward and scalable nature of ceramic processing, a substantial challenge encountered in LLZO ceramics processing is the pronounced Li loss at these higher temperatures. This predicament is primarily due to the sublimation of Li_2O, which occurs at temperatures exceeding 1000°C during prolonged sintering, resulting in the loss of Li. This phenomenon introduces phase impurities and deviations in composition, consequently impacting the efficacy of the LLZO SE. The structural integrity of LLZO is compromised, often leading to the coexistence of the pyrochlore $La_2Zr_2O_7$ phase, which in turn diminishes the material's ionic conductivity [19,21,109].

To address this challenge, various techniques are explored, including enclosing pellets with additional LLZO mother powder, or introducing excess Li within the initial green part. However, considering the presence of costly rare earth metals like La and other dopants in doped LLZO, the use of LLZO mother powder material as an excess Li source can lead to cost escalation [21]. Hence, a more cost-effective approach is to investigate alternate Li sources or to explore rapid sintering methodologies. Numerous articles propose incorporating extra Li during the calcination of the powder to facilitate subsequent sintering [30,59,110–116], or the direct introduction of excess Li within the initial composition of bulk pellets or thinner pellets/films [20,59,96,115,117–120].

Calcination

Comprehending the sintering characteristics of LLZO hinges upon a comprehensive grasp of the precursor calcination stage, which predominantly involves metal oxides, hydroxides, or carbonates of Li, La, and Zr, alongside dopants like Li_2CO_3, La_2O_3, ZrO_2, and Ta_2O_3. While a straightforward reaction equation may be developed, the complexities of these reactions are clearly evident from in situ observations.

$$3La_2O_3 + 4ZrO_2 + 7Li_2CO_3 \rightarrow 2Li_7La_3Zr_2O_{12} + 7CO_2 \quad (7)$$

During the decomposition of Li salts in the precursor materials, gaseous species such as CO_2, H_2O, and Li_2O are generated. The rate of decomposition of lithium carbonate plays a pivotal role in managing Li loss, making Li more accessible within the environment. This accessibility contributes to the formation of the cubic LLZO phase.

To counterbalance the Li loss inherent to the calcination process, an excess of 5-15 wt% of Li salt is incorporated into the precursor materials. Notably, the decomposition of lithium carbonate initiates at approximately 740°C, leading to the amorphous state and, culminating the $La_2Zr_2O_7$ intermediate phase at 750°C [30,121,122].

$$Li_2CO_3 + ZrO_2 \rightarrow Li_2ZrO_3 + CO_2 \quad (8)$$

$$La_2O_3 + 2ZrO_2 \rightarrow La_2Zr_2O_7 \quad (9)$$

The initiation of LLZO phase formation commences at approximately 800°C, which subsequently progresses into layer-to-layer diffusion at 900°C (Figure 26). The duration of the calcination phase spans from 10 to 15 hours within the temperature spectrum of 900°C to 1000°C. As the material cools, the cubic phase can transition into the tetragonal phase at 650°C. Nevertheless, the incorporation of dopants such as Ta serves to inhibit this phase transition, thereby ensuring the stable cubic structure [109,121].

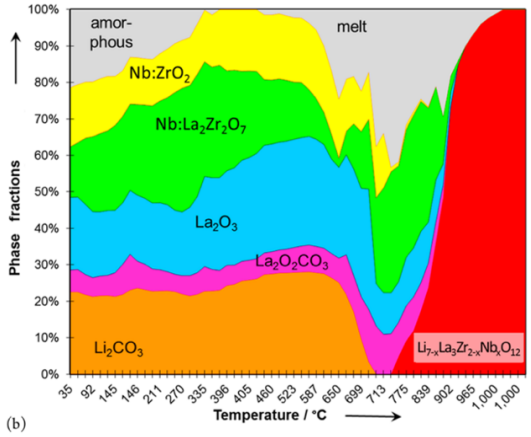

Figure 26: Weight fractions of phases during LLZO formation from 35°C to 1000°C. Retrieved from [123].

Sintering

The synthesized LLZO powder can undergo subsequent processing to create either bulk pellets or thin films based on the intended application, followed by a sintering stage to yield a compact ceramic structure. This phase is arguably the cornerstone of LLZO ceramic preparation, marked by the influence of numerous factors. The properties of the calcined powder parameters such as particle size, distribution, shape, and composition, have a significant impact over the ceramics' sintering capability. For optimal efficiency in the sintering process, fine particle sizes within the range of 500 nm to 1 μm are typically favoured as they facilitate more effective surface diffusion. Several studies have also demonstrated the impact of dopants on sintering [19,67,116,122,124–127]. In comparison to Ta and Nb dopants, Ga-dopants tend to necessitate lower sintering temperatures and shorter durations [66].

Numerous sintering parameters influence the sintering behaviour of LLZO, including heating profiles, crucible powder covering, ambient conditions, and sintering additives. These factors are elaborated upon in the subsequent section. Conventionally, sintering within the temperature range of 900°C to 1300°C with heating rates ranging between 3 to 10°C per minute. Investigating multi-step sintering processes at 900°C, 1100°C, and 1200°C has been explored with the intent of mitigating impurity phases. Figure 27 demonstrates the heating profile for ultra-fast, multi-step and isothermal sintering. Facilitating the transition from tetragonal garnet to cubic garnet requires suitable time and temperatures, and employing a multi-step strategy to sinter Al-LLZO pellets has demonstrated notable improvements to reduce impurity. In the conventional approach of single-step sintering, grain sizes become larger as pores reduce, leading to an increase in density upon higher-temperature sintering. Nonetheless, with a multi-step sintering technique, grains continue to grow during each phase, thus decreasing pores further and boosting the relative density to over 90% [128].

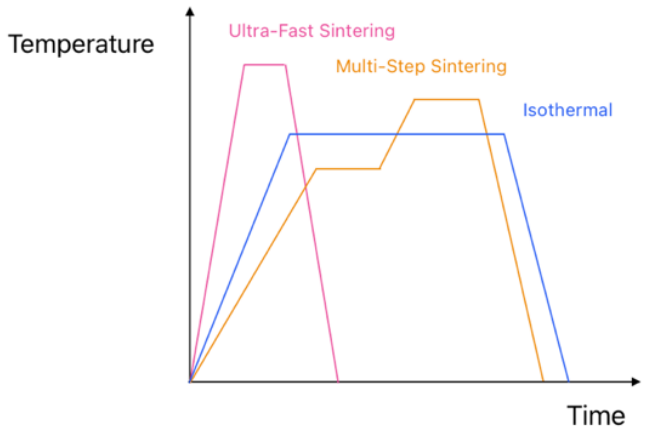

Figure 27: Temperature-time plots of ultra-fast, multi-step, and isothermal sintering.

2.4.2 Sintering Environment and Set-up

The sintering process is significantly affected by the surrounding environment [19]. Several sintering factors must be considered, including the sintering environment (ambient air versus inert gas), the type of crucible used, the use of sintering additives, the chosen sintering temperature, the duration of the sintering process, and how excess Li is incorporated (within the green body versus external powder).

Sintering Environment

LLZO ceramic bulk electrolytes are often sintered in the presence of ambient air flow. Nonetheless, various research developments have revealed the use of flowing inert gas to preserve the cubic crystal phase during sintering. The gas flow has a major effect on the sintering process. For example, Paolella et al. found that decreasing the gas flow can help limit the rate of Li loss, which is assisted by lithium carbonate decomposition [121]. This intervention allows Li_2CO_3 to remain in a molten state for a relatively extended duration, effectively decelerating the decomposition rate. This strategic method promotes interactions between Li_2CO_3 and intermediate $La_2Zr_2O_7$ phases, inducing the formation of LLZO under a Li-rich environment [121]. While this study asserts the successful synthesis of cubic LLZO, gas flow environments remain common within the literature. They ensure gas exchange, thus enabling additional reactions that influence the final stoichiometry.

X-ray photoemission spectroscopy depth profiling can reveal the development of Li_2CO_3 layers, approximately 5-10 nm thick on the LLZO particles. The potential routes for these processes are illustrated in Figure 28. Several reaction mechanisms concerning the carbonation of LLZO are proposed in an effort to comprehend this phenomenon [129].

$$Li_{6.5}La_3Zr_{1.5}Ta_{0.5}O_{12} + xH_2O_{(g)} \rightarrow Li_{6.5-x}H_xLa_3Zr_{1.5}O_{12} + xLiOH_{(s)} \quad (10)$$

$$2Li_{6.5}La_3Zr_{1.5}Ta_{0.5}O_{12} + xH_2O_{(g)} + xCO_{2(g)} \rightarrow Li_{6.5-x}H_xLa_3Zr_{1.5}O_{12} + xLiCO_{3\,(g)} \quad (11)$$

$$LiOH_{(s)} + \frac{1}{2}CO_{2(g)} \rightarrow \frac{1}{2}Li_2CO_{3(s)} + H_2O \quad (12)$$

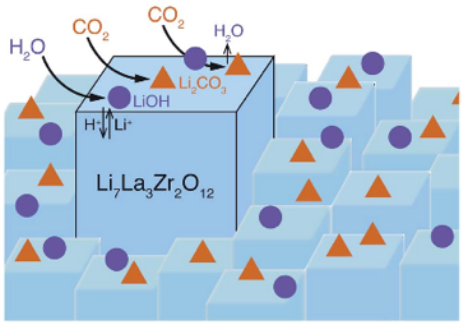

Figure 28: Reaction pathways for LLZO particle contamination when exposed to H_2O and CO_2. Retrieved from [129].

The intricate surface reactions of LLZO upon exposure to ambient air involving H_2O and CO_2 give rise to processing and storage complications for LLZO. The presence of a Li_2CO_3 layer has been demonstrated to have adverse effects on performance [19,129]. Hence, conducting sintering in inert atmospheres like argon, where the concentration of CO_2 is lower, allows to minimize the Li_2CO_3 phase on the surface, preventing a decrease in efficiency [110,129].

Crucible Type

Frequently employed crucible materials for the processes of calcination and sintering are alumina, magnesium oxide, zirconium oxide, or platinum. Earlier investigations into LLZO revealed that during sintering, aluminum ions (Al^{3+}) diffuse from alumina crucibles, leading to doping within the LLZO sample. This phenomenon can expedite the sintering process and promote the stabilization of the cubic phase, resulting in larger grain sizes and heightened conductivity [19,109,130]. However, this diffusion can become uncontrolled, potentially inducing the formation of secondary phases at grain boundaries (such as $LiAlO_2$ or $LaAlO_3$), consequently leading to reduced conductivity. Moreover, the interaction between Al^{3+} and Li_2O can generate challenges in terms of reproducibility. The reaction between Li_2O and Al_2O_3 gives rise to a eutectic liquid, thereby accelerating the sintering of LLZO [130]. Hence, crucibles made of MgO and Pt are favoured as they avoid aluminum contamination, providing better control over phase compositions [19].

$$(2x-3)Li_2O\ (g) + Al_2O_3(s) \rightarrow 2Li_{2x-3}AlO_x \quad (13)$$

Sintering Additives

Sintering additives are recognized for their ability to decrease sintering temperatures while concurrently enhancing the densification process. These additives possess the ability to modify the chemistry of grain boundaries, thereby contributing to improved mechanical strength and stability at the Li interfaces. In the context of LLZO sintering, a variety of additive categories are employed: those containing Li, those free of Li, and soft additives [19].

Additives containing Li compounds exhibit a notably low melting point, prompting the emergence of a liquid and ionically conductive phase at grain boundaries. Noteworthy example is tri-lithium tri-borate (Li_3BO_3), which have a low melting point of approximately 700°C [20,114,131,132]. Another prominent Li-containing additive is lithium oxide. Invariably, the presence of a glass-like phase forms at grain boundaries due to Li_2O association with liquid-phase sintering behavior. This formation leads to a reduction in porosity and a corresponding elevation in density, with values increasing from 91.5% to 97.3% [133]. The concentration of Li_2O has an impact on the optimal sintering temperature, while simultaneously augmenting density, as demonstrated in Table 10 [133]. In this work, the Li-containing additive is used.

Table 10: Influence of Li_2O concentration on optimal temperatures, relative density, total conductivity, activation energy, and electronic conductivity of ceramic electrolytes. Retrieved from [133].

x (wt.%)[a]	Optimal sintering T (°C)	Maximum density (%)[b]	σ_{total} (S cm^{-1})[c]	E_a (eV)[d]	σ_e (S cm^{-1})[e]
0	1230	91.5	2.2×10^{-4}	0.41	3.9×10^{-7}
2	1200	92.3	3.3×10^{-4}	0.38	4.0×10^{-7}
4	1200	95.4	4.4×10^{-4}	0.33	4.3×10^{-7}
6	1170	97.2	6.4×10^{-4}	0.30	5.3×10^{-7}
8	1170	97.3	2.7×10^{-4}	0.39	5.7×10^{-7}

[a] x: concentration of the Li_2O additive.
[b] Maximum relative density after optimization of sintering temperature.
[c] σ_{total}: total conductivity.
[d] E_a: activation energy.
[e] σ_e: electronic conductivity.

Another approach documented involves the use of dual additives, Li_3BO_3 and Al_2O_3, to facilitate sintering at a significantly reduced temperature of 790°C. This innovative process culminated in a final relative density of 90%, coupled with an impressive ionic conductivity value of 0.36 mS/cm [134].

The second category of additives comprises Li-free counterparts such as Al_2O_3, MgO[57], B_2O_3 [135], BN [136], CuO [137], and $La_2Zr_2O_7$ [138]. The inclusion of these additives proves advantageous in fostering LLZO densification, while simultaneously enhancing various other properties such as chemical attributes, mechanical strength, and stability at the Li interfaces.

Lastly, the third class encompasses soft additives, which establish a composite with LLZO through low-temperature treatments. These additives frequently manifest as Li-ion conductors [19].

Sintering Temperature & Duration

Typically, the sintering of LLZO involves an isothermal heating process, where the desired temperature is maintained for a specific duration. Earlier investigations commonly employed high temperatures exceeding 1200°C for extended periods, usually surpassing 20 hours, as effective sintering conditions [19]. Doped LLZO variants, such as those with Al, Ga, Ta, Sr, and Fe, are recognized for their ability to accelerate the sintering process. The sintering duration has shown variation in recent research, spanning from 0.5 hours to 24 hours [20–22,25,27–31,56,57,61,62,128,139]. Alternatively, rapid high-temperature sintering with elevated heating rates at temperatures above 1300°C has the potential to induce rapid densification in LLZO [19,21]. In 2019, Yang Li et al. introduced an innovative approach involving rapid sintering. This method entails sintering LLZO ceramic electrolytes at 1360°C for 10 minutes, a method aimed to mitigate Li loss and curb abnormal grain growth. Remarkably, these pellets achieved both high conductivity (8.5×10^{-4} S/cm at 25°C) and a relative density (97%) without the requiring excess Li from mother powder [21].

Evidently, properties of ceramic bulk pellets and thin films differ in thickness, processing methods and applicability as shown in Table 11. Therefore, it can be inferred the sintering properties also differ to favour the application. Thin film LLZO ceramic electrolytes have a larger surface area to volume ratio leading to more Li loss. To mitigate this, the temperature and duration can be adjusted to achieve a high-density cubic phase ceramic. Comprehensive literature review of LLZO pellets and thin-film sintering is presented in Table 12 and Table 13.

Table 11: Comparison between LLZO pellets vs thin-film properties. Table recreated table from [19].

	Ceramic Bulk (Pellets)	**Thin-Film**
Properties	• Conductivity: 10^{-4}-10^{-3} S/cm • Thickness: mm-µm	• Conductivity: 10^{-8}-10^{-4} S/cm • Thickness: < µm
Processing method	• Powder pressing • Conventional sintering • Advanced sintering	• Physical vapour deposition • Chemical vapour deposition • Sputter, aerosol deposition • 3D printing
Battery applicability	• Researched process • Sintering difficulty • Poor interfacial contact	• Processing difficulty • Good interfacial contact • Low battery capacity

Table 12: Literature comparisons of sintering conditions of LLZO solid electrolyte pellets.

Composition	Additives/ Excess Li	Sintering Conditions	Atmosphere	Crucible Type	Phase	Relative Density (%)	Total Conductivity ($x10^{-4}$ S/cm)	Ref
$Li_{6.4}La_3Zr_{1.4}Ta_{0.6}O_{12}$	-	1250°C x 40 min	Ambient Air	Alumina	cubic	79	5.22	[109]
$Li_{6.25}Al_{0.25}La_3Zr_2O_{12}$	1wt% BN	1100°C x 12h	Ambient Air	Alumina	cubic	83.8	6.21	[136]
$Li_{6.5}La_3Zr_{1.5}Ta_{0.5}O_{12}$	Mother Powder	1200°C x 12h	Ambient Air	MgO	cubic	86.7	1.18	[21]
$Li_{6.5}La_3Zr_{1.5}Ta_{0.5}O_{12}$	Mother Powder	1320°C x 0.5h	Ambient Air	MgO	cubic	87.1	2.2	[21]
$Li_{6.5}La_3Ta_{0.5}Zr_{1.5}O_{12}$	Mother Powder	1140°C x 16h	Ambient Air	Alumina	cubic	88	4	[130]
0.25Al-LLZO	Mother Powder	1200°C x 24h	Ambient Air	Alumina	cubic	89	1.81	[60]
Al-$Li_{6.75}La_3Zr_{1.75}Ta_{0.25}O_{12}$	10mol% Li_2CO_3	1200°C x 4h	Ambient Air	Alumina	cubic	91.1	6.1	[140]
Al-LLZO	Li3BO3	700°C x 5h + 900°C x 36h	Ambient Air	Alumina	cubic	92	1	[113]
$Li_{6.4}La_3$ $Zr_{1.4}Ta_{0.6}O_{12}$	6 wt.% LZO / Mother Powder	1200°C x 2.5h	Ambient Air	Alumina	cubic	92	5.84	[138]
$Li_7La_{2.75}Ca_{0.25}Zr_{1.75}Nb_{0.25}O_{12}$	10% excess $LiNO_3$ / Mother Powder	1050°C x 12h	Ambient Air	Alumina	cubic	92		[141]
LLZO	Mother Powder	1150°C x 6h	Ambient Air		cubic	92	1	[142]
$Li_{6.5}La_3Zr_{1.5}Nb_{0.5}O_{12}$	1.4 wt% B_2O_3 / Mother Powder	1100°C x 6h	Ambient Air	Zirconium	cubic	92.4	1.86	[135]
$Li_7La_{2.75}Ca_{0.25}Zr_{1.75}Nb_{0.25}O_{12}$	-	1050°C x 16h	Ambient Air	Alumina	cubic	93	1.8	[120]
$Li_{6.5}La_3Zr_{1.5}Ta_{0.5}O_{12}$	-	1200°C x 12h	Ambient Air	MgO	cubic + LZO	93.3	4.17	[21]
$Li_{6.4}La_3Zr_2Ta_{0.6}O_{12}$	Li_3BO_3	1000°C x 24h	Ambient Air	-	cubic	93.4	5.47	[132]
$Li_{6.4}La_3Zr_{1.4}Ta_{0.6}O_{12}$	Mother Powder	1250°C x 40 min	Ambient Air	Pt	cubic	94	6.35	[109]
Al-$Li_{6.75}La_3Zr_{1.75}Ta_{0.25}O_{12}$	10 mol% LiOH	1100°C x 4h	Ambient Air	Alumina	cubic	94.1	9.28	[140]
$Li_{6.5}La_3Ta_{0.5}Zr_{1.5}O_{12}$	Mother Powder	1150°C x 20h	Ambient Air	Alumina	cubic	94.5	3.87	[25]
$Li_{6.4}La_3Zr_{1.4}Ta_{0.6}O_{12}$	-	1250°C x 40 min	Ambient Air	MgO	cubic	95	6.32	[109]
$Li_{6.5}La_3Zr_{1.5}Ta_{0.5}O_{12}$	-	1320°C x 0.5h	Ambient Air	MgO	cubic	95.6	5.31	[21]
0.25Al-LLZO	Mother Powder	1200°C x 24h	Ambient Air	Pt	cubic	96	4.48	[60]
$Li_{6.4}La_3Zr_{1.4}Ta_{0.6}O_{12}$	6 wt% MgO	1280°C x 20mins + 1180°C x 5h	Ambient Air	Pt	cubic	97	7.3	[27]
$Li_{6.75}La_3Zr_{1.75}Ta_{0.25}O_{12}$	6wt% Li_2O	1170°C x 6h	Ambient Air	Alumina	cubic + $Li_{0.5}La_2Al_{0.5}O_4$	97.2	6.4	[133]
$Li_{6.3}La_3Zr_{1.65}W_{0.35}O_{12}$	2 wt% CuO	1120°C x 6h	Ambient Air	Alumina	cubic	97.6	1.88	[137]
$Li_{6.4}$ La_3 $Zr_{1.4}$ $Ta_{0.6}$ O_{12}	6 wt% MgO	1150°C x 5h	Ambient Air	Pt support inside MgO	cubic	98.2	5.17	[57]

Table 13: Literature comparisons of sintering conditions of thin-film LLZO solid electrolyte.

Composition	Additives/ Excess Li	Thickness of SE (µm)	De-binding Conditions	Sintering Conditions	Atmosphere	Crucible Type	Phase	Relative Density (%)	Total Conductivity ($x10^{-4}$ S/cm)	Ref
Al-LLZO	Acrylic pore former	65	600°C	1100°C x 20s	Ar	Alumina + Graphite/carbon plate sandwich	cubic	50	0.32	[143]
LALZO	25 wt% Excess Li (LiOH)	< 200	600°C x 12h	1100°C x 12h	Ar	Alumina + Graphite Sandwich	cubic	90	-	[95]
$Li_7La_3Zr_{1.75}Nb_{0.25}Al_{0.1}O_{12}$	0.5 wt% Li_3BO_3	150–175	650°C x 1h	1000°C x 6h	Ar	Alumina + Graphite Sandwich	cubic	90.8	2.82	[20]
$Li_{6.25}Al_{0.25}La_3Zr_2O_{12}$	5 wt% MgO / 5 wt% Li_2CO_3	200	700°C x 2h	1115°C x 3h		Alumina + Graphite Sandwich	cubic	91	2.3	[118]
$Li_{6.45}Al_{0.05}La_3Zr_{1.6}Ta_{0.4}O_{12}$	-	50-240	-	1175°C x 10h	Air	Alumina	cubic	92.8	3.9	[110]
$Li_{6.25}Al_{0.25}La_3Zr_2O_{12}$	-	<30	-	1090°C x 1h	Air		cubic	94	2	[144]
Al-LLZO	Li_2CO_3	< 35	600°C (air)	1100°C x 15 mins	N_2	Carbon + Graphite Sandwich	cubic	95	0.19	[96]
$Li_{6.25}Ga_{0.25}La_3Zr_2O_{12}$	50 wt% Li	25	-	1130°C x 0.3h	N_2	Graphite Sandwich	cubic	95	1.3	[59]
$Li_{6.4}La_3Zr_{1.4}Ta_{0.6}O_{12}$	1.2 wt% Li_2O / Mother Powder	200	650°C x 1h	1100°C x 6h	Air		cubic	99	5.2	[119]
$Li_7La_{2.75}Ca_{0.25}Zr_{1.75}Nb_{0.25}O_{12}$		~50	700°C x 4h	1050°C x 16h	Air	-	cubic	99	2.12	[115]
Al-LLZO	5 wt% Li_2CO_3	50	600°C x 2h (air)	1150°C x 15 mins	N_2	Carbon + Graphite Sandwich	cubic		6.4	[120]
LLZTO	10 wt% LiOH	~200	700°C x 12h	1100°C x 1.5h	Ar	Graphite + MgO plate sandwich in a MgO	cubic	95	2	This Work

As mentioned in previously, ceramics are typically processed with binders within the green body. The de-binding process eradicates the binder to increase densification of the final part [5]. This is typically performed at a lower temperature than the sintering temperature suitable for the specific binders used [145].

It can be concluded LLZO thin-films require more excess Li, lower sintering temperature, and longer sintering duration in comparison to bulk LLZO counterparts. Notably, a de-binding step is introduced in thin-film sintering and the set-up involves using graphite sheets to prevent reactions between crucible and LLZO green parts. The additives are added within the green body. The alumina plates are used to keep the green part from warping during sintering. The sintering set-up for bulk parts is presented to be simpler as fewer challenges are reported.

Excess Li source

A study conducted by Liu et al. highlights the advantages of employing an excess of Li when synthesizing Ta-doped LLZO within alumina crucibles. The following key points are outlined in their work [130]:

(1) The precise quantity of necessary Li is indeterminate, thus the required excess Li to offset this loss remains largely qualitative. Differing quantities of excess Li salts can lead to deviations in the stoichiometric Li ratio [8].
(2) The incorporation of Li_2O as an additive yield augmented density for Ta-doped LLZO and enhances ionic conductivity.
(3) The presence of aluminum contamination originating from alumina crucibles is noted to affect sinterability. The use of Li salt results in a melt phase involving alumina from the crucible, thereby influencing the properties of the sintered LLZO.

To compensate for the excess Li loss during high-temperature heating of LLZO, Li sources like Li_2CO_3 and LiOH are commonly used. Nonetheless, most studies have documented adverse impacts of Li_2CO_3, where densely packed structures coated with Li_2CO_3 exhibit diminished ionic conductivity. In a study by Ren et al., a comparison was made between the effects of Li_2CO_3 and LiOH-H_2O as excess Li sources in Al-LLZO pellets. The findings concluded that LiOH-H_2O yields a purely cubic garnet structure, displaying a more spherical and narrower particle size distribution compared to pellets with excess Li_2CO_3 as show in Figure 29 [140].

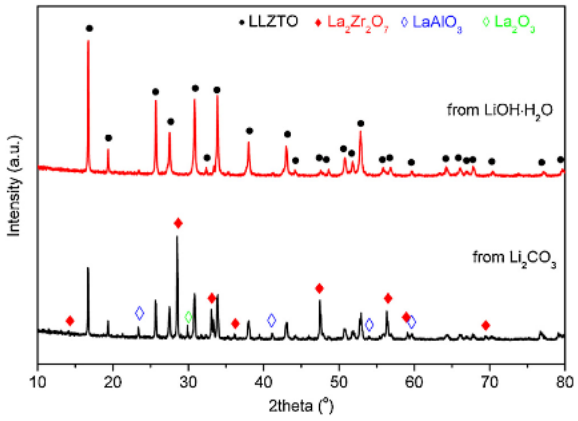

Figure 29: XRD patterns for calcinated Al-LLZO powders from 10 wt% of different Li salt calcinated at 900°C for 6h; Retrieved from [140].

2.4.3 Relationship between composition, microstructure, and properties

The microstructure and composition of LLZO ceramics wield a substantial impact on chemical stability, interface resilience, and mechanical robustness. A preference exists for larger grain boundaries, as they correlate with improved chemical and electrochemical stabilities [146]. It's noteworthy that the choice of crucible employed during sintering can also exert an influence on the resulting grain sizes and boundaries in sintered pellets. Xia et al. demonstrated LLZO pellets sintered in Pt crucibles exhibit superior characteristics compared to those sintered in alumina crucibles. This advantage shown are a higher relative density, larger grain sizes, and fewer grain boundaries, ultimately leading to a heightened ionic conductivity even after exposure to ambient air [60].

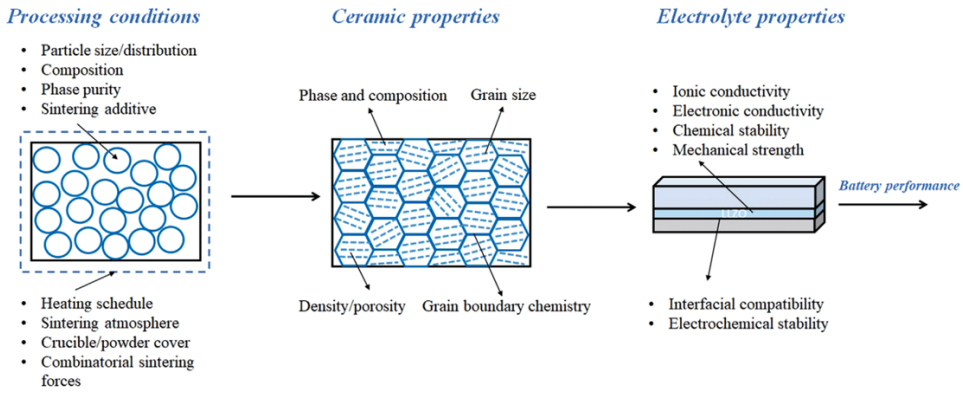

Figure 30: Processing route for ceramic electrolytes. Retrieved from [19].

On the contrary, some studies suggest that LLZO SE should have smaller grains and multiple grain boundaries for successful performance [147].

In summary, the sintering process is critical in successful preparation of a ceramic electrolyte. Therefore, the processing challenges including poor sinterability from Li loss at high temperatures, and sintering environment and set-up need to be resolved to achieve a high density LLZO SE with the desired cubic crystal phase.

2.5 Summary

In summary, this chapter described the state of the art and literature review for the solid-state Li-ion battery, AM of batteries, particle ink synthesis and post-processing sintering of LLZO SE. Additionally, it provides background information required to meet the set objectives of this study.

Chapter 3 Methodology

3.1 Preparation of the LLZO Ink

In this study, Ta-doped LLZTO garnet powder ($Li_{6.4}La_3Zr_{1.4}Ta_{0.6}O_{12}$, referred to as LLZTO) (Ampcera™, MSE Supplies, Tucson, AZ, USA) was procured. The average particle size of LLZTO was 500 nm and the powder density was 5.5 gcm^{-3}. These particles were used to formulate an electrolyte ink with a 3:7 ratio of alpha-terpineol (99%, Alfa Aesar, Haverhill, MA, USA) and n-butanol (99%, Alfa Aesar, Haverhill, MA, USA). The dispersant of choice was Menhaden Fish oil (Z-3, Tape Casting Warehouse, Morrisville, PA, USA), binder of choice was polyvinyl butyral (B-98, Tape Casting Warehouse, Morrisville, PA, USA) and plasticizer of choice was butyl benzyl phthalate (S-160, Tape Casting Warehouse, Morrisville, PA, USA). The list of materials and suppliers are presented in Table 14. Additionally, a 0.7 mm Ta-LLZO garnet pellet (Ampcera™, MSE Supplies, Tucson, AZ, USA) was purchased for comparison of phase and microstructure characterization.

Table 14: Summary of chemical list and manufacturers.

Material	Purchased From
Ta-doped Lithium Lanthanum Zirconium Oxide (LLZTO)	MSE Supplies
Menhaden Fish Oil (MFO)	Z-3, Tape Casting Warehouse
Alpha-Terpineol (αT)	99%, Alfa Aesar
n-Butanol (nB)	99%, Alfa Aesar
Polyvinyl Butyral (PVB)	B-98, Tape Casting Warehouse
Butyl Benzyl Phthalate (BBP)	S-160, Tape Casting Warehouse

A process flow chart describing the ink synthesis process is shown in Figure 31. The materials and process were adopted form McOwen et al. [9]. Firstly, the solvents were combined with dispersant using magnetic stirring to incorporate the fish oil evenly in the ink before dispersing the LLZTO SE powder. This is done in small batches to ensure even distribution of the solid powder in the precursor eliminating large agglomerates. The precursor was mixed using planetary centrifugal mixer (ARE-310, THINKY, Laguna Hills, CA, USA) at 2000 rpm for 3 minutes. Finally, calculated amounts of binder and plasticizer are added to the slurry precursors before ball milling at low rpm with zirconia milling media (10 mm and 5 mm) for 24 hours. This process is done in careful steps to ensure, the ink is homogenous without the presence of

large agglomerates that can impede printing smoothly. The ink formula optimization was done in multiple phases. Phase 1 describes the initial testing of the ink. Phase 2 evaluates the rheological properties. Phase 3 outlines the final ink composition suitable for DIW processing. Phases 4 and 5 demonstrate the solid loading relationship to layer thickness and adding excess LiOH within the ink for Li compensation.

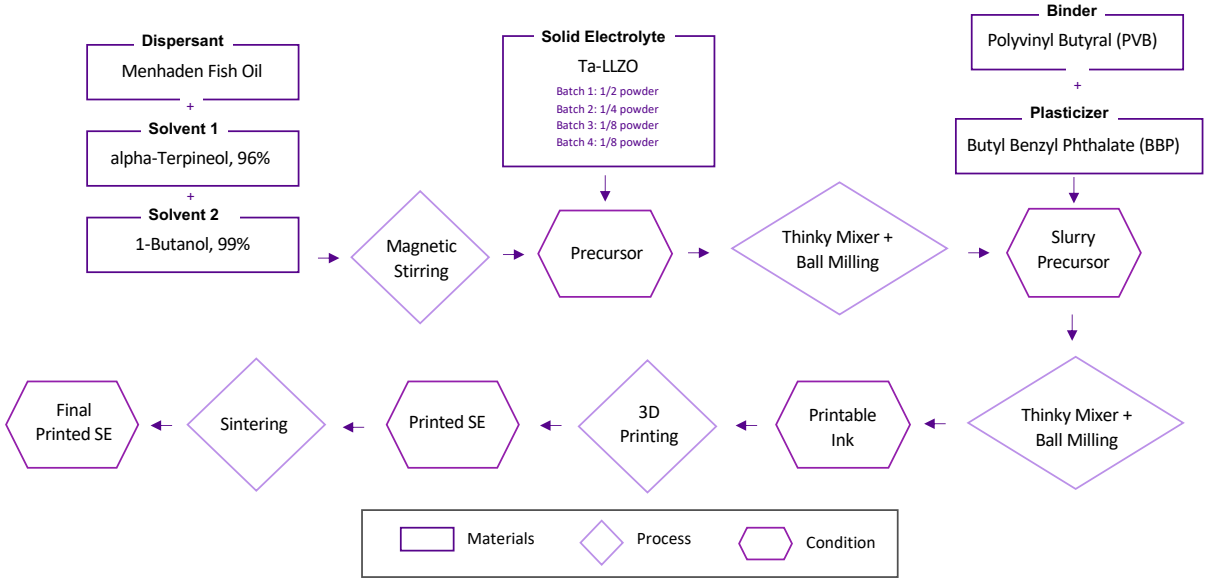

Figure 31: Process flowchart for LLZTO ink synthesis adopted from [14].

Exploration of Ink Components & Behavioral Changes

The ink formula was optimized via a series of experiments observing the ink behavior during DIW printing and drying. The ink compositions A to I tested are outlined in Table 15.

Table 15: Ink Composition A to I.

	Ink Composition (wt%)								
	A	**B**	**C**	**D**	**E**	**F**	**G**	**H**	**I**
LLZTO	45	47.74	47.74	47.74	43.8	30	35	35	35
MFO	0.5	0.65	0.65	0.65	0.25	0.2	0.35	0.35	0.35
αT	14.9	3.65	11.8	11.62	13.1	17.1	18.2	17	15.8
nB	34.6	35.65	27.71	27.1	30.45	39.8	42.5	39.66	36.86
PVB	3.1	7.44	7.44	6.45	6.45	6.45	2	4	6
BBP	1.9	4.56	4.56	6.45	6.45	6.45	2	4	6

Ink Rheology

Examining the ink rheological properties can be useful to determine the behaviour of the ink during high shear rates. The ink compositions with varying binder and plasticizer (B+P) content used for the measurements is outlined in Table 16. The varying ink compositions were synthesized by Cara Kolb at the TUM School of Engineering and Design (Garching bei München, Germany).

Table 16: Ink compositions for rheological studies.

	R-4 wt% B+P	**R-6 wt% B+P**	**R-8 wt% B+P**	**R-10 wt% B+P**	**R-12 wt% B+P**
LLZTO	30	30	30	30	30
MFO	0.15	0.15	0.15	0.15	0.15
αT	7	7	7	7	7
nB	16.33	16.33	16.33	16.33	16.33
PVB	2	3	4	5	6
BBP	2	3	4	5	6

Optimized Ink Formula

The optimized ink formula considered the observations and conclusions drawn in ink synthesis phase 1 and 2. A solid loading of 30-35 wt% is suitable with 1 wt% dispersant content with respect to LLZTO particles. The alpha-terpineol to n-butanol solvents ratio is 3:7 while the binder to plasticizer ratio is 1:1. The optimized ink formulation can be found in Table 17. It is noted the optimized ink formula with 30 wt% solid loading is used to collect data for the volumetric flow rate model and the LLZO drying study. The optimized ink formula with 35 wt% is used for sintering studies to increase the density of the SE.

Table 17: Optimized LLZTO ink formula.

Components	**wt%**	**wt%**
LLZTO	30	35
MFO	0.3	0.35
αT	17.0	15.53
nB	39.7	36.23
PVB	6.45	6.45
BBP	6.45	6.45

Solid Loading vs Layer Thickness

The solid loading is shown to have an impact on the layer thickness printed. Therefore, 20, 25, 30, and 35 wt% solid loading of LLZTO particles using the optimized ink formula ratios (outlined in Ink Synthesis – Optimized Ink Formula) were used to study the printed layer thickness.

Excess LiOH within the Ink

To explore Li compensation, lithium hydroxide was incorporated in concentrations of 5, 10, and 20 wt% LiOH at final ink synthesis step. The ink was then ball milled until LiOH to dispersed evenly.

3.2 Casting LLZTO Ink with Mayer Rod

The prepared LLZTO ink was casted on a polyethylene terephthalate (PET) substrate using a 200 µm wire-wound Mayer Rod (Buschman^{TM}, Cleveland, OH, USA) to test the drying properties of the ink before processing with DIW. This casted ink was left to dry in ambient conditions. Ink compositions G-I and inks with LiOH within the ink were casted using the Mayer Rod.

3.3 Direct Ink Writing Printing LLZO Ink

The prepared ink was printed using a pneumatic material extrusion printhead (Optimeter^{TM}, Nordson EFD, Westlake, Ohio, USA) and a controller (ValveMate^{TM} 9000, Nordson EFD, Westlake, Ohio, USA) was used to control the air-pressure for material extrusion. The dispensing nozzle tips used had a precision needle tip or tapered tip geometry. The nozzle diameter for the precision needle tips used were 250 and 350 µm. The nozzle diameter for the tapered tips used were 200, 250, and 400 µm. The LLZTO ink was deposited on a PET substrate in a circular pattern with 13-15 mm diameter. To filter large agglomerates in the ink, a 250 µm mesh is cut and placed within the syringe (Figure A3). The printed SE were then dried in ambient conditions and lifted off the PET substrate.

Printing of Ink Compositions

The ink compositions A-F were extruded through a 250 µm tapered tip applying 2-3.5 bar of pressure. The translation velocity used was 10-50 mm/s.

Volumetric Flow Rate Model

The volumetric flow rate model studied the flow rate of the optimized 30 wt% solid loading ink extruded through 250 and 350 µm precision needle tips, and 200 and 250 µm tapered tips. The schematic diagram for needle and tapered tips is shown in Figure 10. The applied pressure was varied from 0.4 to 3.5 bar. The

area of the LLZTO printed electrolytes was 2.25 cm^2 while the density of the ink was 1.18 g/cm^3. The line speed and time required for print for each nozzle is outlined in Table 18.

Table 18: DIW printing parameters for volumetric flow rate model.

Nozzle Geometry	Nozzle Diameter	Translation Velocity	Time
Precision	250 µm	10 mm/s	25 seconds
Precision	350 µm	25 mm/s	10 seconds
Tapered	200 µm	45 mm/s	6 seconds
Tapered	250 µm	70 mm/s	4 seconds

The mass of the printed LLZTO SE was measured using a precision scale to calculate the volumetric flow using the mass of print (m; g), density of ink (ρ; gcm^{-1}) and time (t; s) required for print (Equation 14).

$$Q = \frac{m}{\rho t} \tag{14}$$

Furthermore, the wet thickness can be calculated using the volume of the printed SE (ΔVolume; cm^3) and area (A; cm^2) of the print (Equation 15).

$$t = \frac{\Delta Volume}{A} \tag{15}$$

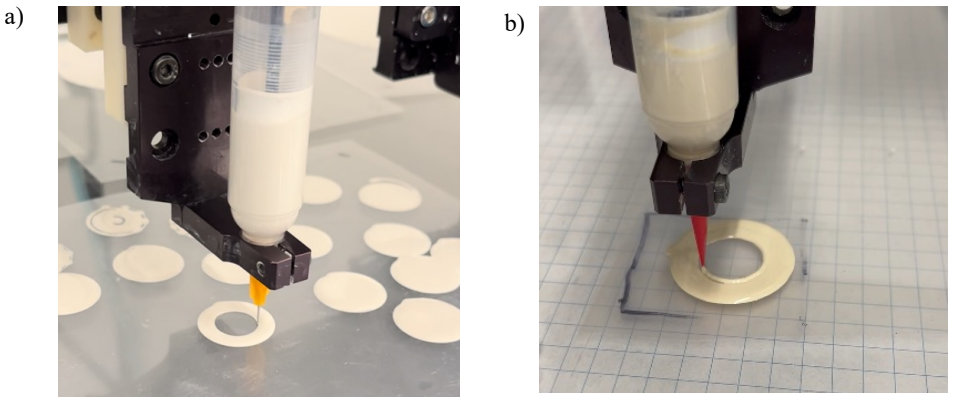

Figure 32: Optical image of DIW of LLZTO ink with a) 350 µm needle tip and b) 250 µm tapered tip.

Solid Loading vs Height

The 20, 25, 30, and 35 wt% solid loading of LLZTO particles using the optimized ink formula ratios (outlined in Ink Synthesis – Optimized Ink Formula) were fabricated using 250 µm tapered tip applying 3.5 bar of pressure. The translation velocity set was 20 mm/s.

The wet thickness describes the thickness of ceramic electrolyte immediately after printing or casting with a Mayer rod. The dry thickness describes the thickness of ceramic electrolyte after drying in air or vacuum oven to evaporate majority of the solvents.

LLZO Drying Study

A drying study was done after printing LLZTO SE to investigate the drying behaviour and time. The optimized 30wt% solid loading ink was printed with the 250 µm tapered tip applying 2-3.5 bar of pressure. The translation velocity used was 10-50 mm/s. The LLZTO printed pellets were left to dry over a 45-hour period on the PET substrate in ambient air conditions or dried in the convection oven (Binder, FD023UL-120V, Tuttlingen, Germany) at 50℃ for comparison.

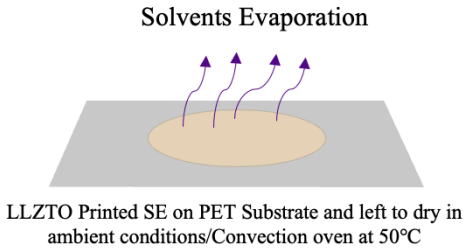

Figure 33: Schematic illustration of the drying process of printed LLZTO ceramic part.

3.4 Powder Pressing Bulk LLZO Pellets

The LLZTO garnet powder was compacted into bulk pellets with a diameter of 12.7 mm and a thickness of approximately 1 cm, applying 200 to 400 MPa of pressure (Figure A1). Additionally, a small quantity (~10 µL) of alpha-terpineol was used as a binder to wet the particles of LLZTO powder for compaction.

3.5 Sintering of the LLZO Electrolyte

3.5.1 LLZO Bulk Pellets

The bulk pellets were sintered within an alumina boat (100x20x20 mm) or MgO crucible (12 mL; 40x40x15 mm) within a tube furnace (GSL-1600×, MTI Corporation, Richmond, CA, USA) using the sintering conditions outlined in Table 19. The bulk pellets were buried within Mother powder (LLZTO powder) to compensate for the Li loss phenomenon.

Table 19: Bulk LLZTO pellet sintering conditions.

	Sintering Conditions	Excess Li Source	Crucible
1	1200℃ x 24h	Mother Powder	Alumina + lid
2	1200℃ x 12h	Mother Powder	Alumina + lid
3	1200℃ x 1h	Mother Powder	Alumina + lid
4	1250℃ x 1h	Mother Powder	MgO + lid
5	1230℃ x 0.75h	Mother Powder	Alumina + lid
6	1320℃ x 0.5h	-	Alumina + lid

3.5.2 LLZO Printed/Casted SE

Sintering Phase 1: LLZTO Sintering with Mother Powder

The 200 µm LZZTO casted film and 3D printed 300 µm SE were subjected to de-binding and sintering within a capped 12 mL MgO crucible with excess mother powder (LLZTO powder) as shown in Figure 34. The de-binding process was performed at 600℃ for 3 hours, with a gradual heating rate (1℃/min) followed by sintering at 1200℃ for 3 hours with a fast-heating rate (10℃/min). This heating process was performed in the tube furnace.

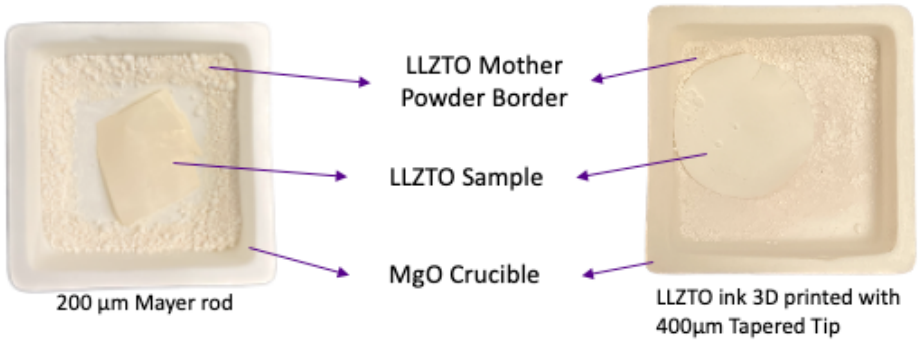

Figure 34: Optical image of 200 µm LLZTO casted film and 3D printed 300 µm SE sintering set-up in MgO crucible.

Sintering Phase 2: LLZTO Sintering with Excess LiOH within Ink in Ambient Air Conditions

The casted 200 µm LLZTO inks with 5, 10, 20 wt% excess LiOH within the ink were dried and cut to fit in the crucible. The de-binding process involved heating at 600°C for 12 hours, and sintering was carried out at 1200°C for 12 hours in ambient air. The heating rate set was 3°C/min to 600°C and 10°C/min to 1200°C. This heating process was performed in the tube furnace.

The sintering setup used in these experiments is illustrated in Figure 35. In this setup, the LLZTO ceramic electrolyte is placed between graphite sheets to prevent it from adhering to alumina or MgO plates. Although MgO is known to be inert to LLZTO, even small impurities on the surface can cause the SE to react with the MgO and adhere to it. The graphite sheet also acts as a buffer between the alumina or MgO plates, maintaining the ceramic electrolyte's flatness to prevent warping.

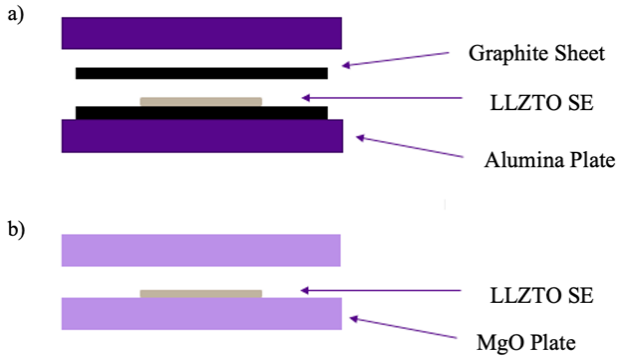

Figure 35: Schematic diagram of LLZTO films sintering set-up with a) graphite/alumina plates and b) MgO plates.

Sintering Phase 3: Exploring Sintering Time

The casted 200 µm LLZO SE with 5 wt% LiOH within the ink was heat processed using Condition A and Condition B under a high-purity argon gas flow as shown in Table 20. The heating rate to de-binding temperature was set to 3°C/min while the heating rate to sintering temperature was set to 10°C/min. This heating process was performed in the tube furnace using the graphite sheet and alumina plate sandwich as described in Figure 35a.

Table 20: LLZTO de-binding and sintering parameters for condition A and B.

	De-binding Temperature	De-binding Duration	Sintering Temperature	Sintering Duration
Condition A	700°C	4 h	1200°C	1.5 h
Condition B	600°C	12 h	1200°C	12 h

Sintering Phase 4: LLZTO Sintering with Excess LiOH within Ink in Argon

The 0, 5, 10, 20 wt% excess LiOH within the LLZTO ink casted SE film was heat processed with 2°C/min to 700°C followed by sintering at 1200°C for 1.5 hours with a 10°C/min heating ramp in argon atmosphere. This was done in a furnace (Pro Press 100, Whip Mix, KY, USA) using the graphite sheet and alumina plate sandwich as described in Figure 35a.

Sintering Phase 5: LLZTO Sintering with Excess LiOH in Crucible in Argon

The 0, 5, 10, 20 wt% excess LiOH was added to edges of the MgO crucible as the 3D printed LLZTO SE was heat processed with 2°C/min to 700°C followed by sintering at 1200°C for 1.5 hours with a 10°C/min heating ramp in argon atmosphere. This was done in a furnace (Pro Press 100, Whip Mix, KY, USA) using simple sintering method shown in Figure 36.

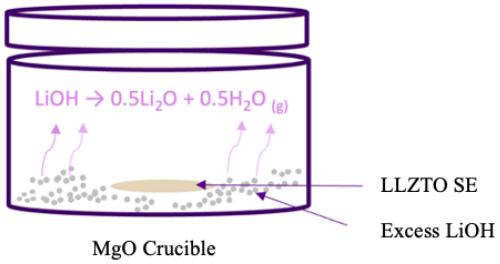

Figure 36: Schematic diagram of LLZTO sintering in MgO with excess LiOH in crucible.

Sintering Phase 6: Optimizing Sintering of Printed LLZTO SE

The dried LLZTO SE was heated to approximately 60-70°C on a hotplate and pressed with 3.8 Ton weight using a laboratory press (YLJ-15L/15S, MTI Corporation, Richmond, CA, USA) to improve the green density. Then, cut to ½ inch diameter to prevent warping during thermal heating process (Figure 37).

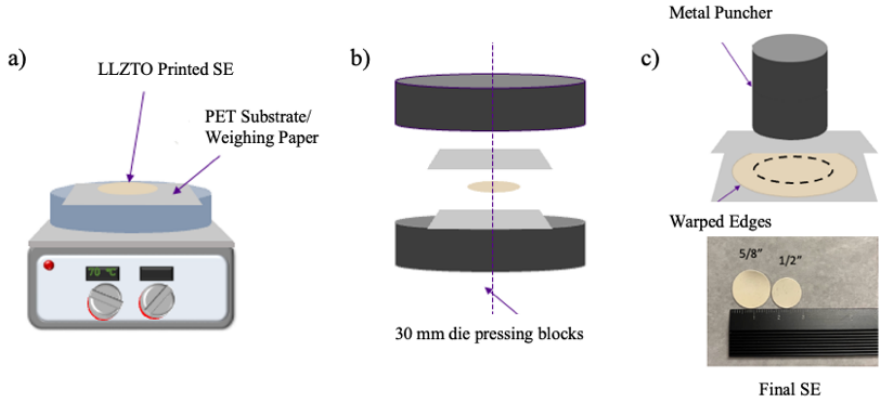

Figure 37: Schematic diagram of preparing printed LLZTO SE for sintering; a) heating on hot plate at 70°C, b) pressing using die pressing blocks for at 3.8 Ton weight, and c) punching SE to 1/2-inch diameter.

The pressed and cute printed LLZTO were subjected to a sintering process within a temperature range spanning 1000°C to 1250°C, over durations of 1.5 or 6 hours, all under a flowing argon gas (~ 3 L/min) atmosphere. This process was done within a muffle furnace (GCF1400-6X6X6, Across International, Livingston, NJ, USA). To prevent deformation, these prepared LLZTO pellets were enclosed between MgO plates and graphite sheets within the MgO crucible and excess LiOH was added to border of crucible to facilitate Li rich environment (Figure 38, Figure A8). An additional step, involving a de-carbon process at 650°C for 12 hours in flowing compressed air, was implemented to eliminate any residual graphite contamination present on the final sintered LLZO ceramic.

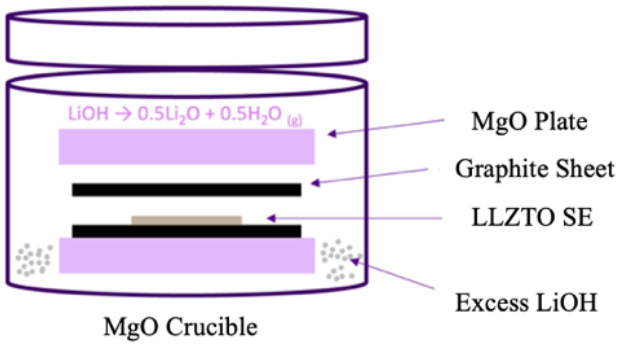

Figure 38: Schematic diagram of optimized LLZTO sintering in MgO with excess LiOH in crucible.

3.6 Material Characterization

3.6.1 Rheology

The rheological behavior of the 30 wt% solid loading LLZTO ink with varying binder and plasticizer content as described in Section 3.1 – Phase 2 using a rotational rheometer (Kinexus lab+, Netzsch, Selb, Germany). A 40 mm plate-plate geometry with a gap distance adjusted to 0.1 mm was used. Each measurement was conducted at ambient temperature to examine the shear-dependent flow behaviour for the various LLZTO inks. The Herschel-Bulkley model was employed to analyze and fit the data (Equation 2). This data was collected by Cara Kolb at the TUM School of Engineering and Design (Garching bei München, Germany).

3.6.2 Crystal Phase (XRD)

The x-ray diffraction (XRD) analysis was conducted with an x-ray diffractometer (Miniflex II, Rigaku, Tokyo, Japan) to analyze the crystal phases of LLZTO material before and after heat treatment. The scan speed set was 1°/min with 0.03° step increments between 10-60°. The crystal phases were analyzed using the DIFFRAC.EVA software (Bruker, Billerica, MA, USA). The relative intensity ratio (R value) is adopted to characterize the impurity LZO peak relative to LLZTO cubic phase peak (Equation 16).

$$\%\mathrm{LZO} = \left(\frac{\mathrm{I_{LZO}}}{\mathrm{I_{LLZTO}}}\right) \mathrm{x}\ 100\% \tag{16}$$

3.6.3 Au Coating

The surface of LLZTO SE was Au coated by ion-sputtering instrument (E5100, Polaron Instruments, London, England). The sputtering was conducted using 20 mA current for 2 minutes for SEM samples and 20 mA current for 5 minutes for EIS samples on each surface of SE. This process deposits 30 nm of Au on SEM samples and 75 nm of Au on EIS samples providing a conductive pathway for ions to travel. During sputtering for EIS samples, tape was used on edges to avoid an edge short circuit.

3.6.4 Fracture Surface Morphology (SEM)

The microstructure for the fracture surface was analyzed using a scanning electron microscopy (SEM) (Vega3, Tescan, Brno, Czechi). The SEM images can analyze the grain growth during high-temperature sintering and examine the porosity. A highly dense SE with minimal porosity is desired.

3.6.5 Density

The density of the sintered SE was measured using the Archimedes method in a deionized water standard at room temperature.

3.6.6 Phase Transitions & Mass Loss (DSC/TGA)

The phase transitions and mass loss were analyzed using differential scanning calorimetry (DSC) and thermogravimetric analysis (TGA) (STA 449 F1 Jupiter, NETZSCH, Selb, Germany).

DSC/TGA Phase 1: DSC analysis on LLZTO powder

To gain further insights into the phase transition of LLZTO during sintering, DSC was employed on commercial powder under a compressed air atmosphere. This analysis aimed to examine the exothermic and endothermic reactions during sintering. The heating rate was set to 5°C per minute reaching 1300°C with a compressed air flow of 20 mL/min. Nitrogen was used as a protective gas with flow of 20 mL/min.

DSC/TGA Phase 2: TGA Analysis to Optimize De-Binding Parameters

The mass loss from a TGA curve can be used to determine the temperature and duration required for the de-binding process in 20 mL flowing argon atmosphere. Argon was also employed as the protective gas with flow of 20 mL/min. Table 21 outlines the ramp and isothermal heating steps to evaluate the de-binding temperature and duration.

Table 21: TGA heating parameters to optimize de-binding parameters.

	Ramp 1	Isothermal	Ramp 2	Isothermal	Ramp 3
Evaluate de-binding temperature	1°C/min to 250°C	250°C x 2 h	3°C/min to 1200°C	-	3°C/min to 20°C
Evaluate de-binding duration	1°C/min to 250°C	250°C x 2 h	3°C/min to 750°C	750°C x12 h	3°C/min to 20°C

3.6.7 Electrochemical Properties (EIS)

A two-electrode Swagelok cell (PFA 14 mm diameter and 50 mm rod, Swagelok Ontario, Mississauga, ON, Canada) with symmetric ion-blocking was employed to test the electrochemical properties. The electrochemical impedance spectroscopy (EIS) data was collected on the potentiostat (SP-300, BioLogic, Seyssinet-Pariset, France) in Professor Michael Pope's lab (chemical engineering, University of Waterloo) to test the impedance ranging from 10 Hz to 6MHz. In-Au-LLZTO-Au-In symmetric battery was assembled using Au sputtering and ~75 µm Indium foil (99.99%, Sigma-Aldrich, Missouri, USA).

The Swagelok cell can be placed in a 3D printed compression jig to apply a load between 0-50 kgF improving the contact between the electrodes and electrolyte (Figure 39a). The compression jig was designed and printed by Professor Saeed Maleksaaedi at the Multi-Scale Additive Manufacturing Lab (University of Waterloo, Canada). This configuration, implemented with a Swagelok cell, facilitates the data acquisition necessary for calculating the ionic conductivity, as defined by the equation 17. The metal electrodes of the Swagelok cell were wrapped with Cu foil and connected the potentiostat alligator clips (Figure 39b).

$$\sigma = \frac{I}{R_{total}A} \tag{17}$$

Where, R_{total} is the total resistance (Ω) of the electrolyte sample, I is the sample thickness (cm), and A is the area (cm^2).

a) b)

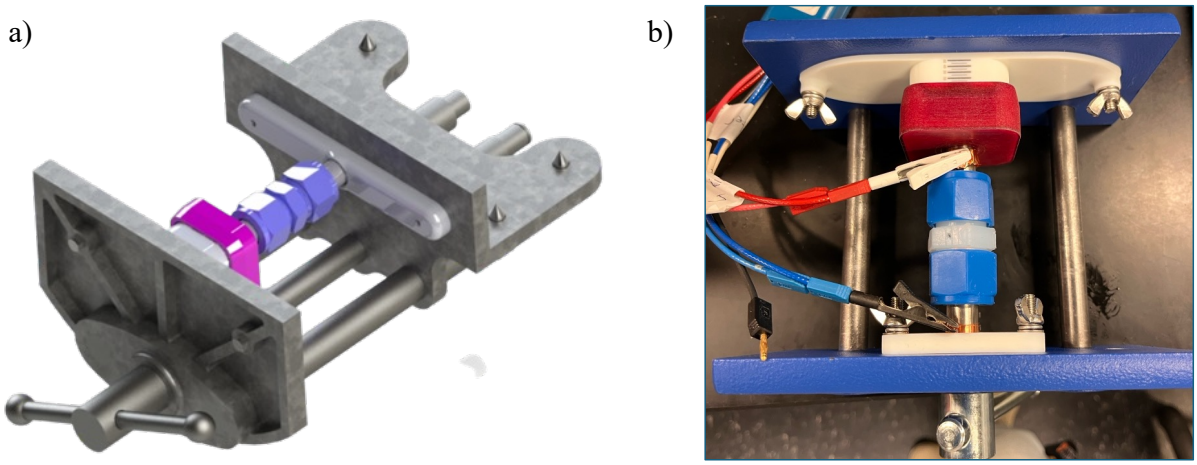

Figure 39: a) Rendered design for 3D printed compression jig; b) Swagelok cell placed in between the 3D printed compression jig.

To further study the ionic conductivity at various temperatures (30, 40 and 50°C). The temperature-dependent conductivities can linearly fit on a ln**σ** vs. 1/T plot (Arrhenius plot) where E_a, K_b, and T are activation energy (eV), Boltzmann constant (JK^{-1}) and absolute temperature (K).

$$\sigma = \sigma_o e^{\frac{E_a}{K_b T}} \tag{18}$$

Chapter 4 Results & Discussion

The contents in this chapter include results for each ink synthesis, DIW printing, a high-temperature sintering.

4.1 Ink Synthesis

4.1.1 Exploration of Ink Components & Behavioral Changes

The ink components were varied, and the behaviour of the ink is observed. The printed ceramic electrolytes were characterized by two tests. The first test involves examining the ceramic electrolyte of any cracks while the second test involved removing the ceramic part off the PET substrate. The results for ink composition A through F are shown in Figure 40.

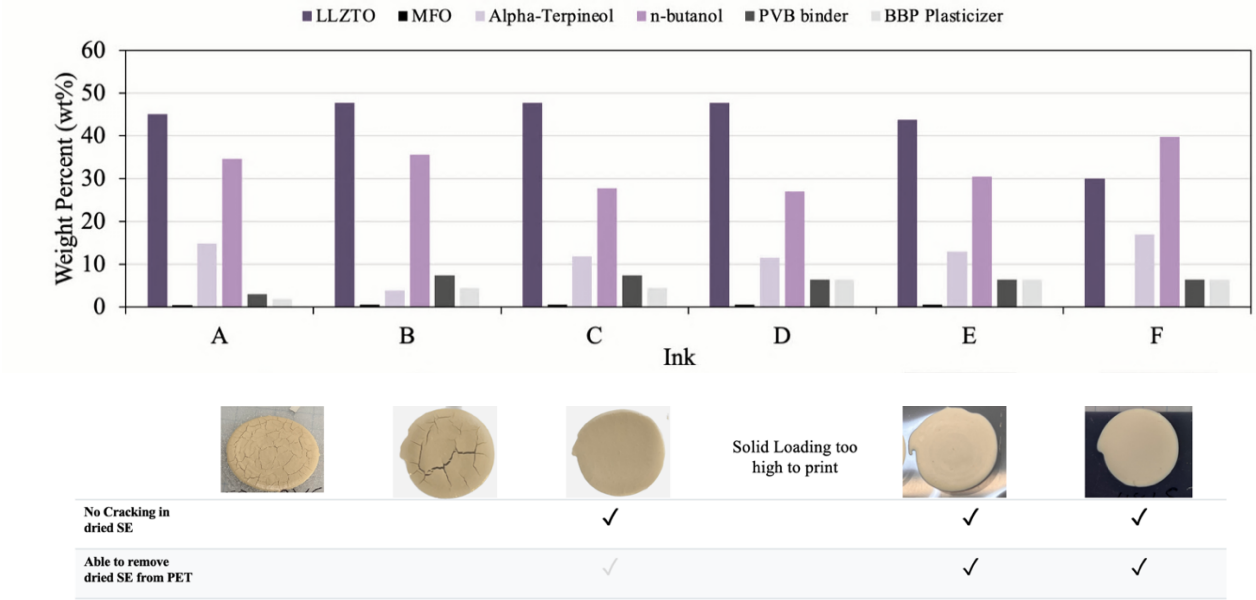

Figure 40: LLZTO ink compositions A-F tested via DIW printing.

Solvent Ratios

The solvent mixture consisting of alpha-terpineol, and n-butanol was maintained at a constant ratio of 3:7, as recommended by McOwen et al. [9]. This solvent ratio, characterized by specific physical properties, is crucial for preventing cracks during the drying process (Table 22). The differential vapor pressures of these solvents play a key role. N-butanol, with its higher vapor pressure of 0.67 kPa at 20°C, facilitates rapid

drying, while alpha-terpineol, with its lower vapor pressure of 0.0037 kPa at 20°C, encourages particle rearrangement during the drying phase.

Surface tension, defined as the force acting along the surface of a liquid droplet to minimize surface area and maintain a spherical shape, is also a relevant factor. Alpha-terpineol possesses a slightly higher surface tension of 33.2 dynes/cm compared to n-butanol, which has a surface tension of 25 dynes/cm. Consequently, the presence of alpha-terpineol in the ink is necessary to promote the ink's 3D behavior and prevent excessive spreading. Moreover, the lower vapor pressure and higher boiling point of alpha-terpineol make it an ideal solvent for facilitating the drying of ceramics, without the occurrence of observed cracks.

Conversely, n-butanol contributes to the faster drying of the printed ceramics. Therefore, maintaining the 3:7 ratio of alpha-terpineol to n-butanol is considered ideal. Deviating from this ratio with a lower concentration of alpha-terpineol could lead to cracking in the printed ceramics. This occurs because n-butanol evaporates rapidly, leaving noticeable pores in the sample, resembling cracks (Figure A4).

Table 22: Physical properties of alpha-terpineol and n-butanol.

	Vapour Pressure at 20°C	Boiling Point	Surface Tension at 25°C
Alpha-Terpineol	0.0037 kPa	219°C	33.2 dynes/cm
n-Butanol	0.67 kPa	117°C	25 dynes/cm

Solid Loading and Binder: Plasticizer Ratio

The solid loading of LLZTO particles in the ink is directly linked to the ink's viscosity. As the solid loading increases, the ink becomes more saturated with ceramic particles, resulting in a rise in viscosity and the formation of larger agglomerates within the ink. Additionally, a higher solid loading extends the synthesis time required for the ink to achieve homogeneity.

A higher solid loading with low amounts of binder and plasticizer can cause cracks during drying as seen in composition A and B. The binder increased the strength of the ink while the plasticizer softened the binder to increase the flexibility of dried SE. The 1:1.6 ratio of the binder and plasticizer used in composition A through C does not provide enough flexibility to the dried SE to successfully remove off the PET without cracking. However, increasing the binder and plasticizer content can mitigate some of the cracks as seen in composition C. It was suggested by Yu Mingxian et al., a 1:1 ratio of binder to plasticizer

increased the strength of the alumina green tapes with the highest green density [97]. Therefore, composition D, E, and F employed a 1:1 ratio of binder to plasticizer to increase the strength of the ink and provide enough plasticizer to soften the binder present in ink. The plasticizer can reduce the PVB glass transition temperature allowing a better microstructure and particle arrangement homogeneity [97]. The high solid loading paired with higher binder and plasticizer content increased the viscosity creating a paste-like ink with large agglomerates. This proved to be unsuitable for DIW through the 250 µm tapered tip. Therefore, decreasing the solid loading as shown in ink composition E and F reduced the viscosity to a suitable range for DIW while mitigating cracks and creating a flexible SE that can be removed from the PET substrate.

To further investigate the effect of amount of binder and plasticizer necessary in the LLZTO ink, composition G-I were studied. Uneven particle distribution in the slurry due to electrostatic forces between slurry particles and the PET film were observed for the casted inks (Figure 41). However, it is observed the thinner wet thickness (200 µm) experiences fewer cracks during drying compared to DIW printed compositions (A-F). Lower quantities of binder and plasticizer, such as 2 wt% for each, were inadequate for producing a casted electrolyte that was both robust and flexible. In such cases, it was impossible to remove the green body from the PET substrate. On the other hand, a higher ratio of binder and plasticizer ensured even distribution of the green body, resulting in greater strength and flexibility. To successfully demold the green body from the PET, a slightly higher binder-to-plasticizer ratio was recommended. Consequently, a final binder and plasticizer content of 6.45 wt% each was established for all future prints. This binder and plasticizer content is higher than reported in tape casting LLZTO inks where 4 wt% PVB and 5 wt% BBP is employed [148].

Figure 41: Optical images of LLZTO ink composition G-I coated on PET with 200 µm wet thickness and dried for 24h.

4.1.2 Ink Rheology

As mentioned in the previous section, it has been observed that the content of binders and plasticizers can significantly impact the viscosity of the ink during process of synthesizing ink. However, it is crucial to include a sufficient amount of binders and plasticizers to impart strength and flexibility to the ink. The rheological behavior of the ink is of utmost importance for achieving successful 3D printing of parts. The flow characteristics of the ink can be effectively described using the Hershel-Bulkley model, particularly evident in a 30 wt% LLZTO ink with varying binder/plasticizer contents. As shear rate is increased, reaching up to 10,000 s^{-1}, there is a gradual increase in shear stress for each of the tested inks. The data collected, as represented in Figure 42, demonstrates a shear rate vs. shear stress curve fitted to the Hershel-Bulkley model. From this, it can be concluded that the LLZTO ink with various binder and plasticizer content exhibits shear-thinning behavior, allowing the ink to be extruded through the DIW nozzle tips at high shear rates. The 12 wt% binder and plasticizer LLZTO ink is deemed suitable for processing with DIW technology achieving high shear stress at high shear rates.

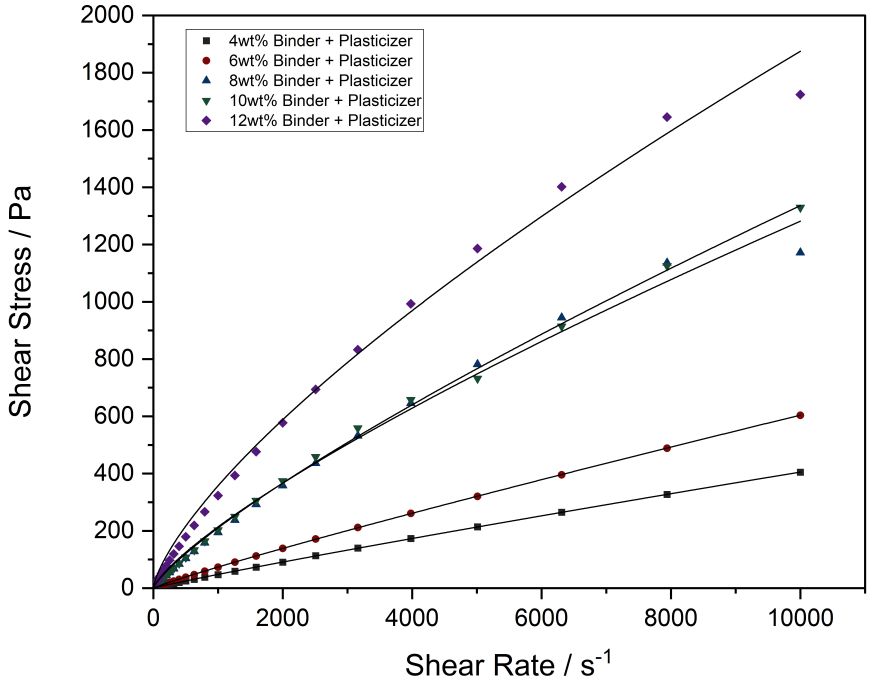

Figure 42: Shear rate sweeps of 30 wt% LLZTO ink with varying binder & plasticizer content.

4.1.3 Ink Synthesis Summary

In summary, the ink synthesis is impacted by the ink materials, their physical property, and the ratios between solvents and binder/plasticizer. Each of the components can affect the ink viscosity, printing, and drying behaviour. Therefore, development of a suitable ink composition for LLZTO SE processing is the first challenge of this study. Although, many formulations exist for tape-casting of LLZTO, no explicit formulation of LLZTO ink suitable for DIW is reported to date. The transparency of ink materials, composition, and synthesis route used in our study aims to help other research groups continue our research further. An optimized ink formulation, combined with the suitable binder-to-plasticizer content, can help mitigate the observed cracking during the drying process. The binder provides strength to the ink whereas the plasticizer enables a flexible film is produced. The flexibility aids to remove the ceramic off the PET substrate after drying. Additionally, the 3:7 ratio between the alpha-terpineol and n- butanol solvents facilitate particle rearrangement to prevent cracks during drying. Hence, the optimized LLZTO ink composition used in our study includes a solid loading of 30-35 wt%, 0.35 wt% MFO dispersant (equivalent to 1 wt% concerning the solid loading), a 3:7 alpha-terpineol to n-butanol ratio, and a 1:1 binder-plasticizer ratio (both at 6.45 wt%).

4.2 Direct Ink Writing

4.2.1 Volumetric Flow Rate Model

Figure 43 depicts the volumetric flow rates of material extrusion rates with respect to pressure applied for the prepared 30 wt% LLZTO ink. The aim of the volumetric flow rate model is to aid in prediction of flow rate, wet thickness, and pressure required to successful print the ceramic electrolyte ink. This provides a critical quantitative understanding of the ink printing behaviour and provides means to find the working windows defined as printable regions (defined as purple regions in Figure 43). These regions help analyze and predict the behaviour of the ceramic ink while dispensing using the various nozzle geometries and tips. This region can be defined by the flow rate and wet thickness desired for each dispensing tip based on qualitative observations such as evenly printed ink without distortion of the structure contour being printed. The needle tips offer precision printing indicating a thinner ceramic can be printed resulting in narrower bounds. On the contrary, a tapered nozzle dispenses material at a higher flow rate increasing thickness of ceramic and providing a larger suitable printable region. The suitable printable region for each of the nozzle geometries tested are defined in Table 23. These ranges were chosen based on desired print properties such as thickness, continuity of print, and avoiding overflowing of ink for desired pattern. It

should be notes a moderate/low extrusion rate is desired to print a greater viscosity ink with fewer pores in the final printed part.

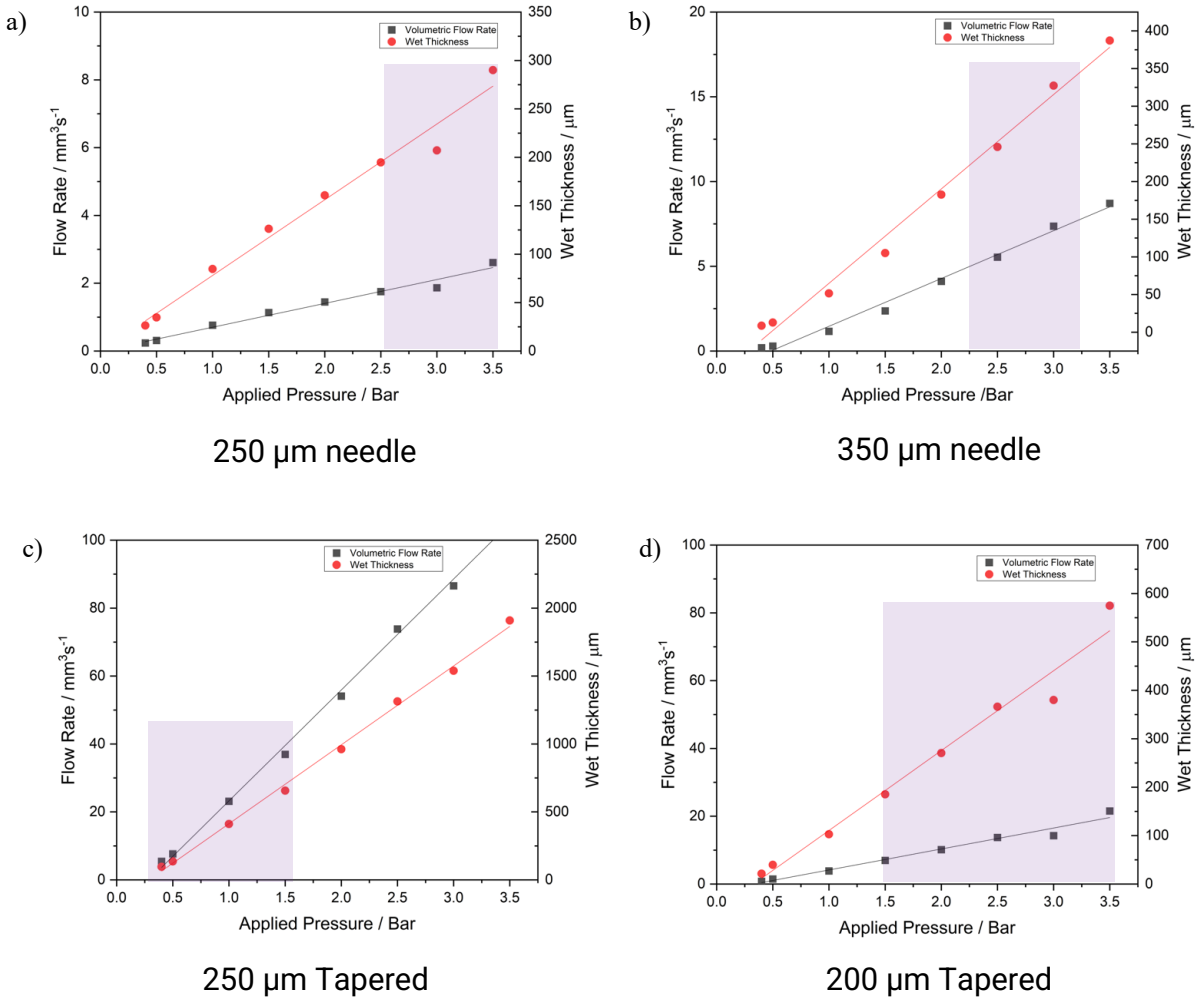

Figure 43: Volumetric flow rate and wet thickness plotted with respect to applied pressure to print 30 wt% solid loading LLZTO ink with a) 250 µm needle tip, b) 350 µm needle tip, c) 250 µm tapered tip, and d) 200 µm tapered tip.

Table 23: Defined suitable printing regions for ceramic ink for various dispensing tips.

Suitable printable region bounds	Flow Rate (mm^3/s)	Wet Thickness (µm)
250 µm Needle	1.5-2.5	200-300
350 µm Needle	5-5.5	250-350
250 µm Tapered	5-45	150-1500
200 µm Tapered	7-20	200-600

4.2.2 Solid Loading vs. Layer Thickness

The quantity of solid material within the ink noticeably impacts the thickness of a printed sample. As depicted in Figure 44, there is a connection between solid loading and the height of each printed layer. The printed layer is defined as the dry thickness of the SE.

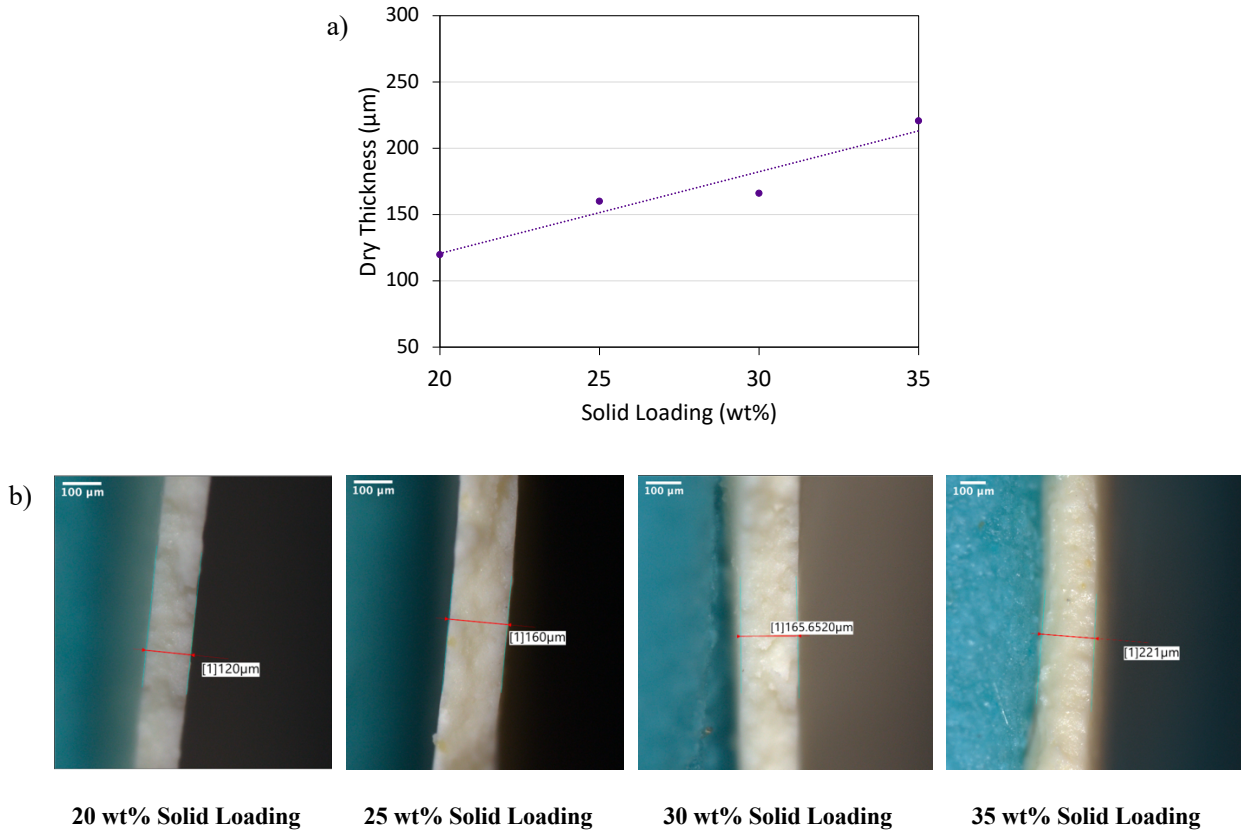

Figure 44: a) Solid loading (wt%) vs dry thickness of printed LLZTO; b) optical cross-sectional images of printed LLZTO ceramics with varying layer thickness.

Ink with lower solid loading is more amenable to being processed through smaller nozzle openings, due to a reduced presence of agglomerates. Nevertheless, it lacks structural integrity during the printing process linked to the lower viscosity of the ink. Conversely, ink with a higher solid loading can present challenges during processing if it contains numerous agglomerates of larger size than the nozzle orifice. However, this higher solid loading ink can increase the final dry thickness of the printed sample and facilitates increased density after the drying and sintering processes [5].

The chosen translation velocity in DIW can influence the continuous filament printing process and layer height. A faster translation velocity is likely to result in a thinner layer height when compared to a slower translation velocity. It is crucial to configure this parameter in alignment with the specific characteristics of the ink and the applied pressure.

The 30 or 35 wt% solid loading presents a layer thickness of 165 – 221 µm dry thickness when fabricated using 250 µm tapered tip applying 3.5 bar of pressure and 20 mm/s translation velocity. When sintered, the printed SE are expected to experience 30 – 45% shrinkage in thickness. This is evaluated from the sintering data presented in section 4.3. Therefore, the higher solid loading impacting the layer thickness meets the research objective to achieve 150 - 250 µm thick ceramic electrolyte.

4.2.3 Printed LLZTO Ceramic Drying Study

An essential aspect of achieving a successful ceramic print lies in the drying process (Figure 45). It can be deduced that a thinner green body will dry more quickly due to its higher surface area-to-volume ratio, while a thicker green body with the same lateral dimensions will dry at a slower rate.

Figure 45 illustrates the point in time when, theoretically, n-butanol and alpha-terpineol are completely evaporated under ambient air conditions or in a convection oven at 50°C. It is evident that evaporating the solvents from the green body in ambient air takes approximately more than 45 hours. In contrast, subjecting the green body to a convection oven at 50°C requires approximately less than 10 hours to achieve the same result. This insight is useful in accelerating the drying process when necessary and offers critical information about the green body's readiness for the succeeding sintering process.

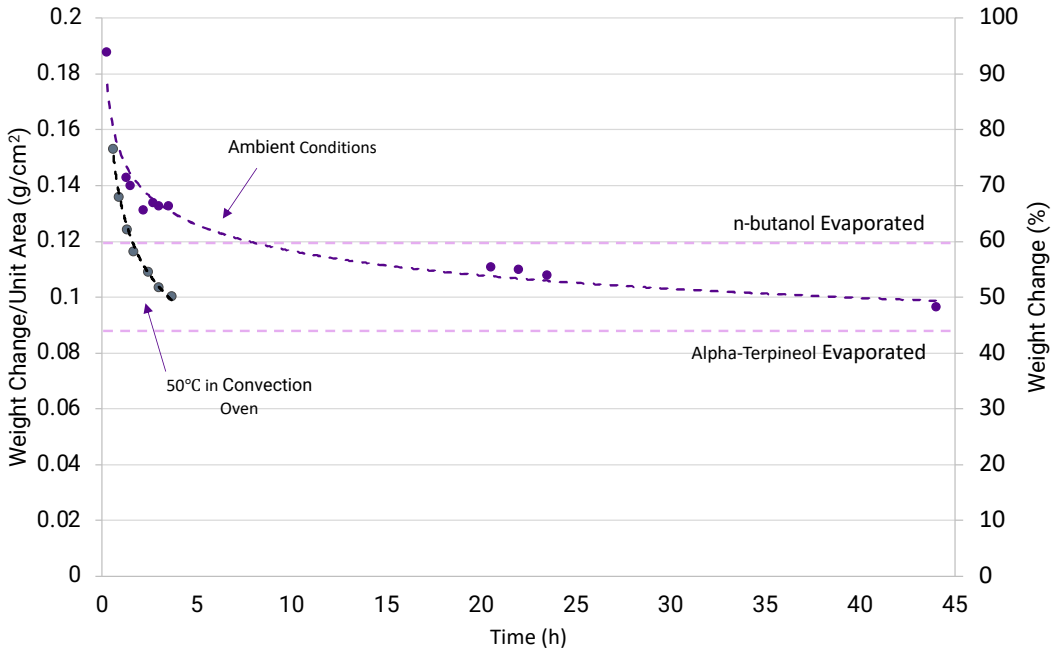

Figure 45: Time plot of weight change per unit area for LLZTO printed sample drying in ambient air conditions and 50°C in convection oven.

4.2.4 DIW Summary

In summary, the accuracy of DIW depends on many key factors including solid loading, rheology of the ink, printing speed, and drying mechanism. Ink printing was executed using the Nordson extrusion-based printing head with various nozzle size and geometry tips. The translation velocity in the Nordson program and applied pressure parameters were set after identifying optimal printing ranges through the DIW model study (Table 24). These parameters were suitable for a ink composition with a solid loading of 30-35 wt%, 0.35 wt% MFO dispersant (equivalent to 1 wt% concerning the solid loading), a 3:7 alpha-terpineol to n-butanol ratio, and a 1:1 binder-plasticizer ratio (both at 6.45 wt%).

Table 24: Printing parameters for the optimized LLZTO ink.

Nozzle Geometry	Nozzle Diameter	Translation Velocity	Pressure
Precision	250 µm	10 mm/s	3 bar
Tapered	250 µm	50 mm/s	2 bar
Precision	350 µm	20 mm/s	3.2 bar
Tapered	400 µm	60 mm/s	1 bar

4.3 Sintering of LLZTO Solid Electrolyte

In this section, the results for sintering phases 1 – 6 are described.

4.3.1 Sintering Phase 1: LLZTO Sintering with Mother Powder

The initial set of experiments involved the sintering of powder pressed LLZTO bulk pellets. This method was used to investigate the effects of sintering on bulk samples before evaluating printed SE. Table 25 outlines the bulk LLZTO pellet sintering conditions, phase results, and relative density. The sintering was performed in ambient atmosphere.

Table 25: Phase 1 - Bulk LLZTO pellet sintering conditions, phase results, and relative density.

	Sintering Conditions	Excess Li Source	Crucible	Results	Relative Density (%)
1	1200°C x 24h	Mother Powder	Alumina + lid	LZO	57.82
2	1200°C x 12h	Mother Powder	Alumina + lid	LZO	59.09
3	1200°C x 1h	Mother Powder	Alumina + lid	c- LLZTO + LZO	69.39
4	1250°C x 1h	Mother Powder	MgO + Lid	c- LLZTO + LZO	75.09
5	1230°C x 0.75h	Mother Powder	Alumina + lid	c- LLZTO + LZO	80.30
6	1320°C x 0.5h	-	Alumina + lid	c- LLZTO + LZO	93.15

It's notable that many pellets exhibited brittle behavior due to inadequate sinterability, leading to instances of cracking and adhesion to the alumina crucible (Figure A2). These observations confirm the presence of a liquid phase sintering resulting from reactions between alumina and LLZTO. The absence of a lid was also noted in the initial sintering runs indicating that without a cover, Li loss at elevated temperatures became more pronounced. As a result, using a lid or covering is necessary to create a Li-rich environment using the extra Li in the mother powder and to maintain equal heat distribution for the LLZTO pellets.

Furthermore, the reproducibility of phases during sintering emerged as a challenge due to the interplay of numerous uncontrollable and controllable factors. In numerous XRD analyses, the dominant peak consistently indicated the presence of pyrochlore $La_2Zr_2O_7$ (LZO), an intermediary compound formed during the heat treatment reactions. This LZO intermediate compound arises in scenarios of Li deficiency observed during high-temperature sintering. While functioning as an intermediate, it has been known to impede ionic conductivity as an impurity. Therefore, a dual focus must be maintained: minimizing the LZO phase while simultaneously preserving the crystalline LLZTO cubic phase.

Figure 46 shows the XRD results for six of the sintering experiments on LLZTO pellets (1-6) whilst being compared to reference, cubic LLZTO phase. The sintering temperature varied from 1200℃ to 1320℃ while dwelling time, and sintering setup were also varied (Table 25). Traditional dwelling time of 24 hours without a crucible lid and enough excess Li to compensate the Li loss showed complete degradation of LLZTO cubic phase with only signs of LZO remaining. When the dwelling time is reduced, reduced Li loss is observed with the presence of small peaks of cubic LLZO. However, a shorter dwelling time can indicate incomplete reactions displayed as double peaking (experiment #2). The most promising results with a minimal LZO peak and good cubic phase was seen in experiment #3, however, the relative density of the pellet was 75%. To ensure a good ionic conductivity is measured, the density of the desired LLZTO.

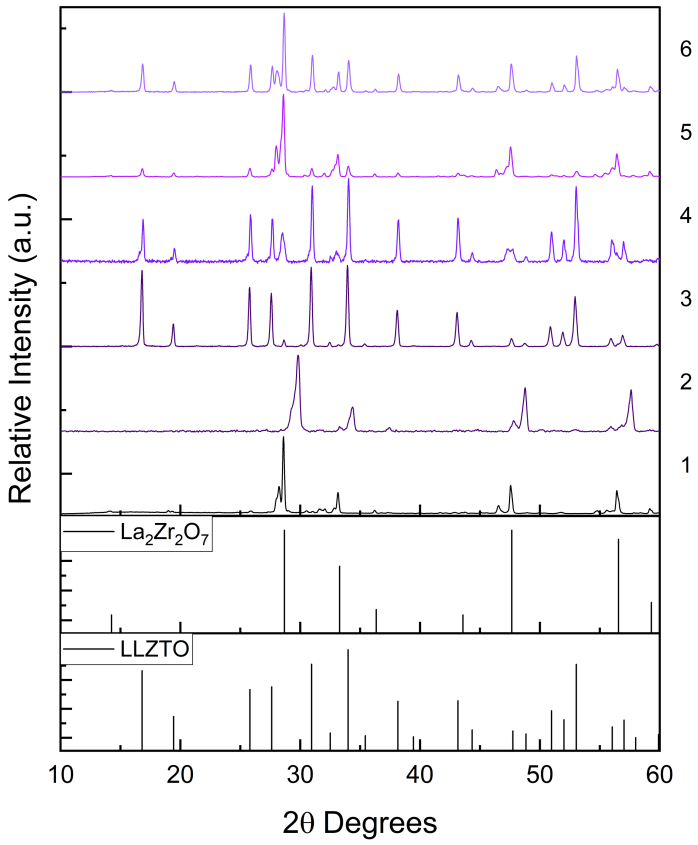

Figure 46: XRD analysis of LLZTO bulk pellets sintered at 1) 1200℃ for 24h, 2) 1200℃ for 12h, 3) 1200℃ for 1h, 4) 1250℃ for 1h, 5) 1230℃ for 0.75h, and 6) 1320℃ for 0.5h.

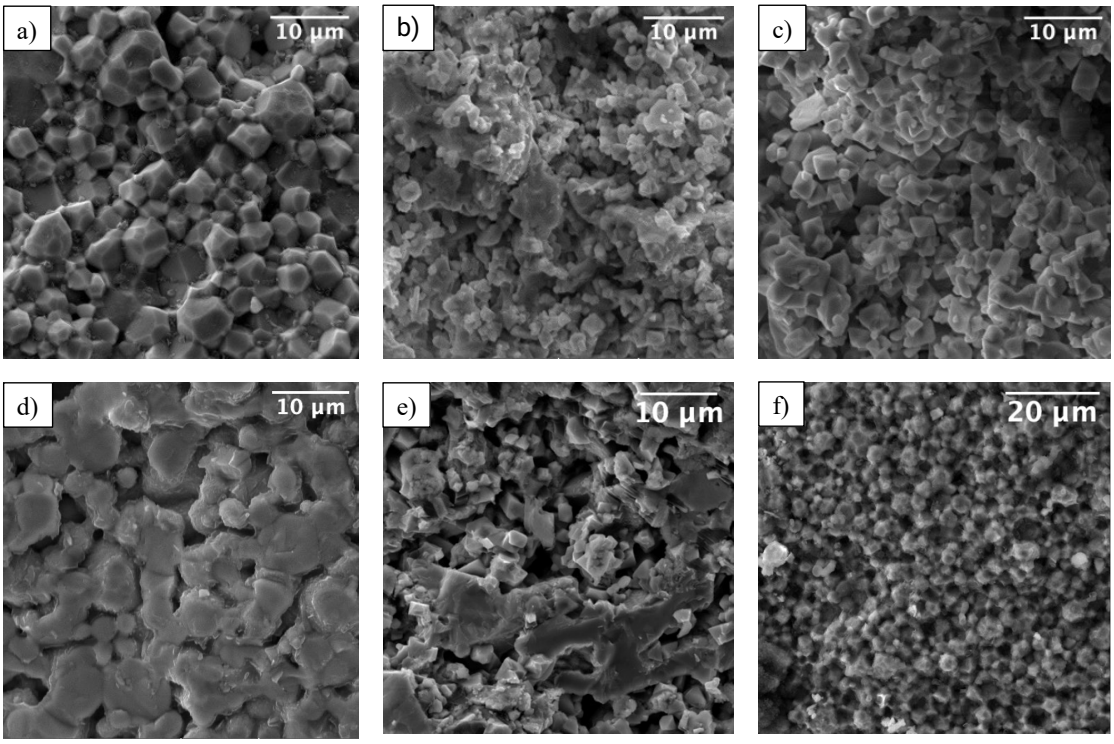

Figure 47: SEM fracture images of sintered LLZTO bulk pellets a) commercial pellet, b) 1200℃ for 24h, c) 1200℃ for 12h, d) 1250℃ for 1h, e) 1230℃ for 0.75h, and f) 1320℃ for 0.5h.

SEM images offer insight into the microstructural analysis of cross-sectional grain boundaries and pores. A comparison between the sintered LLZTO pellets and a commercially purchased pellet is depicted in Figure 47. In SE, uniform grains devoid of pores are essential for facilitating Li transport. Longer sintering times accompanied with Li deficit produced a porous microstructure, whereas higher temperatures with shorter durations resulted in a larger prevalence of well-defined grains. LLZTO pellet sintered at 1320℃ for 0.5h displayed uniforms grains like that of commercial pellet with approximately 93% relative high density.

To gain further insights into the phase transition of LLZTO during sintering, DSC was employed on commercial powder under a compressed air atmosphere (DSC/TGA Phase 1). This analysis aimed to examine the exothermic and endothermic reactions during sintering as illustrated in Figure 48. The first two observed endothermic peaks are attributed to moisture evaporation and LiOH decomposition. A 600℃, an exothermic peak indicates the formation of LZO impurity, accompanied by a total mass loss of 12.19%. Additionally, an endothermic decomposition of Li_2CO_3 is observed just below 700℃. The results of the DSC curves' results play a crucial role in analyzing and identifying the reactions occurring at critical

temperature during the sintering process such as the formation of LZO phase following the LiOH decomposition.

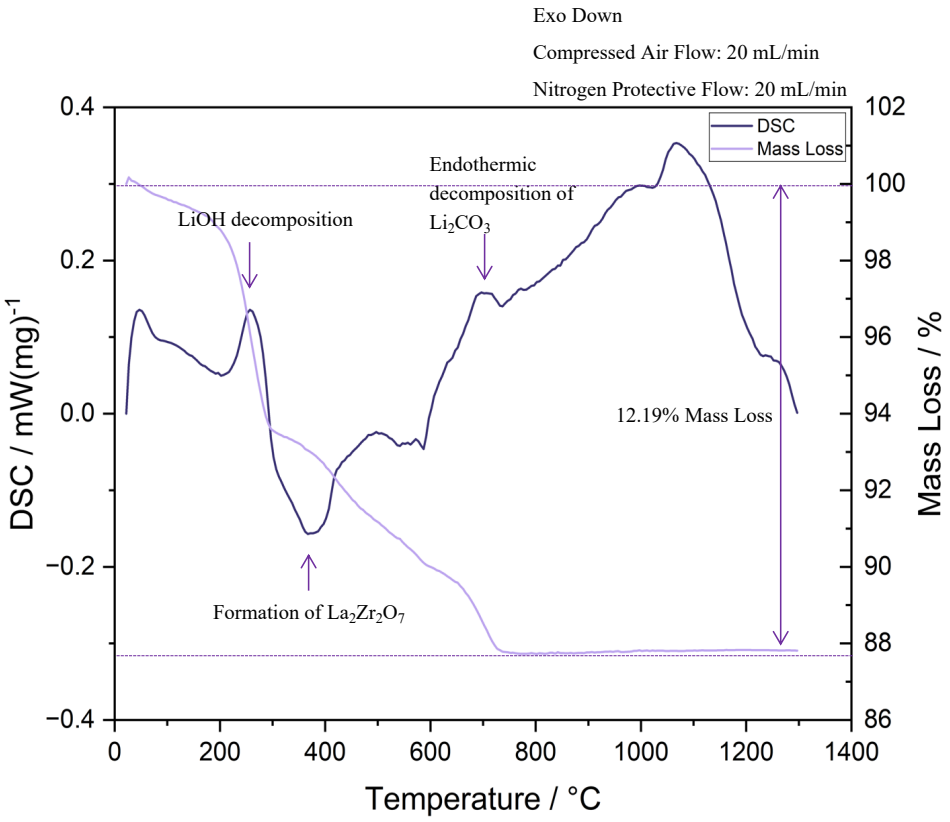

Figure 48: DSC plot of commercial LLZTO powder heated to 1300°C.

The first sintering test for thinner LLZTO SE involved treating a 300 µm thick LLZTO printed sample and film fabricated using a 200 µm threaded Mayer rod. Both samples were subjected to sintering using the same setup as employed for LLZTO pellets, in MgO crucibles as shown in Figure 34.

It was observed that de-binding of the PVB and BBP components was necessary to achieve a fully dense part and enhance its mechanical integrity. Given that the melting point of PVB and BBP is below 600°C, a de-binding process was implemented at 600°C for 3 hours, with a gradual heating rate to facilitate the evaporation of these components. Further refinement of this de-binding step is necessary to attain a highly dense ceramic.

A challenge encountered during the sintering process was the warping of the ceramic. As the ceramic piece is subjected to high temperatures, the binder, plasticizer, and residual solvents began to evaporate from the edges, resulting in uneven stresses and the formation of cracks. To mitigate this issue, sandwiching the ceramic part between plates to keep it flat is proposed to promote more uniform sintering.

Furthermore, the attempt to use excess mother powder as a source of additional Li to compensate for Li loss was found to be unviable. This was due mother powder adhering to the LLZTO component and concerns about the appropriate quantity of excess Li. While thinner samples have a higher surface area-to-volume ratio, the need to compensate Li loss becomes more significant. XRD analysis revealed a notable degradation of the cubic LLZTO phase in both scenarios, leaving only the LZO impurity phase intact (Figure 49). This indicates the necessity for additional research on Li loss in the sintering process of LLZO. The possibility of introducing excess Li by adding it within the green body or within the crucible is considered.

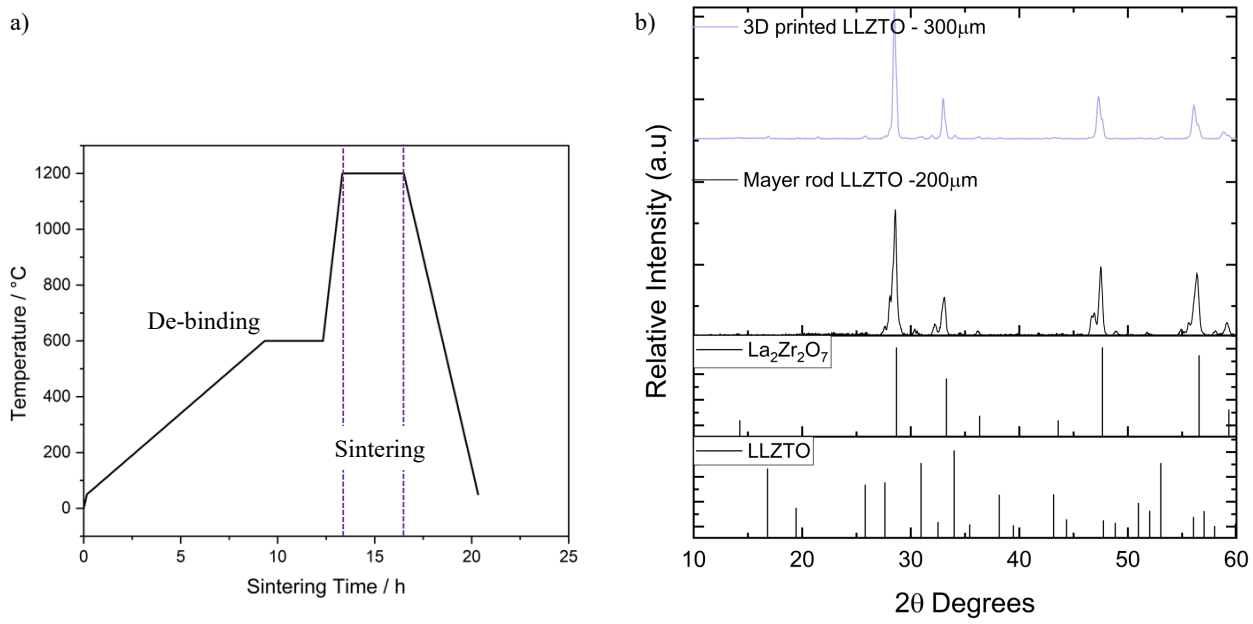

Figure 49: a) Sintering profile of LLZTO and b) XRD of 300 µm 3D printed LLZTO and casted 200 µm LLZTO film in MgO crucible sintered in ambient air with mother powder.

4.3.2 Sintering Phase 2: LLZTO Sintering with Excess LiOH within Ink in Ambient Air Conditions

The LLZO mother powder was found to be an insufficient source of Li during the sintering of casted SE. Consequently, alternative methods for ensuring an adequate Li compensation were explored. The first approach chosen to investigate this was the addition of excess LiOH (5, 10, and 20 wt%) to the ink.

As indicated by the XRD results in Figure 50b, it was evident the quantity of excess Li did not contribute to the stabilization of the cubic phase, suggesting that excess Li alone is not the sole factor influencing phase stability. Other factors, such as the environment and sintering setup, exert significant influence on the phase.

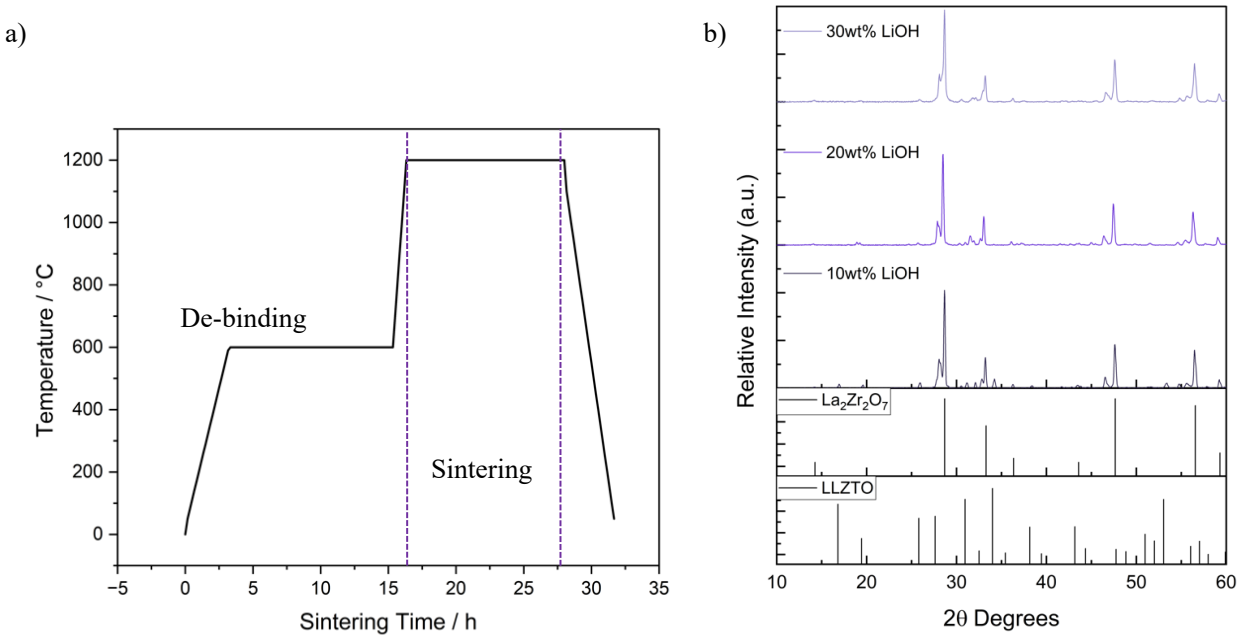

Figure 50: a) Sintering profile of LLZTO and b) XRD LLZTO with 10, 20, and 30 wt% excess LiOH in ink sintered in ambient air

4.3.3 Sintering Phase 3: Exploring Sintering Time

In addition to addressing Li compensation, the sintering atmosphere also plays a pivotal role in achieving a dense ceramic electrolyte with a cubic phase. As previously mentioned, the use of an inert gas atmosphere can effectively reduce reactivity with CO_2 and promote the stabilizing of the cubic phase. Consequently, a

high-purity argon gas flow was selected to sinter two ceramic components under different sintering conditions, labeled as Condition A and Condition B. Condition A entailed a de-binding process at 700°C for 4 hours, followed by sintering at 1200°C for 1.5 hours. On the other hand, Condition B involved de-binding at 600°C for 12 hours, followed by sintering at 1200°C for 12 hours.

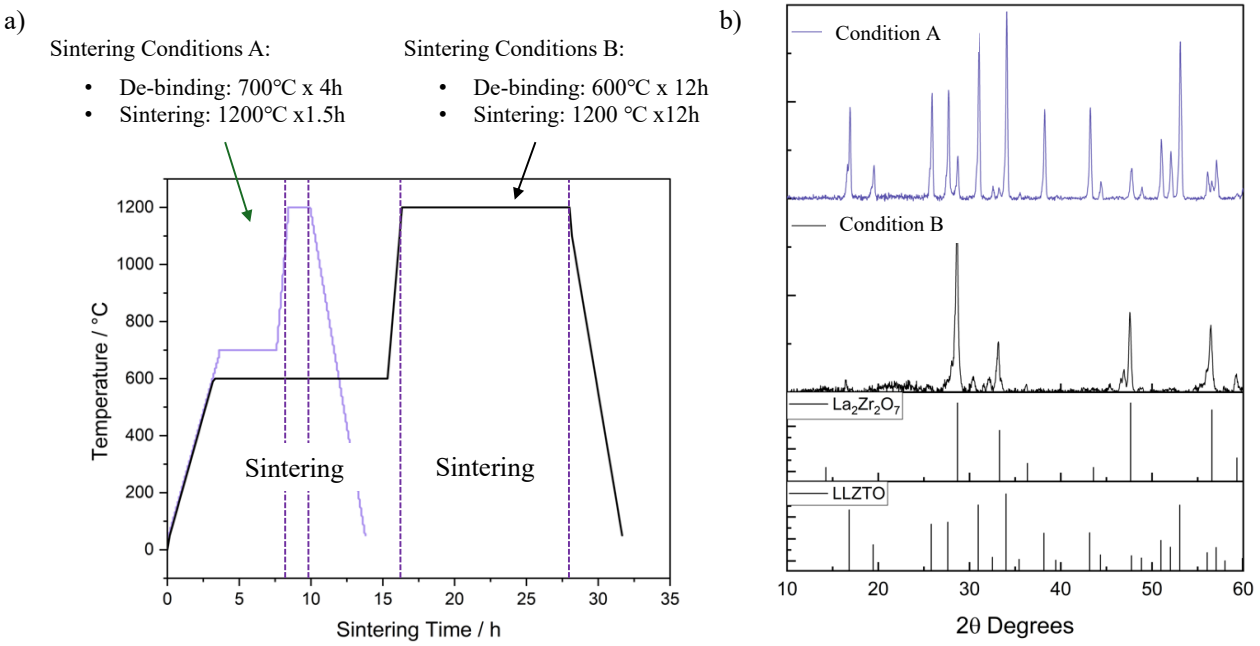

Figure 51: a) LLZTO sintering profile A and B and b) XRD of LLZTO sintering conditions with 5 wt% excess LiOH in ink in argon atmosphere.

The XRD findings, comparing the two sintering conditions, reveal that sintering Condition A led to a more pronounced cubic phase (Figure 51) for the casted SE with 5 wt% excess LiOH. Conversely, sintering Condition B resulted in the presence of a purely LZO impurity phase. These results affirm that having flowing argon gas during sintering is effective in stabilizing the cubic phase for 3D printed ceramic electrolytes, provided that the sintering duration is reduced. Reducing the sintering time at elevated temperatures diminishes Li loss, ultimately yielding a phase composition that is desirable with minimal impurities.

4.3.4 Sintering Phase 4: LLZTO Sintering with Excess LiOH within Ink in Argon

To further investigate these effects, cased LLZTO ceramic electrolytes were sintered with varying amounts of excess Li in the ink, specifically 0, 5, 10, and 20 wt%, while maintaining the de-binding and sintering conditions as outlined in Table 26. The XRD results indicate that even a small amount of excess Li can facilitate the transition from the intermediate LZO phase to the cubic LLZO phase (Figure 52). The R value, which represents the intensity of the LZO peak relative to the highest intensity of the cubic LLZTO peak as percentage, is a crucial parameter. A smaller R value is preferred, signifying a lower presence of LZO impurities. The calculated R values for 0, 5, 10, and 20 wt% excess Li are 553, 2.52, 81.15, and 8.40%, respectively. In theory, with the addition of excess Li leads to a reduced in R values. However, it's important to acknowledge that other factors, such as the setup and argon flow rate, can influence the phase composition.

The SEM analysis provides insights into the grain size generated during the sintering process. A well-sintered component exhibits minimal pores and polyhedral grains when the cross-section is examined. The SEM cross-section analysis reveals a trend, suggesting that excess Li can also serve as a sintering aid decreasing porosity in the sintered part. It is noted the film sintered with 10 wt% excess LiOH in ink exhibited more grain growth compared to other 5 and 20 wt% LiOH inks. This can be attributed to temperature, placement of plates within furnace, and other environmental parameters. Due to issues with reproducibility and poorly controlled atmosphere, it cannot be stated with certainty the cause of this grain growth.

Table 26: Phase 4 - Sintering conditions, phase results, and relative density for casted LLZTO films – 0, 5, 10, 20 wt% excess LiOH within the ink and argon atmosphere.

	De-binding Conditions	Sintering Conditions	Excess LiOH in Ink	Results	R Value (I_{LZO}/I_{LLZTO})
1	2°C/min to 700°C	1200°C x 1.5h	0 wt%	LZO	553
2	2°C/min to 700°C	1200°C x 1.5h	5 wt%	c- LLZTO + LZO	2.52
3	2°C/min to 700°C	1200°C x 1.5h	10 wt%	c- LLZTO + LZO	81.15
4	2°C/min to 700°C	1200°C x 1.5h	20 wt%	c- LLZTO + LZO	8.40

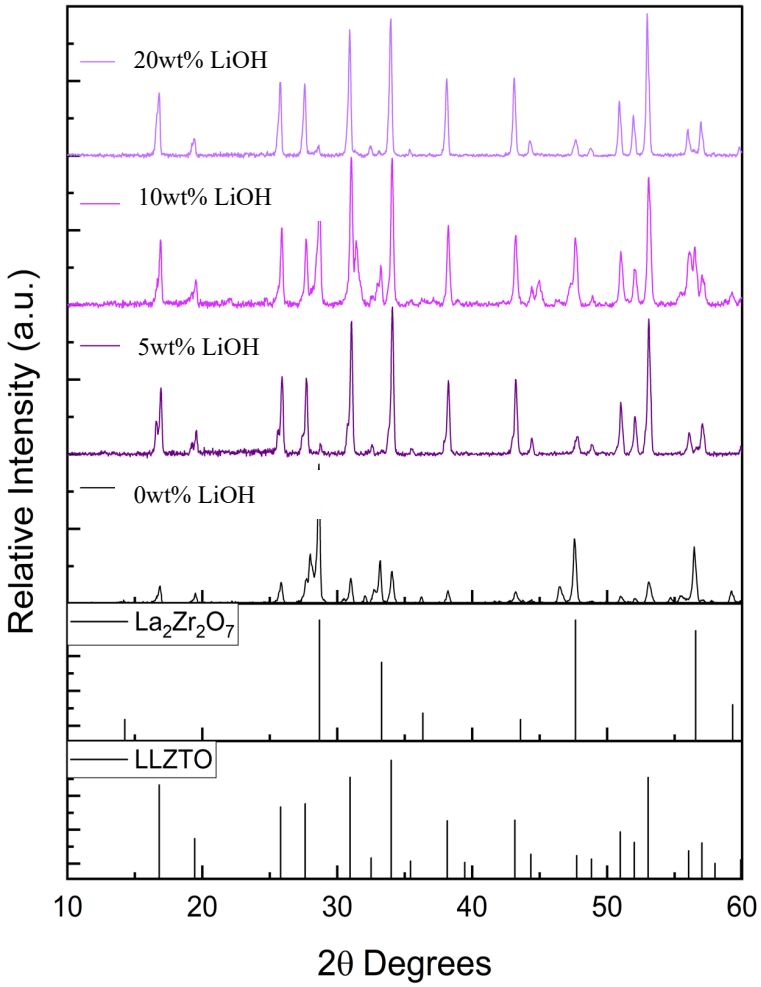

Figure 52: XRD of casted LLZTO films sintered with 0, 5, 10, 20 wt% excess LiOH in ink at 1200°C for 1.5h in argon atmosphere.

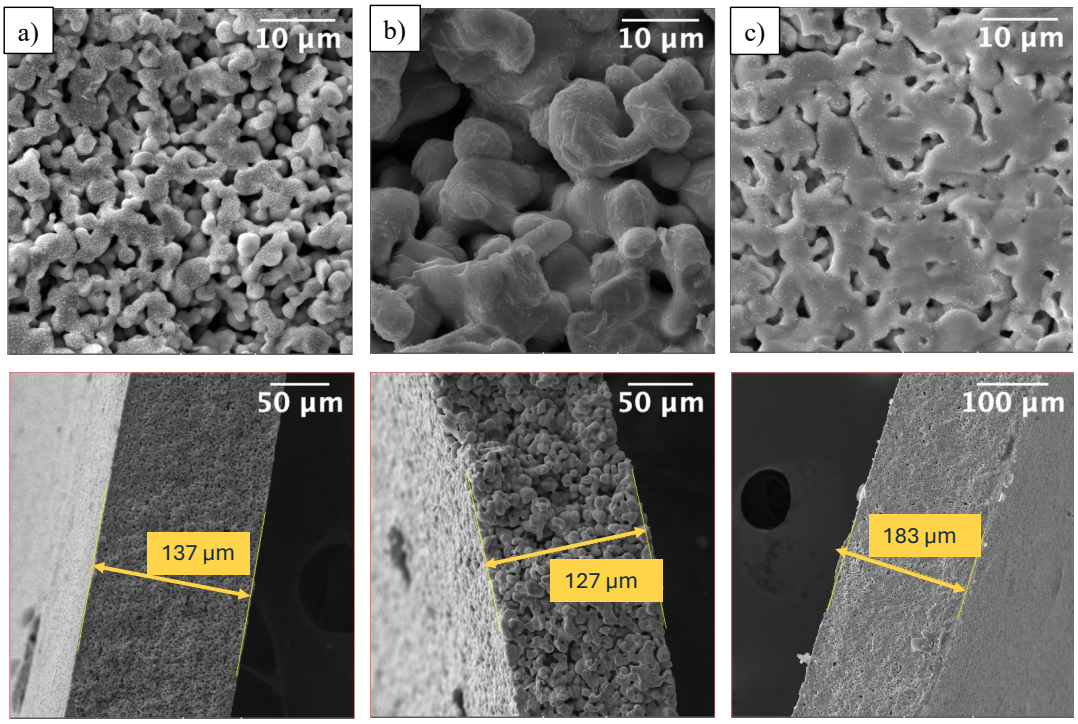

Figure 53: SEM fracture images of casted LLZTO films sintered with a) 5 wt%, b) 10 wt%, and c) 20 wt% excess LiOH in ink at 1200°C for 1.5h and argon atmosphere.

4.3.5 Sintering Phase 5: LLZTO Sintering with Excess LiOH in Crucible in Argon

Similar to introducing excess LiOH within the ink, a similar experiment design was conducted to evaluate the effect of LiOH on the phase of LLZTO. The quantity of LiOH was measured based on the weight of the printed SE and strategically placed along the edges of the MgO crucible. The sealed MgO crucible plays a role in creating a Li_2O atmosphere when the LiOH melts, thus facilitating the transformation of intermediate phases into the cubic LLZTO phase.

Table 27: Phase 5 - Sintering conditions, phase results, and relative density for printed LLZTO SE – 0, 10, 20, 30 wt% excess LiOH in crucible and argon atmosphere.

	De-binding Conditions	Sintering Conditions	Excess LiOH in Crucible	Results	R Value (I_{LZO}/I_{LLZTO})
1	2°C/min to 700°C	1200°C x 1.5h	0 wt%	LZO	439
2	2°C/min to 700°C	1200°C x 1.5h	10 wt%	c- LLZTO + LZO	30.76
3	2°C/min to 700°C	1200°C x 1.5h	20 wt%	c- LLZTO + LZO	6.42
4	2°C/min to 700°C	1200°C x 1.5h	30 wt%	c- LLZTO + LZO	22.59

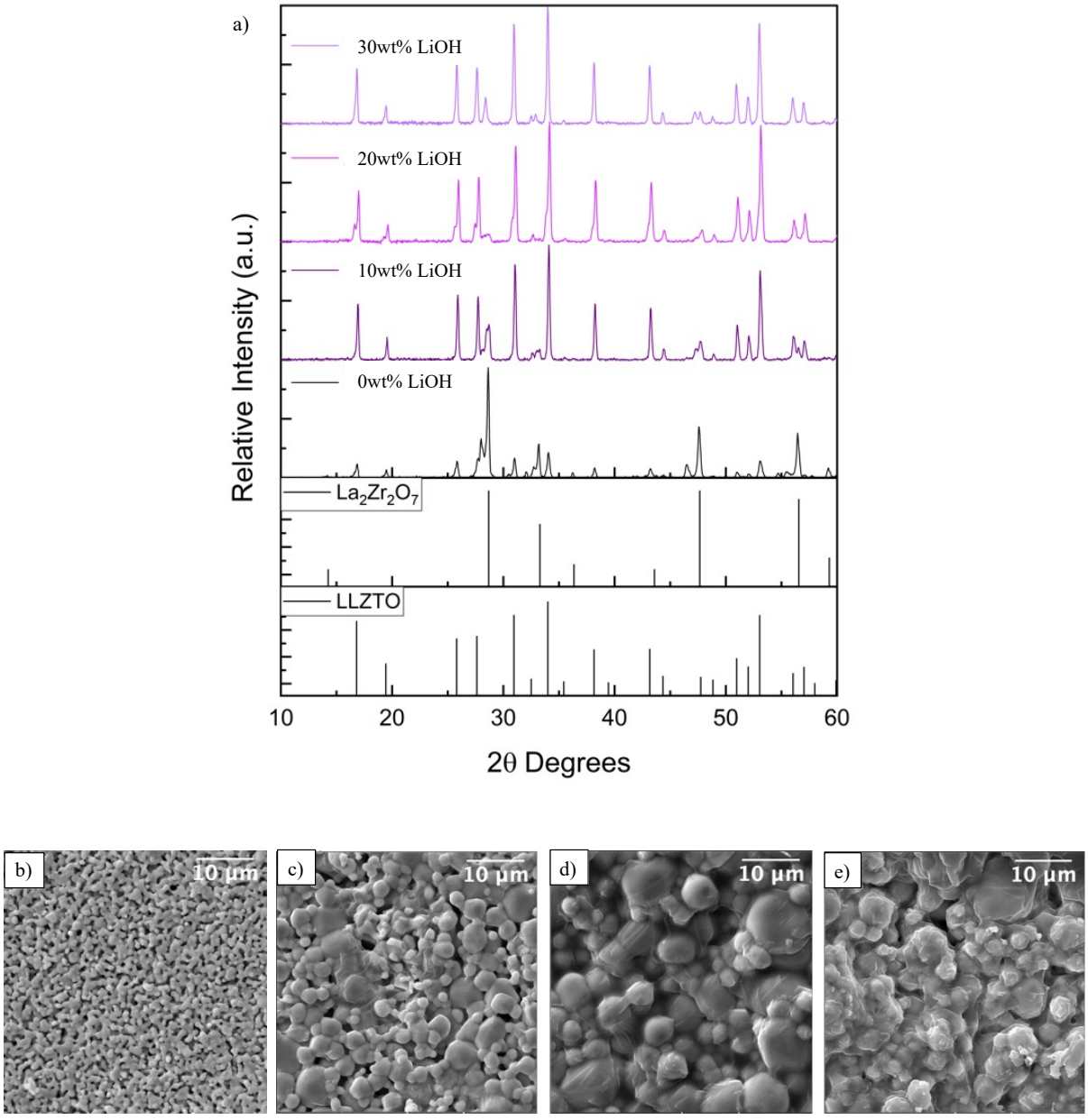

Figure 54: a) XRD of printed LLZTO SE sintered with 0, 10, 20, 30 wt% excess LiOH in MgO crucible and argon atmosphere; SEM images of top view of b) 0 wt%, c) 10 wt%, d) 20 wt%, and e) 30 wt% excess LiOH in MgO crucible.

The XRD analysis results shown in Figure 54a, as indicated by the R value, demonstrate that the addition of 20 wt% excess LiOH in this manner resulted in maintaining the cubic LLZTO phase with a reduced impurity phase, approximately 6.42%. The SEM analysis revealed a densely sintered pellet when viewed from the top, with grain sizes ranging from approximately 4 to 10 µm and minimal pore formation (Figure 54b-e). These results lead to the conclusion that introducing an excess Li source into the crucible is a straightforward and effective method for compensating for Li loss. However, it's important to note that challenges related to the reproducibility of phases, the removal of the SE from the MgO crucible without cracking or adhesion, and improving density still need to be addressed.

4.3.6 Optimizing De-binding using Thermal Gravimetric Analysis

Up to this point, the temperature and duration of both the de-binding and sintering steps are held constant to better understand the relationship between Li compensation and phase analysis. However, it is evident from the literature review that the temperature and duration of de-binding and sintering have significant effects.

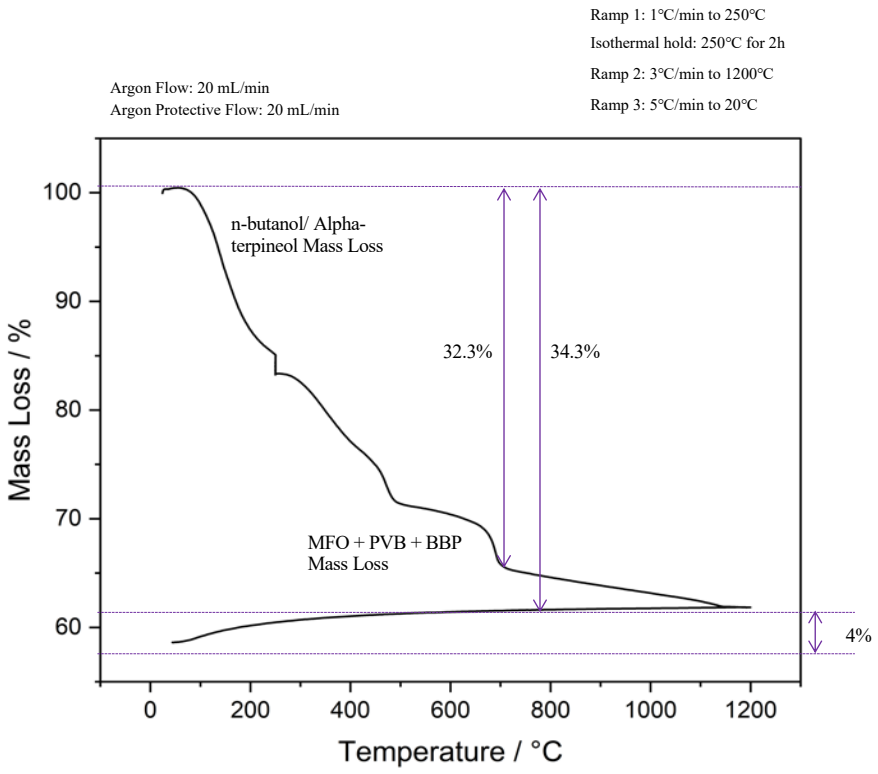

Figure 55: TGA plot of LLZTO solid electrolyte heated to 1200°C.

To address this, a TGA curve can be employed to assess the mass loss that occurs during the heating profile, as depicted in Figure 55 and Figure 56 (DSC/TGA Phase 2). Two TGA curves were conducted to determine the appropriate de-binding temperature and duration. This stage is crucial in establishing an effective de-binding cycle before exploring sintering parameters.

Figure 55 displays the plot of mass loss (%) vs. temperature, illustrating the heating of the SE to 1200°C without any additional isothermal heating time for de-binding. The plot reveals an approximate 34% mass loss by 750°C. This mass loss is the solvents and dispersants evaporating, while approximately 30% can be attributed to the burnout of the binder and plasticizer. This plot indicates the ideal temperature for de-binding PVB and BBP falls within the range of 700-750°C.

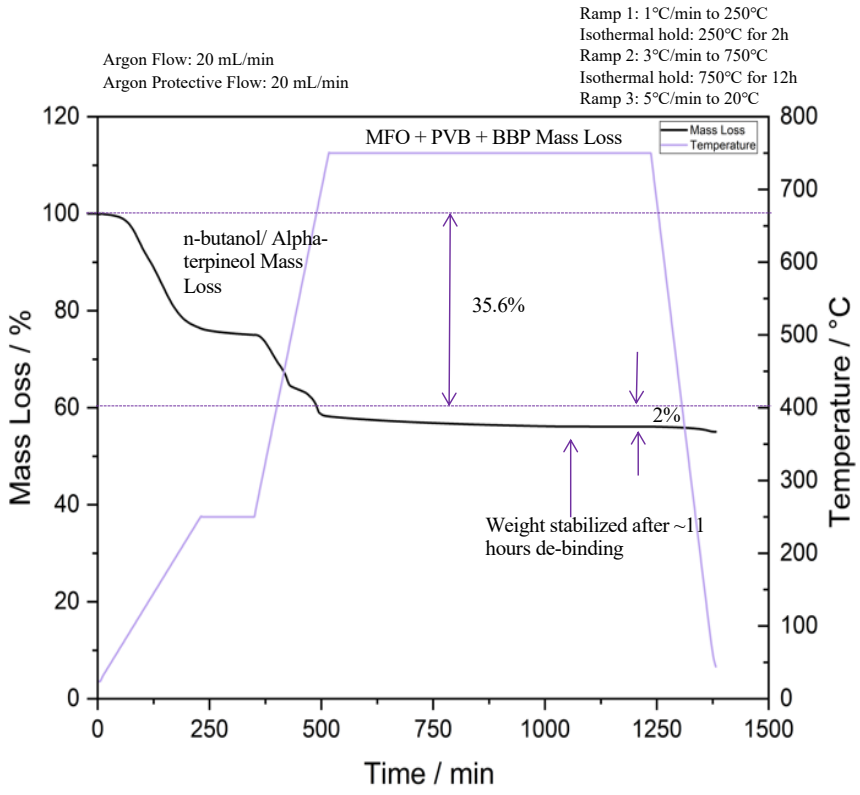

Figure 56: TGA plot of LLZTO solid electrolyte heated to 750°C for 12h.

In Figure 56, the TGA curve depicts the de-binding process with an isothermal hold at 750°C over a duration of 12 hours. Once again, an initial weight loss of approximately 35% is observed before the isothermal heating at 750°C commences. An additional 2% mass loss is noted before the weight stabilizes,

which occurs after approximately 11 hours. This analysis confirms an isothermal hold for12 hours within the temperature range of 700-750°C is necessary to ensure the complete PVB and BBP burnout from the sample before advancing to the subsequent sintering step.

4.3.7 Sintering Phase 6: Optimizing Sintering of Printed LLZTO Solid Electrolyte

Although sintering remains a formidable challenge for LLZTO ceramic electrolytes, several additional steps can be incorporated into the standard operating procedure (SOP) to enhance sinterability. Up to this point, efforts are made to address the issues related to excess Li, sintering environment, and de-binding parameters. The addition of 5-20 wt% excess Li has proven effective in maintaining the cubic phase at elevated temperatures of 1200°C with a high purity flowing argon atmosphere. Nonetheless, challenges persist, particularly concerning the adhesion of the ceramic electrolyte to the MgO plate and the density of the electrolyte.

Numerous research groups have employed graphite films to sandwich the LLZTO SE films [95,118,149]. Graphite is preferred as it does not react with LLZTO, and the pressed film between plates helps keep the electrolyte flat, preventing warping along the edges. However, the proposed setup involves a unique approach, where the sandwiched LLZTO and excess Li is placed directly inside the crucible, with a lid, creating a freestanding configuration. This innovative setup offers several advantages, including ensuring the LLZTO remains flat, being sandwiched between graphite to prevent adhesion to MgO plates, and establishing a Li-rich environment required to maintain the cubic phase. A comprehensive schematic of this newly proposed setup is presented in Figure 38.

Moreover, printed LLZTO pellets are gently heated on a hot-plate to activate the binders, and then they are subjected to compression at a pressure of at 3.8 Ton weight using weighing paper and 30 mm die pressing blocks. This step ensures the ceramic particles are tightly packed together before the sintering process. Subsequently, the compressed thin pellets can be cut to the desired size, typically 1/2 inch, using a metal puncher. This cutting process focuses on removing thinner edges that could warp during sintering, further contributing to the achievement of a flat and dense solid ceramic electrolyte. This process is depicted in Figure 37.

The sintering temperature is known to be a significant factor in the formation of larger polyhedral grains, which are ideal for ionic transport and achieving higher density. Therefore, printed and cut LLZTO pellets were subjected to sintering at three different temperatures: 1000°C, 1100°C, and 1200°C for a duration of 1.5 hours, without the use of excess Li. The naming convention used is G-1100Cx1.5h-0EL, G-

1100Cx1.5h-0EL, and G-1200Cx1.5h-0EL where 'G' represents using a graphite sheet, and 'EL' represents the excess LiOH. The results indicated a greater Li deficiency is observed at the higher temperature of 1200°C in comparison to 1000°C and 1100°C (Figure 57a and Table 28). Although impurity levels remain relatively low compared to previous results, these findings underscore the advantages of the new set-up within the box furnace. The relative densities for these thinner pellets are recorded as 62%, 85%, and 93% (Figure 57b), accompanied by R values of 1.7%, 3.14%, and 11.45% for LZO impurity, respectively.

Table 28: Phase 6 – Sintering conditions, phase results, and relative density for printed LLZTO pellets sintered with new sintering set-up – No excess LiOH in crucible in argon atmosphere.

	De-binding Conditions	Sintering Conditions	Excess LiOH in Crucible	Results	R Value (I_{LZO}/I_{LLZTO})	Relative Density (%)
1	700°C x12h	1000°C x 1.5h	0 wt%	c- LLZTO	1.70	61.64
2	700°C x12h	1100°C x 1.5h	0 wt%	c- LLZTO	3.14	85.09
3	700°C x12h	1200°C x 1.5h	0 wt%	c- LLZTO + LZO	11.46	92.72

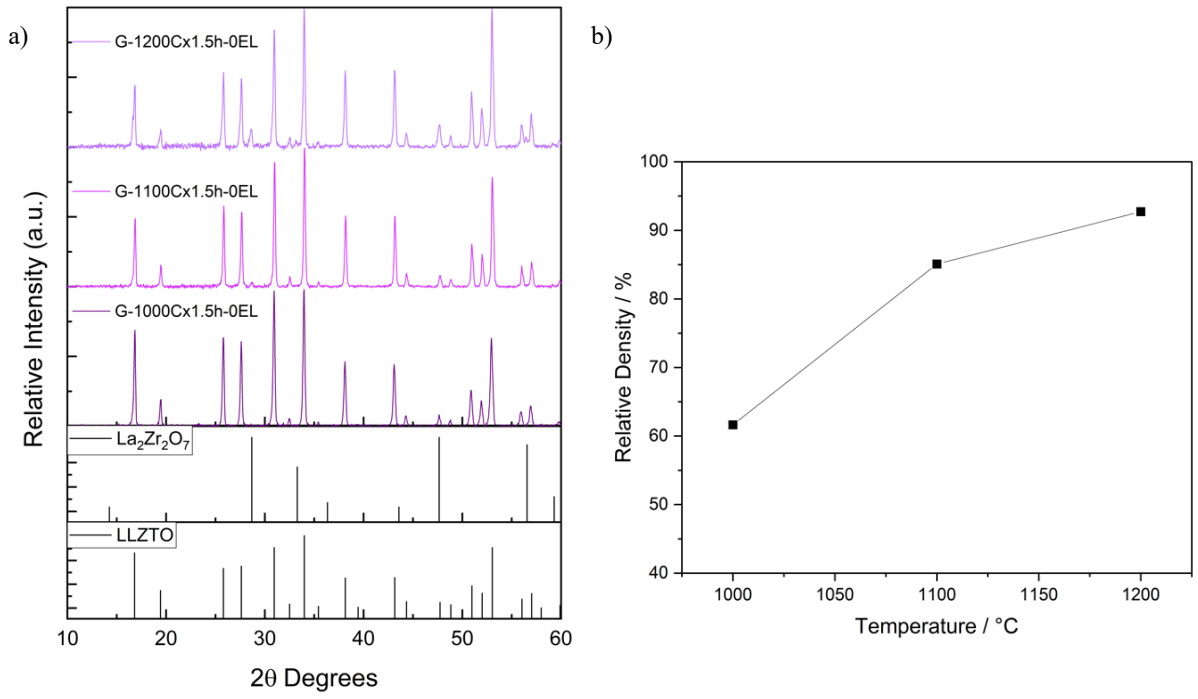

Figure 57: a) XRD of printed LLZTO pellet sintered with new sintering set-up - no excess LiOH and argon atmosphere; b) relative density plot relating temperature to density of SE.

The positive outcomes of the previous DOE have encouraged the exploration of extended sintering durations, specifically 1.5 hours and 6 hours, at temperatures of 1100°C and 1250°C. This study involved varying the presence of excess Li in the crucible, with concentrations of 0 and 10 wt%. The results are presented in Table 29, Figure 58, and Figure 59.

Table 29: Sintering conditions, phase results, and relative density for printed LLZTO pellets sintered with new sintering set-up – 0, 10 wt% excess LiOH sintered at 1100℃ and 1250℃ in argon atmosphere.

	De-binding Conditions	Sintering Conditions	Excess LiOH in Crucible	Results	R Value (I_{LZO}/I_{LLZTO})	Relative Density (%)
1	700°C x12h	1100°C x 1.5h	0 wt%	c- LLZTO	2.82	85.09
2	700°C x12h	1100°C x 6h	0 wt%	c- LLZTO + LZO	10.41	83.91
3	700°C x12h	1100°C x 1.5h	10 wt%	c- LLZTO	1.85	95.45
4	700°C x12h	1100°C x 6h	10wt%	c- LLZTO	1.92	85.73
5	700°C x12h	1250°C x 1.5h	0 wt%	c- LLZTO + LZO	44.67	-
6	700°C x12h	1250°C x 6h	0 wt%	c- LLZTO	119.81	88.09
7	700°C x12h	1250°C x 1.5h	10 wt%	c- LLZTO	35.07	93.64
8	700°C x12h	1250°C x 6h	10 wt%	c- LLZTO	507.83	83.82

The most favorable results were achieved when sintering at 1100°C for 1.5 hours with 10wt% excess LiOH, yielding the lowest observed impurity at 1.85% and a relative density of 95%. However, as the temperature and annealing duration are increased, there is a noticeable rise in LZO impurity and a degradation of the cubic LLZTO phase. During the sintering process, the pellets experienced a lateral shrinkage of approximately 34% in each run and a thickness reduction of 43%. Polyhedral grains were observed, characterized by minimal pore formation, which is comparable to commercial LLZTO pellet.

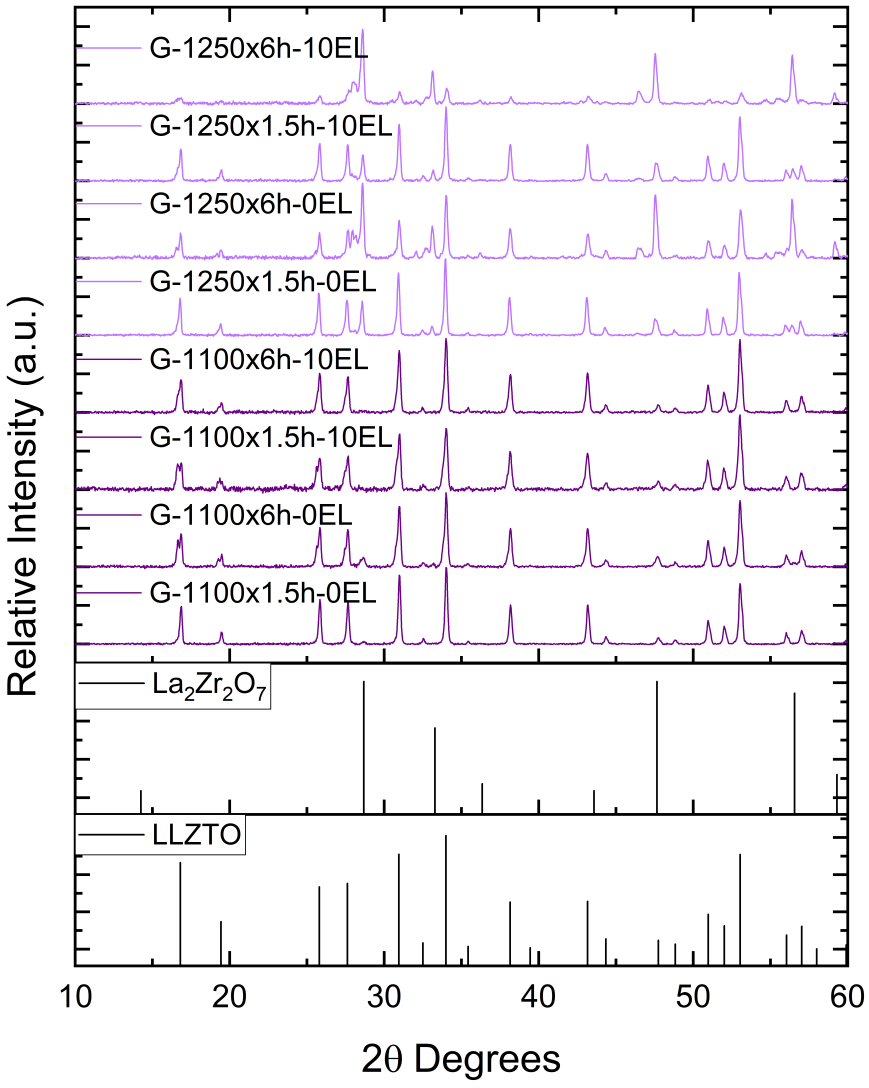

Figure 58: XRD of printed LLZTO sintered with new sintering set-up - 0, 10 wt% excess LiOH sintered at 1100°C and 1250°C for 1.5h and 6h in argon atmosphere.

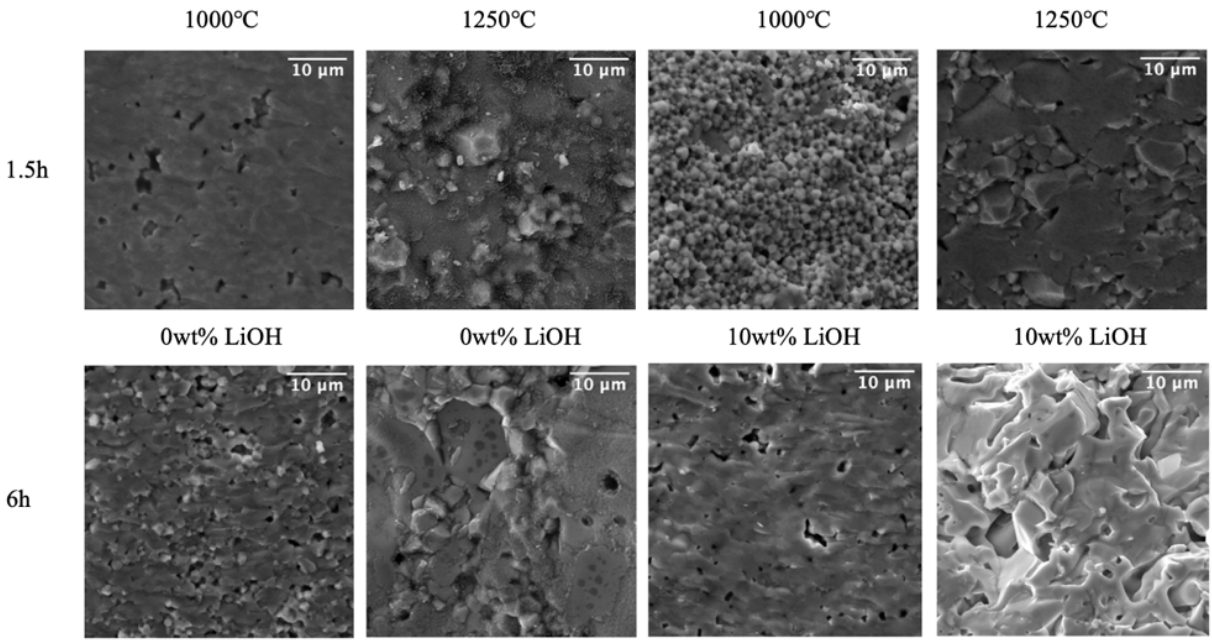

Figure 59: SEM fracture images printed LLZTO pellets sintered with new sintering set-up - 0, 10 wt% excess LiOH sintered at 1100°C and 1250°C for 1.5h and 6h in argon atmosphere.

In summary, the optimal conditions for achieving a flat, dense, and cubic-phased pellet with a thickness of 201 µm were established at 1100°C for 1.5 hours after a de-binding step at 700°C for 12 hours in a flowing Ar gas environment, employing 10 wt% excess LiOH, and using the novel sintering setup.

These results are comparable to what is seen in literature for sintering the films of a similar thickness range. Table 13 compares many thinner LLZO ceramic film de-binding and sintering parameters. It can be inferred that a small amount of excess Li is often required to compensate for the Li loss. Parejiya et al. demonstrated tape-casting of Al-LLZO films with a 200 µm thickness, using PVB binder and BBP plasticizer in the ink formulation [95]. The de-binding temperature used in the paper is lower (600°C) than the one we employed (700°C) for the same duration of 12 hours. The purpose of the de-binding step is to ensure all binder and plasticizer is burned off the green body before undergoing high-temperature sintering. Considering the boiling point of PVB and BBP is 660°C and 370°C, a 700°C de-binding temperature can ensure successful burnout of binder and plasticizer. This was confirmed with the TGA results shown in Figure 55. It is noteworthy, the amount of binder and plasticizer used in this research to facilitate DIW, drying without cracking, and successfully remove green body off PET substrate, is greater than reported in the literature [95]. Therefore, the higher temperature can increase the rate of PVB/BBP burnout ensuring

the 12 hours is sufficient time duration for this process as seen in Figure 56. Additionally, a sintering temperature of 1100℃ is employed in this research comparable to the literature review [96,119,143].

4.3.8 Correlation of Thickness to the Cubic Phase

One of the significant advantages of 3D printing is its capability to produce thin SE in various shapes. Typically, bulk pellets need to be relatively thick, usually > 5 mm, to achieve a dense pellet with a cubic phase. Sintering thinner films, with a thickness in the range of a few hundred microns, poses a more complex challenge. This is because the higher surface area-to-volume ratio in thinner pellets has a significant impact on the phase during the sintering process. As a result, a thinner green thickness SE requires more excess LiOH to compensate the Li loss compared to a thicker SE. This is demonstrated in the XRD results of sintered LLZTO with green thicknesses of 434, 357, 278, and 195 µm (Figure 60 and Figure 61b).

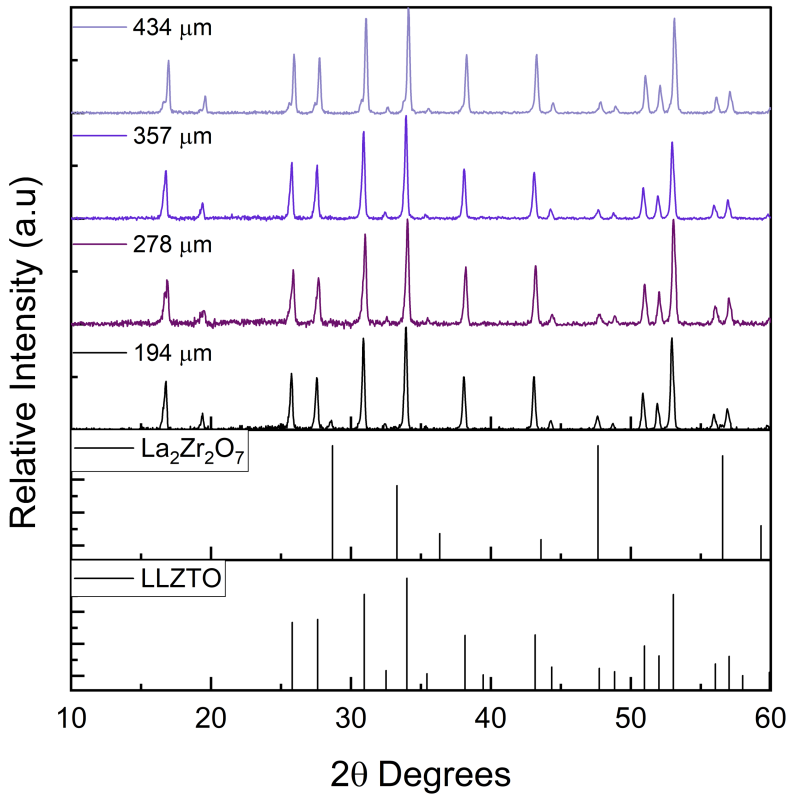

Figure 60: XRD of printed LLZTO pellets sintered with new sintering set-up – 10 wt% excess LiOH in crucible sintered at 1100℃ for 1.5h in argon atmosphere.

The thinner SE sintered at 1100°C for 1.5h with 10 wt% excess LiOH show more LZO impurity in the crystal phase. Interestingly, it has been discovered that samples with a green thickness exceeding 400 µm can attain a cubic phase without the need for excess Li when sintered at 1100°C for 1.5 hours. However, for ceramics with a green thickness of approximately less than 200 µm, as much as 20 wt% excess LiOH is required (Figure 61a).

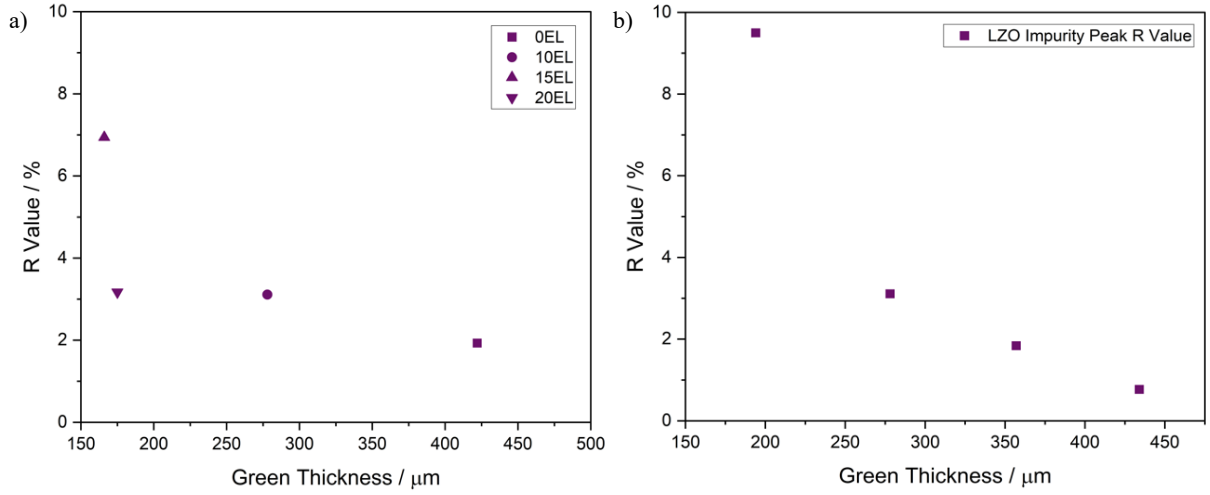

Figure 61: a) Excess LiOH (xEL wt%) compensation for Li loss at 1100°C for 1.5h to achieve minimal LZO impurity with varying green thicknesses SE and b) the effect of green thickness on LZO impurity peak R value sintered at 1100 °C for 1.5h with 10 wt% excess LiOH.

Additionally, with the aid of SEM images in Figure 62, it can be observed the addition of Li acts as a sintering aid to further densify the thinner solid ceramic electrolytes. This finding is unique in the context of LLZTO sintering and can provide the basis to conduct further research in this area. To our knowledge, there are no prior articles in the literature that have explored the correlation between excess Li and the cubic phase in the same manner.

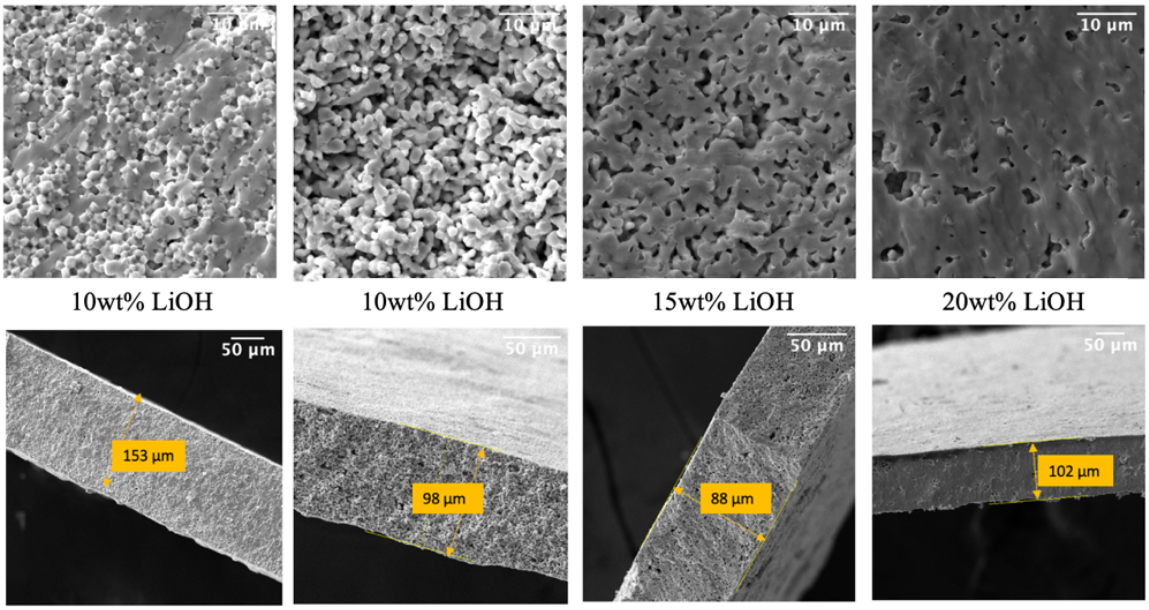

Figure 62: SEM fracture images of printed LLZTO pellets sintered with new sintering set-up – 10, 15, and 20 wt% Excess LiOH in MgO sintered at 1100℃ for 1.5h in argon atmosphere.

4.3.9 Sintering Summary

In summary, multiple optimization efforts were conducted to successfully prepare a high-density, cubic-phase LLZTO SE. Sintering experiments were performed on bulk LLZTO pellets casted films, and 3D printed pellets to gain insights into the sintering behavior of ceramic electrolytes. The optimized sintering parameters are 1100℃ for 1.5 hour with 10 wt% excess LiOH after de-binding at 700℃ for 12 hours. Additionally, it is evident that thinner SE require a lower sintering temperature and a higher excess of Li to achieve a dense, cubic phase electrolyte.

Moreover, a novel sintering setup was developed to create a Li-rich environment conducive to sintering 3D printed LLZTO pellets. This setup involves sandwiching the SE between graphite sheets and MgO plates. The graphite sheets play a crucial role in preventing the SE from adhering to MgO or alumina plates. The de-binding and sintering procedure should take place in flowing high-purity argon environment to preserve the crystal phase. The challenges initially outlined in section 2.4, such as insufficient sintering capabilities, sintering conditions and set-ups, H_2O/CO_2 reactivity, and composition and microstructure, are addressed in the optimized sintering setup achieving a SE with cubic crystal phase with 95% relative density.

4.4 Electrochemical Performance of LLZTO Solid Electrolyte

Thus far, numerous attempts were made to sinter a successful working dense, and cubic phased LLZTO ceramic electrolyte. A 200 µm LLZTO ceramic electrolyte was sintered with 95% relative density and purely cubic phase as shown in Figure 63 sintered at 1100℃ for 1.5h with 10 wt% excess LiOH.

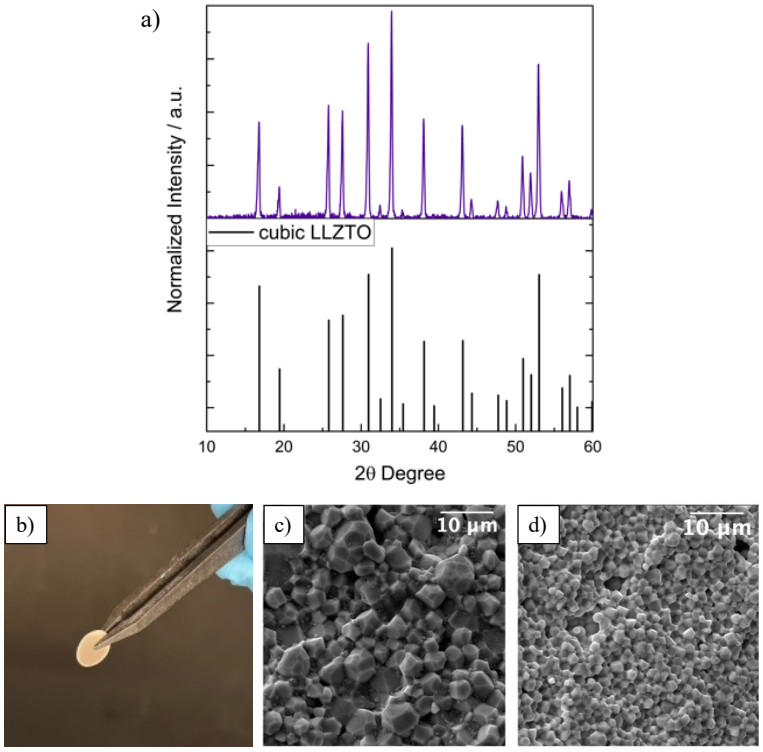

Figure 63: a) XRD of sintered LLZTO, b) optical image of SE, and SEM imaging of c) commercial pellet compared with d) 217 µm 3D-printed pellet.

The dense LLZTO SE was tested using the EIS set-up described in section 3.6.7. The resulting Nyquist plot is shown in in Figure 64 at room temperature. Fitting the Nyquist plot to an appropriate circuit can be a challenge for SE as they can exhibit non-ideal behaviour. The high-frequency semi-circle corresponds to the grain boundaries. The right point of semicircle determined as the total resistance [150]. The linearity of low-frequency tail was used to analyze the total resistance in the cases a full-semicircle is not observed. The Li^+ ion migration in the ceramic is too rapid not revealing a semi-circle at the highest detection frequency of 6 MHz [150,151]. The calculated ionic conductivity is 2 x 10^{-4} S/cm (2 mS/cm) at room temperature.

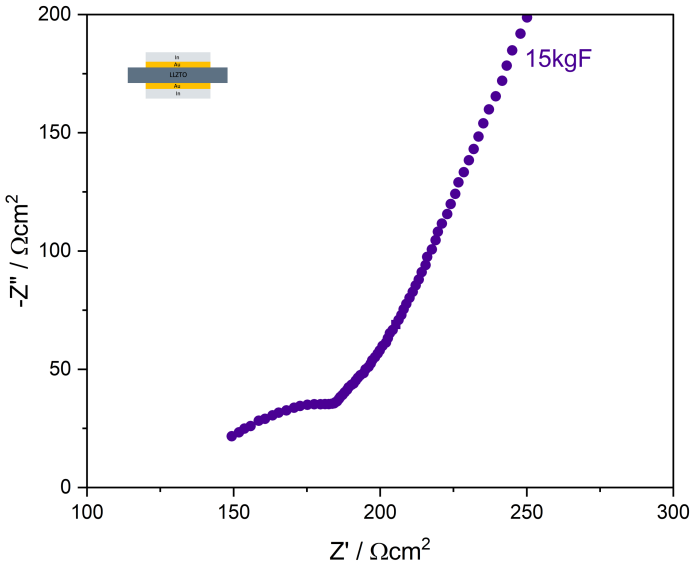

Figure 64: Nyquist plot characterizing 200 µm LLZTO SE with 95% relative density sintered at 1100°C for 1.5h with 10 wt% excess LiOH.

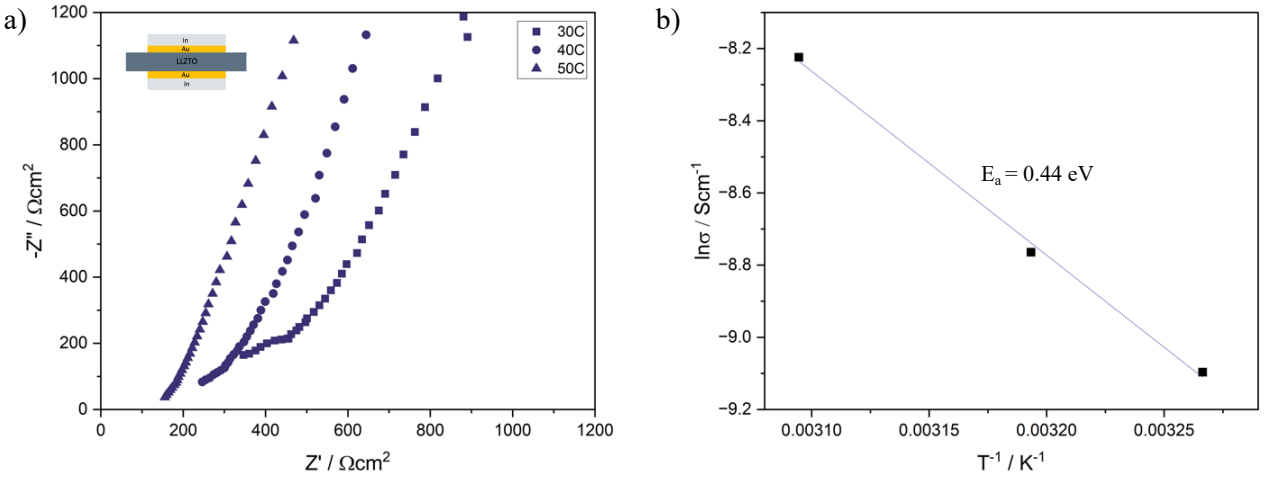

Figure 65: a) Nyquist plot characterizing 217 µm LLZTO SE sintered at 1100 °C for 1.5h with 10wt% excess LiOH at 30, 40, and 50°C and b) Arrhenius plot for LLZO pellet.

As the temperature is increased (applying 15kgF), the semi-circle is smaller, and the total resistance is lower [150,151]. At 50℃, the semicircle nearly vanishes and only a tail is seen (Figure 65). Using the low-frequency tail, the calculated ionic conductivity for 30, 40 and 50℃ is 1.1, 1.6, and 2.7 mS/cm. The temperature-dependent conductivities can linearly fit on a ln$\boldsymbol{\sigma}$ vs. 1/T plot (Figure 65b) using equation 16. The calculated E_a value obtained from slope of the linear fit is 0.44 eV. This represents the low energy barrier the ions need to overcome to move within the LLZO lattice.

The ionic conductivity achieved at room temperature and elevated temperatures is comparable to the 700 µm LLZTO commercial pellet available at MSE Supplies with an ionic conductivity range of 0.4-1 mS/cm. Therefore, the 3D printed LLZTO SE demonstrating 95% relative density obtain a higher ionic conductivity than commercially available SE. In future works, the ionic conductivity can be approximated with more accuracy with the use of an appropriate circuit rather than low-frequency tail approximations done in this work.

4.4.1 EIS Summary

In conclusion, the 3D printed LLZTO SE demonstrated a high ionic conductivity of 2 mS/cm at ambient temperature with 95% relative density for a symmetrical In-Au-LLZTO-Au-In cell. Increasing the temperature increased the ionic conductivity of the ceramic electrolytes to 2.7 mS/cm at 50℃. The calculated activation energy was 0.44 eV. In future works, a Li-LLZTO-Li symmetric cell can be configured to compare ionic conductivities to gold blocking electrodes. Additionally, more research into the fitting of EIS curves can be done to accurately calculate the ionic conductivity of the SE.

Chapter 5 Summary, Conclusions, and Future Work

In this chapter, the research project in this thesis is summarized and conclusions are drawn. The achievements and future works are listed and described.

5.1 Thesis Summary

In this thesis, LLZTO ceramic solid-state electrolytes were fabricated via direct ink writing for all-solid-state battery applications. The ink synthesis, direct ink writing processing, sintering, and electrochemical characterization work is reported.

The electrolyte ink was synthesized using optimized composition of ceramic particles, dispersant, solvents, binder, and plasticizer. It was observed an optimized ink formulation was critical to the processing and drying of the ceramic electrolyte. The suitable ink composition consists of a solid loading of 30-35 wt%, 0.35 wt% MFO dispersant (equivalent to 1 wt% concerning the solid loading), a 3:7 alpha-terpineol to n-butanol ratio, and a 1:1 binder-plasticizer ratio (both at 6.45 wt%). Furthermore, the dispersion and mixing techniques used including magnetic stirring, planetary mixer, and jar-milling with milling media aided to develop a homogeneous ink with minimal agglomerates. A 250 μm tapered tip is recommended for 3D printing since large particle agglomerates can impede printing through fine 250 – 350 μm needle nozzle tips. The wet thickness of the SE can be adjusted by varying the applied pressure, as demonstrated in the volumetric flow model.

Ceramic sintering is an essential process for increasing density through grain growth. The Li loss at temperatures exceeding 1000℃ depletes the cubic phase in LLZO solid electrolytes. Therefore, methods of Li compensation, sintering conditions and set-ups need to be optimized to understand the sintering capability, composition and microstructure relationship. The optimized sintering set-up involves a graphite and MgO plate sandwich within an MgO crucible with excess LiOH around the crucible. This allows for uniform, flat shrinkage in a Li-rich environment resulting in a flat, dense, cubic crystal phase of the final electrolyte. The optimal heating profile is de-binding at 700℃ for 12 hours and sintering at 1100℃ for 1.5 hours with 10 wt% excess LiOH in the MgO crucible. The de-binding and sintering process should be performed in a high-purity argon flow. Furthermore, the electrochemical properties result in a high ionic conductivity (2 mS/cm) and low activation energy (0.44 eV).

5.2 Conclusions

The conclusions are listed as follow.

1. The research presented in this thesis provides an alternative method for fabrication of LLZO ceramic electrolytes – direct ink writing. When compared with alternative fabrication technologies like powder pressing, tape-casting and chemical vapour deposition, direct ink writing has the advantages of easy operation and capable of producing multi-material cathode composite inks. Additionally, this method can be used to create diverse geometries in a wide range of sizes. The preliminary results in this thesis demonstrate the feasibility of using direct ink writing to manufacture ceramic solid-state electrolytes. This conclusion meets objective 2 to fabricate 150 – 250 μm SE using direct ink writing.
2. A known challenge in ceramic manufacturing is the cracking seen during shrinkage (drying and sintering). This phenomenon is directly related to the ink composition. As a result, a suitable ink composition that has appropriate solvent ratios and binder-plasticizer content is developed for the processing and drying of ceramic electrolytes. The solvent ratios assist the ideal drying rate of the ceramic part avoiding cracks. The binder strengthens the ink, while the plasticizer allows for more flexibility in the printed ceramic solid electrolyte. This conclusion meets objective 1 to formulate a ceramic electrolyte ink suitable for direct ink writing.
3. The final step in the processing of ceramic electrolytes is sintering. Although extensively studied in literature, the poor processing results in poor reproducibility impeding the path to commercialization. This research addressed and provided solutions to some common sintering challenges such as reproducibility of a flat, high density solid electrolyte with the desired crystal cubic phase. This conclusion meets objective 3 to find suitable sintering parameters for printed LLZTO ceramic electrolyte.
4. This work presented a correlation between the green thickness of the LLZTO ceramic electrolyte with the Li depletion impurity phase. A green thickness of approximately less than 200, 300, and 400 μm, as much as 20, 10, and 0 wt% excess LiOH is required to compensate for the high-temperature Li loss and maintain the desired cubic crystal phase. To our knowledge, this data has not been presented in literature in a similar manner.
5. The electrochemical analysis of the final sintered solid electrolyte revealed a high ionic conductivity exceeding the ionic conductivity of a thicker bulk pellet commercially available. This signifies the

ability of LLZO to efficiently conduct Li-ions rapidly. This conclusion meets objective 4 to characterize the printed LLZTO ceramic electrolyte.

5.3 Future Works

1. Additive manufacturing demonstrates freeform design capability to enhance the areal energy density and volumetric energy density. In this thesis, printing dense solid electrolytes is demonstrated. However, exploring unique customized designs for specific applications has not been studied. Additionally, a porous ink can be synthesized to add a porous LLZO layer enhancing the battery capacity and improving the integration with cathode material.
2. A cathode ink can be synthesized, and fabricated on top of the sintered LLZO using direct ink writing to create a cathode composite layer on the solid electrolyte increasing the interfacial contact between the cathode and electrolyte. Additionally, features can be printed on dense solid electrolyte to further enhance the interfacial contact.
3. The thickness of the printed LLZTO solid electrolyte is known to greatly impact the Li-depleted LZO impurity phase in the final crystal phase. Further studies can be done to validate the findings of this research and perform statistical analysis for this phenomenon. An understanding of the phase correlation to green thickness can lead to more reproducible results with the desired crystal phase in the future, making us one step closer to commercialization of this LLZO solid electrolyte. This data can also be used to study the Li diffusion at the microstructure scale using x-ray photoelectron spectroscopy.
4. Finally, a 3D printed full cell battery with high energy density Li metal, and high-voltage cathode material can be created for further electrochemical analysis included charging and discharging cycling.

Letters of Copyright Permission

Among the cited figures, Figure 3, 4a, 4b, 7, 9, 11, 17, and 20 are reprinted from open access articles distributed under the terms and conditions of the Creative Commons Attribution license (http://creativecommons.org/licenses/by/3.0/). Permissions for reuse for the remaining figures are obtained from Copyright Clearance Center or PLSclear as follows.

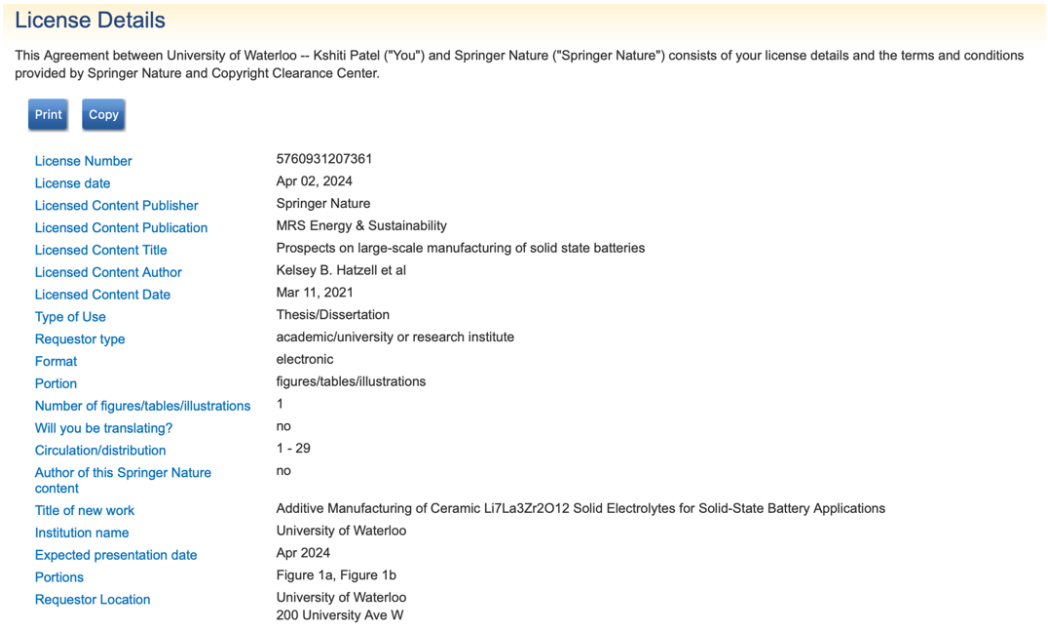

License Details

This Agreement between University of Waterloo -- Kshiti Patel ("You") and Springer Nature ("Springer Nature") consists of your license details and the terms and conditions provided by Springer Nature and Copyright Clearance Center.

Print Copy

License Number	5760931207361
License date	Apr 02, 2024
Licensed Content Publisher	Springer Nature
Licensed Content Publication	MRS Energy & Sustainability
Licensed Content Title	Prospects on large-scale manufacturing of solid state batteries
Licensed Content Author	Kelsey B. Hatzell et al
Licensed Content Date	Mar 11, 2021
Type of Use	Thesis/Dissertation
Requestor type	academic/university or research institute
Format	electronic
Portion	figures/tables/illustrations
Number of figures/tables/illustrations	1
Will you be translating?	no
Circulation/distribution	1 - 29
Author of this Springer Nature content	no
Title of new work	Additive Manufacturing of Ceramic Li7La3Zr2O12 Solid Electrolytes for Solid-State Battery Applications
Institution name	University of Waterloo
Expected presentation date	Apr 2024
Portions	Figure 1a, Figure 1b
Requestor Location	University of Waterloo 200 University Ave W

Permission for Figure 2.

License Details

This Agreement between University of Waterloo -- Kshiti Patel ("You") and Elsevier ("Elsevier") consists of your license details and the terms and conditions provided by Elsevier and Copyright Clearance Center.

Print Copy

License Number	5760991207213
License date	Apr 02, 2024
Licensed Content Publisher	Elsevier
Licensed Content Publication	Chemical Engineering Journal
Licensed Content Title	Prospects of LLZO type solid electrolyte: From material design to battery application
Licensed Content Author	Hongchao Sun,Shifei Kang,Lifeng Cui
Licensed Content Date	Feb 15, 2023
Licensed Content Volume	454
Licensed Content Issue	n/a
Licensed Content Pages	1
Type of Use	reuse in a thesis/dissertation
Portion	figures/tables/illustrations
Number of figures/tables/illustrations	1
Format	electronic
Are you the author of this Elsevier article?	No
Will you be translating?	No
Title of new work	Additive Manufacturing of Ceramic Li7La3Zr2O12 Solid Electrolytes for Solid-State Battery Applications
Institution name	University of Waterloo
Expected presentation date	Apr 2024
Portions	Figure 3
Requestor Location	University of Waterloo 200 University Ave W

Permission for Figure 5.

ACS Publications
Most Trusted. Most Cited. Most Read.

First-Principles Studies on Cation Dopants and Electrolyte|Cathode Interphases for Lithium Garnets

Author: Lincoln J. Miara, William Davidson Richards, Yan E. Wang, et al

Publication: Chemistry of Materials

Publisher: American Chemical Society

Date: Jun 1, 2015

PERMISSION/LICENSE IS GRANTED FOR YOUR ORDER AT NO CHARGE

This type of permission/license, instead of the standard Terms and Conditions, is sent to you because no fee is being charged for your order. Please note the following:

- Permission is granted for your request in both print and electronic formats, and translations.
- If figures and/or tables were requested, they may be adapted or used in part.
- Please print this page for your records and send a copy of it to your publisher/graduate school.
- Appropriate credit for the requested material should be given as follows: "Reprinted (adapted) with permission from {COMPLETE REFERENCE CITATION}. Copyright {YEAR} American Chemical Society." Insert appropriate information in place of the capitalized words.
- One-time permission is granted only for the use specified in your RightsLink request. No additional uses are granted (such as derivative works or other editions). For any uses, please submit a new request.

If credit is given to another source for the material you requested from RightsLink, permission must be obtained from that source.

BACK CLOSE WINDOW

Permission for Figure 6.

License Details

This Agreement between University of Waterloo -- Kshiti Patel ("You") and John Wiley and Sons ("John Wiley and Sons") consists of your license details and the terms and conditions provided by John Wiley and Sons and Copyright Clearance Center.

Print Copy

License Number	5760951121911
License date	Apr 02, 2024
Licensed Content Publisher	John Wiley and Sons
Licensed Content Publication	Advanced Materials
Licensed Content Title	Graphene Oxide-Based Electrode Inks for 3D-Printed Lithium-Ion Batteries
Licensed Content Author	Liangbing Hu, Yue Xu, Zhengyang Wang, et al
Licensed Content Date	Feb 2, 2016
Licensed Content Volume	28
Licensed Content Issue	13
Licensed Content Pages	8
Type of Use	Dissertation/Thesis
Requestor type	University/Academic
Format	Print
Portion	Figure/table
Number of figures/tables	2
Will you be translating?	No
Title of new work	Additive Manufacturing of Ceramic Li7La3Zr2O12 Solid Electrolytes for Solid-State Battery Applications
Institution name	University of Waterloo
Expected presentation date	Apr 2024
Portions	Figure 1, Figure 5i
Requestor Location	University of Waterloo 200 University Ave W

Permission for Figure 12.

License Details

This Agreement between University of Waterloo -- Kshiti Patel ("You") and John Wiley and Sons ("John Wiley and Sons") consists of your license details and the terms and conditions provided by John Wiley and Sons and Copyright Clearance Center.

Print Copy

License Number	5760951441436
License date	Apr 02, 2024
Licensed Content Publisher	John Wiley and Sons
Licensed Content Publication	Advanced Materials
Licensed Content Title	3D-Printing Electrolytes for Solid-State Batteries
Licensed Content Author	Dennis W. McOwen, Shaomao Xu, Yunhui Gong, et al
Licensed Content Date	Mar 25, 2018
Licensed Content Volume	30
Licensed Content Issue	18
Licensed Content Pages	7
Type of Use	Dissertation/Thesis
Requestor type	University/Academic
Format	Print
Portion	Figure/table
Number of figures/tables	3
Will you be translating?	No
Title of new work	Additive Manufacturing of Ceramic Li7La3Zr2O12 Solid Electrolytes for Solid-State Battery Applications
Institution name	University of Waterloo
Expected presentation date	Apr 2024
Portions	Figure 1, Figure 2 d and e, Figure 3
Requestor Location	University of Waterloo 200 University Ave W

Permission for Figure 13 and Figure 14.

License Details

This Agreement between University of Waterloo -- Kshiti Patel ("You") and Elsevier ("Elsevier") consists of your license details and the terms and conditions provided by Elsevier and Copyright Clearance Center.

Print Copy

License Number	5760960103351
License date	Apr 02, 2024
Licensed Content Publisher	Elsevier
Licensed Content Publication	Applied Materials Today
Licensed Content Title	Development of full ceramic electrodes for lithium-ion batteries via desktop-fused filament fabrication and further sintering
Licensed Content Author	José Fernando Valera-Jiménez,Juan Carlos Pérez-Flores,Miguel Castro-García,Jesús Canales-Vázquez
Licensed Content Date	Dec 1, 2021
Licensed Content Volume	25
Licensed Content Issue	n/a
Licensed Content Pages	1
Type of Use	reuse in a thesis/dissertation
Portion	figures/tables/illustrations
Number of figures/tables/illustrations	1
Format	electronic
Are you the author of this Elsevier article?	No
Will you be translating?	No
Title of new work	Additive Manufacturing of Ceramic Li7La3Zr2O12 Solid Electrolytes for Solid-State Battery Applications
Institution name	University of Waterloo
Expected presentation date	Apr 2024
Portions	Figure 3
Requestor Location	University of Waterloo 200 University Ave W

Permission for Figure 15a-d.

License Details

This Agreement between University of Waterloo -- Kshiti Patel ("You") and Springer Nature ("Springer Nature") consists of your license details and the terms and conditions provided by Springer Nature and Copyright Clearance Center.

Print Copy

License Number	5771981291328
License date	Apr 18, 2024
Licensed Content Publisher	Springer Nature
Licensed Content Publication	Journal of Materials Research
Licensed Content Title	Additive manufacturing of 3D batteries: a perspective
Licensed Content Author	Kai Narita et al
Licensed Content Date	Apr 28, 2022
Type of Use	Thesis/Dissertation
Requestor type	academic/university or research institute
Format	electronic
Portion	figures/tables/illustrations
Number of figures/tables/illustrations	2
Will you be translating?	no
Circulation/distribution	1000 - 1999
Author of this Springer Nature content	no
Title of new work	Additive Manufacturing of Ceramic Li7La3Zr2O12 Solid Electrolytes for Solid-State Battery Applications
Institution name	University of Waterloo
Expected presentation date	Apr 2024
Portions	Figure 1, Table 3
Requestor Location	University of Waterloo 200 University Ave W

Permission for Figure 15e and Table 7.

License Details

This Agreement between University of Waterloo -- Kshiti Patel ("You") and John Wiley and Sons ("John Wiley and Sons") consists of your license details and the terms and conditions provided by John Wiley and Sons and Copyright Clearance Center.

Print Copy

License Number	5760960662548
License date	Apr 02, 2024
Licensed Content Publisher	John Wiley and Sons
Licensed Content Publication	ENERGY TECHNOLOGY (ELECTRONIC)
Licensed Content Title	Inkjet Printing of Li-Rich Cathode Material for Thin-Film Lithium-Ion Microbatteries
Licensed Content Author	Maxim Yu. Maximov, Anatoly Popovich, Alexandr Vinogradov, et al
Licensed Content Date	Nov 14, 2019
Licensed Content Volume	8
Licensed Content Issue	3
Licensed Content Pages	11
Type of Use	Dissertation/Thesis
Requestor type	University/Academic
Format	Electronic
Portion	Figure/table
Number of figures/tables	2
Will you be translating?	No
Title of new work	Additive Manufacturing of Ceramic Li7La3Zr2O12 Solid Electrolytes for Solid-State Battery Applications
Institution name	University of Waterloo
Expected presentation date	Apr 2024
Portions	Table 3, Figure 5
Requestor Location	University of Waterloo 200 University Ave W

Permission for Figure 18.

License Details

This Agreement between University of Waterloo -- Kshiti Patel ("You") and Elsevier ("Elsevier") consists of your license details and the terms and conditions provided by Elsevier and Copyright Clearance Center.

Print Copy

License Number	5760960912382
License date	Apr 02, 2024
Licensed Content Publisher	Elsevier
Licensed Content Publication	Joule
Licensed Content Title	Design and Manufacture of 3D-Printed Batteries
Licensed Content Author	Zhiyang Lyu,Gwendolyn J.H. Lim,J. Justin Koh,Yi Li,Yanwen Ma,Jun Ding,Jinlan Wang,Zheng Hu,John Wang,Wei Chen,Yunfei Chen
Licensed Content Date	Jan 20, 2021
Licensed Content Volume	5
Licensed Content Issue	1
Licensed Content Pages	26
Type of Use	reuse in a thesis/dissertation
Portion	figures/tables/illustrations
Number of figures/tables/illustrations	2
Format	electronic
Are you the author of this Elsevier article?	No
Will you be translating?	No
Title of new work	Additive Manufacturing of Ceramic Li7La3Zr2O12 Solid Electrolytes for Solid-State Battery Applications
Institution name	University of Waterloo
Expected presentation date	Apr 2024
Portions	Figure 2, Figure 3c
Requestor Location	University of Waterloo 200 University Ave W

Permission for Figure 21 and Table 6.

License Details

This Agreement between University of Waterloo -- Kshiti Patel ("You") and Elsevier ("Elsevier") consists of your license details and the terms and conditions provided by Elsevier and Copyright Clearance Center.

Print Copy

License Number	5760971492525
License date	Apr 02, 2024
Licensed Content Publisher	Elsevier
Licensed Content Publication	Ceramics International
Licensed Content Title	Optimization of the tape casting process for development of high performance alumina ceramics
Licensed Content Author	Mingxian Yu,Jingxian Zhang,Xiaoguang Li,Hanqin Liang,He Zhong,Yinsheng Li,Yusen Duan,Dong Liang Jiang,Xuejian Liu,Zhengren Huang
Licensed Content Date	Dec 1, 2015
Licensed Content Volume	41
Licensed Content Issue	10
Licensed Content Pages	9
Type of Use	reuse in a thesis/dissertation
Portion	figures/tables/illustrations
Number of figures/tables/illustrations	2
Format	electronic
Are you the author of this Elsevier article?	No
Will you be translating?	No
Title of new work	Additive Manufacturing of Ceramic Li7La3Zr2O12 Solid Electrolytes for Solid-State Battery Applications
Institution name	University of Waterloo
Expected presentation date	Apr 2024
Portions	Figure 4b, Figure 6a
Requestor Location	University of Waterloo 200 University Ave W

Permission for Figure 22a and Figure 24.

ID	Title	ISN	Project Name	Publisher	Date raised	Status
92979	Ceramic Processing and Sintering	9780824709884		Taylor and Francis Group LLC (Books) US	18/04/2024	

Request details

Request comments

This is a PLSclear permission request for resource
Ceramic Processing and Sintering
(9780824709884)
Sourced from PLS
Publisher: Taylor and Francis Group LLC (Books) US
Imprint: Taylor and Francis Group LLC (Books) US
Pub date: Publication date not known
Author: Mohamed N. Rahaman
The requesting user is Kshiti Patel (kshiti.patel@uwaterloo.ca)

Added by: Kshiti Patel - Date: 18/04/2024 02:16:05

Your request has been granted a Free of Charge licence.

Click here to view the licence agreement

Permission for Figure 22b.

License Details

This Agreement between University of Waterloo -- Kshiti Patel ("You") and John Wiley and Sons ("John Wiley and Sons") consists of your license details and the terms and conditions provided by John Wiley and Sons and Copyright Clearance Center.

Print Copy

License Number	5771000857950
License date	Apr 16, 2024
Licensed Content Publisher	John Wiley and Sons
Licensed Content Publication	ENERGY TECHNOLOGY (ELECTRONIC)
Licensed Content Title	Challenges in Lithium-Ion-Battery Slurry Preparation and Potential of Modifying Electrode Structures by Different Mixing Processes
Licensed Content Author	Dorit Nötzel, Hermann Nirschl, Valentin Wenzel
Licensed Content Date	Jun 16, 2015
Licensed Content Volume	3
Licensed Content Issue	7
Licensed Content Pages	7
Type of Use	Dissertation/Thesis
Requestor type	University/Academic
Format	Electronic
Portion	Figure/table
Number of figures/tables	1
Will you be translating?	No
Title of new work	Additive Manufacturing of Ceramic Li7La3Zr2O12 Solid Electrolytes for Solid-State Battery Applications
Institution name	University of Waterloo
Expected presentation date	Apr 2024
Portions	Figure 3
Requestor Location	University of Waterloo 200 University Ave W

Permission for Figure 25.

ACS Publications
Most Trusted. Most Cited. Most Read.

In Situ Neutron Diffraction Monitoring of Li7La3Zr2O12 Formation: Toward a Rational Synthesis of Garnet Solid Electrolytes.

Author: R. Prasada Rao, Wenyi Gu, Neeraj Sharma, et al
Publication: Chemistry of Materials
Publisher: American Chemical Society
Date: Apr 1, 2015

Copyright © 2015, American Chemical Society

PERMISSION/LICENSE IS GRANTED FOR YOUR ORDER AT NO CHARGE

This type of permission/license, instead of the standard Terms and Conditions, is sent to you because no fee is being charged for your order. Please note the following:

- Permission is granted for your request in both print and electronic formats, and translations.
- If figures and/or tables were requested, they may be adapted or used in part.
- Please print this page for your records and send a copy of it to your publisher/graduate school.
- Appropriate credit for the requested material should be given as follows: "Reprinted (adapted) with permission from {COMPLETE REFERENCE CITATION}. Copyright {YEAR} American Chemical Society." Insert appropriate information in place of the capitalized words.
- One-time permission is granted only for the use specified in your RightsLink request. No additional uses are granted (such as derivative works or other editions). For any uses, please submit a new request.

If credit is given to another source for the material you requested from RightsLink, permission must be obtained from that source.

BACK CLOSE WINDOW

Permission for Figure 26.

This is a License Agreement between Kshiti Patel ("User") and Copyright Clearance Center, Inc. ("CCC") on behalf of the Rightsholder identified in the order details below. The license consists of the order details, the Marketplace Permissions General Terms and Conditions below, and any Rightsholder Terms and Conditions which are included below.

All payments must be made in full to CCC in accordance with the Marketplace Permissions General Terms and Conditions below.

Order Date	18-Apr-2024	**Type of Use**	Republish in a thesis/dissertation
Order License ID	1474766-1	**Publisher**	Royal Society of Chemistry
ISSN	2050-7496	**Portion**	Image/photo/illustration

LICENSED CONTENT

Publication Title	Journal of materials chemistry. A, Materials for energy and sustainability	**Publication Type**	e-Journal
Article Title	H 2 O and CO 2 Surface Contamination of the Lithium-Stuffed Garnet	**Start Page**	4960
Author/Editor	Royal Society of Chemistry (Great Britain)	**End Page**	4973
Date	01/01/2013	**Issue**	9
Language	English	**Volume**	10
Country	United Kingdom of Great Britain and Northern Ireland	**URL**	http://pubs.rsc.org/en/journals/journaliss...
Rightsholder	Royal Society of Chemistry		

REQUEST DETAILS

Portion Type	Image/photo/illustration	**Distribution**	Worldwide
Number of Images / Photos / Illustrations	1	**Translation**	Original language of publication
Format (select all that apply)	Electronic	**Copies for the Disabled?**	No
Who Will Republish the Content?	Academic institution	**Minor Editing Privileges?**	No
Duration of Use	Life of current edition	**Incidental Promotional Use?**	No
Lifetime Unit Quantity	Up to 4,999	**Currency**	CAD
Rights Requested	Main product		

NEW WORK DETAILS

Title	Additive Manufacturing of Ceramic Li7La3Zr2O12 Solid Electrolytes for Solid-State Battery Applications	**Institution Name**	University of Waterloo
		Expected Presentation Date	2024-04-30
Instructor Name	Professor Saeed Maleksaeedi		

Permission for Figure 28.

License Details

This Agreement between University of Waterloo -- Kshiti Patel ("You") and Elsevier ("Elsevier") consists of your license details and the terms and conditions provided by Elsevier and Copyright Clearance Center.

Print Copy

License Number	5760981155904
License date	Apr 02, 2024
Licensed Content Publisher	Elsevier
Licensed Content Publication	Journal of the European Ceramic Society
Licensed Content Title	Effects of Li source on microstructure and ionic conductivity of Al-contained Li6.75La3Zr1.75Ta0.25O12 ceramics
Licensed Content Author	Yaoyu Ren,Hui Deng,Rujun Chen,Yang Shen,Yuanhua Lin,Ce-Wen Nan
Licensed Content Date	Feb 1, 2015
Licensed Content Volume	35
Licensed Content Issue	2
Licensed Content Pages	12
Type of Use	reuse in a thesis/dissertation
Portion	figures/tables/illustrations
Number of figures/tables/illustrations	1
Format	electronic
Are you the author of this Elsevier article?	No
Will you be translating?	No
Title of new work	Additive Manufacturing of Ceramic Li7La3Zr2O12 Solid Electrolytes for Solid-State Battery Applications
Institution name	University of Waterloo
Expected presentation date	Apr 2024
Portions	Figure 2
Requestor Location	University of Waterloo 200 University Ave W

Permission for Figure 29.

License Details

This Agreement between University of Waterloo -- Kshiti Patel ("You") and Elsevier ("Elsevier") consists of your license details and the terms and conditions provided by Elsevier and Copyright Clearance Center.

Print Copy

License Number	5760991207213
License date	Apr 02, 2024
Licensed Content Publisher	Elsevier
Licensed Content Publication	Chemical Engineering Journal
Licensed Content Title	Prospects of LLZO type solid electrolyte: From material design to battery application
Licensed Content Author	Hongchao Sun,Shifei Kang,Lifeng Cui
Licensed Content Date	Feb 15, 2023
Licensed Content Volume	454
Licensed Content Issue	n/a
Licensed Content Pages	1
Type of Use	reuse in a thesis/dissertation
Portion	figures/tables/illustrations
Number of figures/tables/illustrations	1
Format	electronic
Are you the author of this Elsevier article?	No
Will you be translating?	No
Title of new work	Additive Manufacturing of Ceramic Li7La3Zr2O12 Solid Electrolytes for Solid-State Battery Applications
Institution name	University of Waterloo
Expected presentation date	Apr 2024
Portions	Figure 3
Requestor Location	University of Waterloo 200 University Ave W

Permission for Figure 30.

License Details

This Agreement between University of Waterloo -- Kshiti Patel ("You") and John Wiley and Sons ("John Wiley and Sons") consists of your license details and the terms and conditions provided by John Wiley and Sons and Copyright Clearance Center.

Print Copy

License Number	5761030228993
License date	Apr 02, 2024
Licensed Content Publisher	John Wiley and Sons
Licensed Content Publication	Advanced Functional Materials
Licensed Content Title	Additive Manufacturing of Batteries
Licensed Content Author	Changyong Cao, Devin MacKenzie, Kent Snyder, et al
Licensed Content Date	Oct 30, 2019
Licensed Content Volume	30
Licensed Content Issue	1
Licensed Content Pages	22
Type of Use	Dissertation/Thesis
Requestor type	University/Academic
Format	Electronic
Portion	Figure/table
Number of figures/tables	1
Will you be translating?	No
Title of new work	Additive Manufacturing of Ceramic Li7La3Zr2O12 Solid Electrolytes for Solid-State Battery Applications
Institution name	University of Waterloo
Expected presentation date	Apr 2024
Portions	Table 2
Requestor Location	University of Waterloo 200 University Ave W

Permission for Table 5.

License Details

This Agreement between University of Waterloo -- Kshiti Patel ("You") and Elsevier ("Elsevier") consists of your license details and the terms and conditions provided by Elsevier and Copyright Clearance Center.

Print Copy

License Number	5760991004183
License date	Apr 02, 2024
Licensed Content Publisher	Elsevier
Licensed Content Publication	Solid State Ionics
Licensed Content Title	Influence of lithium oxide additives on densification and ionic conductivity of garnet-type Li6.75La3Zr1.75Ta0.25O12 solid electrolytes
Licensed Content Author	Yiqiu Li,Yang Cao,Xiangxin Guo
Licensed Content Date	Dec 15, 2013
Licensed Content Volume	253
Licensed Content Issue	n/a
Licensed Content Pages	5
Type of Use	reuse in a thesis/dissertation
Portion	figures/tables/illustrations
Number of figures/tables/illustrations	1
Format	electronic
Are you the author of this Elsevier article?	No
Will you be translating?	No
Title of new work	Additive Manufacturing of Ceramic Li7La3Zr2O12 Solid Electrolytes for Solid-State Battery Applications
Institution name	University of Waterloo
Expected presentation date	Apr 2024
Portions	Table 1
Requestor Location	University of Waterloo 200 University Ave W

Permission for Table 10.

License Details

This Agreement between University of Waterloo -- Kshiti Patel ("You") and John Wiley and Sons ("John Wiley and Sons") consists of your license details and the terms and conditions provided by John Wiley and Sons and Copyright Clearance Center.

Print Copy

License Number	5761031265953
License date	Apr 02, 2024
Licensed Content Publisher	John Wiley and Sons
Licensed Content Publication	Small
Licensed Content Title	Processing and Properties of Garnet-Type Li7La3Zr2O12 Ceramic Electrolytes
Licensed Content Author	Chao Chen, Kexin Wang, Hongying He, et al
Licensed Content Date	Dec 19, 2022
Licensed Content Volume	19
Licensed Content Issue	12
Licensed Content Pages	33
Type of Use	Dissertation/Thesis
Requestor type	University/Academic
Format	Electronic
Portion	Figure/table
Number of figures/tables	1
Will you be translating?	No
Title of new work	Additive Manufacturing of Ceramic Li7La3Zr2O12 Solid Electrolytes for Solid-State Battery Applications
Institution name	University of Waterloo
Expected presentation date	Apr 2024
Portions	Table 1
Requestor Location	University of Waterloo 200 University Ave W

Permission for Table 11.

References

[1] A. Manthiram, X. Yu, S. Wang, Lithium battery chemistries enabled by solid-state electrolytes, Nat Rev Mater 2 (2017). https://doi.org/10.1038/natrevmats.2016.103.

[2] Y. Liu, L. Wang, D. Li, K. Wang, State-of-health estimation of lithium-ion batteries based on electrochemical impedance spectroscopy: a review, Protection and Control of Modern Power Systems 8 (2023). https://doi.org/10.1186/s41601-023-00314-w.

[3] H. Sun, S. Kang, L. Cui, Prospects of LLZO type solid electrolyte: From material design to battery application, Chemical Engineering Journal 454 (2023) 140375. https://doi.org/10.1016/j.cej.2022.140375.

[4] M. Nasir, J. Seo, J.S. Park, H.J. Park, Excellent electrochemical response of Ce stabilized cubic Li7La3Zr2O12, J Eur Ceram Soc (2024). https://doi.org/10.1016/j.jeurceramsoc.2024.01.082.

[5] A. Shahzad, I. Lazoglu, Direct ink writing (DIW) of structural and functional ceramics: Recent achievements and future challenges, Compos B Eng 225 (2021). https://doi.org/10.1016/j.compositesb.2021.109249.

[6] F. Zhang, Z. Li, M. Xu, S. Wang, N. Li, J. Yang, A review of 3D printed porous ceramics, J Eur Ceram Soc 42 (2022) 3351–3373. https://doi.org/10.1016/J.JEURCERAMSOC.2022.02.039.

[7] A. Wolf, P.L. Rosendahl, U. Knaack, Additive manufacturing of clay and ceramic building components, Autom Constr 133 (2022). https://doi.org/10.1016/j.autcon.2021.103956.

[8] K. Huang, H. Elsayed, G. Franchin, P. Colombo, Embedded direct ink writing of freeform ceramic components, Appl Mater Today 23 (2021). https://doi.org/10.1016/j.apmt.2021.101005.

[9] L. del-Mazo-Barbara, M.P. Ginebra, Rheological characterisation of ceramic inks for 3D direct ink writing: A review, J Eur Ceram Soc 41 (2021) 18–33. https://doi.org/10.1016/j.jeurceramsoc.2021.08.031.

[10] F. Hu, T. Mikolajczyk, D.Y. Pimenov, M.K. Gupta, Extrusion-based 3d printing of ceramic pastes: Mathematical modeling and in situ shaping retention approach, Materials 14 (2021). https://doi.org/10.3390/ma14051137.

[11] T. Huang, W. Liu, C. Su, Y. Li, J. Sun, Direct ink writing of conductive materials for emerging energy storage systems, Nano Res (2022). https://doi.org/10.1007/s12274-022-4200-2.

[12] B. Chen, N. Willenbacher, High-precision direct ink writing of Li6.4La3Zr1.4Ta0.6O12, J Eur Ceram Soc 42 (2022) 7491–7500. https://doi.org/10.1016/j.jeurceramsoc.2022.09.018.

[13] M.A.S.R. Saadi, A. Maguire, N.T. Pottackal, M.S.H. Thakur, M.M. Ikram, A.J. Hart, P.M. Ajayan, M.M. Rahman, Direct Ink Writing: A 3D Printing Technology for Diverse Materials, Advanced Materials 34 (2022). https://doi.org/10.1002/adma.202108855.

[14] D.W. McOwen, S. Xu, Y. Gong, Y. Wen, G.L. Godbey, J.E. Gritton, T.R. Hamann, J. Dai, G.T. Hitz, L. Hu, E.D. Wachsman, 3D-Printing Electrolytes for Solid-State Batteries, Advanced Materials 30 (2018). https://doi.org/10.1002/adma.201707132.

[15] Y. Pang, Y. Cao, Y. Chu, M. Liu, K. Snyder, D. MacKenzie, C. Cao, Y. Pang, Y. Cao, Y. Chu, C. Cao, M. Liu, K. Snyder, D. MacKenzie, Additive Manufacturing of Batteries, (2019). https://doi.org/10.1002/adfm.201906244.

[16] C. Sun, Y. Wang, M.D. McMurtrey, N.D. Jerred, F. Liou, J. Li, Additive manufacturing for energy: A review, Appl Energy 282 (2021). https://doi.org/10.1016/j.apenergy.2020.116041.

[17] K. Narita, M.A. Saccone, Y. Sun, J.R. Greer, Additive manufacturing of 3D batteries: a perspective, J Mater Res 37 (2022) 1535–1546. https://doi.org/10.1557/s43578-022-00562-w.

[18] S. Pinilla, S. Ryan, L. McKeon, M. Lian, S. Vaesen, A. Roy, W. Schmitt, J.N. Coleman, V. Nicolosi, Additive Manufacturing of Li-Ion Batteries: A Comparative Study between Electrode Fabrication Processes, Adv Energy Mater (2023). https://doi.org/10.1002/aenm.202203747.

[19] C. Chen, K. Wang, H. He, E. Hanc, M. Kotobuki, L. Lu, Processing and Properties of Garnet-Type Li7La3Zr2O12 Ceramic Electrolytes, Small 19 (2023). https://doi.org/10.1002/smll.202205550.

[20] R.A. Jonson, P.J. McGinn, Tape casting and sintering of Li7La3Zr1.75Nb0.25Al0.1O12 with Li3BO3 additions, Solid State Ion 323 (2018) 49–55. https://doi.org/10.1016/j.ssi.2018.05.015.

[21] L. Yang, Q. Dai, L. Liu, D. Shao, K. Luo, S. Jamil, H. Liu, Z. Luo, B. Chang, X. Wang, Rapid sintering method for highly conductive Li7La3Zr2O12 ceramic electrolyte, Ceram Int 46 (2020) 10917–10924. https://doi.org/10.1016/J.CERAMINT.2020.01.106.

[22] X. Huang, Y. Lu, Z. Song, K. Rui, Q. Wang, T. Xiu, M.E. Badding, Z. Wen, Manipulating Li2O atmosphere for sintering dense Li7La3Zr2O12 solid electrolyte, Energy Storage Mater 22 (2019) 207–217. https://doi.org/10.1016/J.ENSM.2019.01.018.

[23] M. Hong, Q. Dong, H. Xie, ‖ Bryson, C. Clifford, J. Qian, X. Wang, J. Luo, L. Hu, Ultrafast Sintering of Solid-State Electrolytes with Volatile Fillers, Cite This: ACS Energy Lett 6 (2021) 3760. https://doi.org/10.1021/acsenergylett.1c01554.

[24] E. Ramos, A. Browar, J. Roehling, J. Ye, CO 2 Laser Sintering of Garnet-Type Solid-State Electrolytes, 14 (2022) 33. https://doi.org/10.1021/acsenergylett.2c01630.

[25] M. Liu, H. Chen, S. Zhang, G. Li, B. Li, Y. Wen, J. Qiu, J. Chen, P. Zhao, Key factors of the self-consolidation mechanism for sintering Li7La3Zr2O12 solid electrolytes, J Power Sources 556 (2023). https://doi.org/10.1016/j.jpowsour.2022.232447.

[26] Z. Dong, C. Xu, Y. Wu, W. Tang, S. Song, J. Yao, Z. Huang, Z. Wen, L. Lu, N. Hu, Dual substitution and spark plasma sintering to improve ionic conductivity of garnet Li7La3Zr2O12, Nanomaterials 9 (2019). https://doi.org/10.3390/nano9050721.

[27] X. Huang, T. Xiu, M.E. Badding, Z. Wen, Two-step sintering strategy to prepare dense Li-Garnet electrolyte ceramics with high Li + conductivity, (2017). https://doi.org/10.1016/j.ceramint.2017.12.217.

[28] M. Liu, B. Li, S. Zhang, W. Xie, G. Li, Y. Wang, Y. Wen, J. Qiu, J. Chen, P. Zhao, Effect of Nb and Ta Simultaneous Substitution on Self-Consolidation Sintering of Li 7 La 3 Zr 2 O 12, Cite This: ACS Appl. Energy Mater 2022 (2022). https://doi.org/10.1021/acsaem.2c01018.

[29] J.A. Hammons, J.A. Espitia, E. Ramos, R. Shi, F. Meisenkothen, M. Wood, M.R. Cerón, C. Cerón, J. Ye, Pore and grain chemistry during sintering of garnet-type Li 6.4 La 3 Zr 1.4 Ta 0.6 O 12 solid-state electrolytes †, (2022). https://doi.org/10.1039/d1ta10338e.

[30] P. Barai, T. Fister, Y. Liang, J. Libera, M. Wolfman, X. Wang, J. Garcia, H. Iddir, V. Srinivasan, Investigating the Calcination and Sintering of Li 7 La 3 Zr 2 O 12 (LLZO) Solid Electrolytes Using Operando Synchrotron X-ray Characterization and Mesoscale Modeling, Cite This: Chem. Mater 33 (2021) 4352. https://doi.org/10.1021/acs.chemmater.0c04393.

[31] W. Xue, Y. Yang, Q. Yang, Y. Liu, L. Wang, C. Chen, R. Cheng, The effect of sintering process on lithium ionic conductivity of Li 6.4 Al 0.2 La 3 Zr 2 O 12 garnet produced by solid-state synthesis, (2018). https://doi.org/10.1039/c8ra01329b.

[32] X. Zhang, T.-S. Oh, J.W. Fergus, Densification of Ta-Doped Garnet-Type Li 6.75 La 3 Zr 1.75 Ta 0.25 O 12 Solid Electrolyte Materials by Sintering in a Lithium-Rich Air Atmosphere , J Electrochem Soc 166 (2019) A3753–A3759. https://doi.org/10.1149/2.1031915JES/XML.

[33] J.G. Kim, B. Son, S. Mukherjee, N. Schuppert, A. Bates, O. Kwon, M.J. Choi, H.Y. Chung, S. Park, A review of lithium and non-lithium based solid state batteries, J Power Sources 282 (2015) 299–322. https://doi.org/10.1016/j.jpowsour.2015.02.054.

[34] M. Balaish, J.C. Gonzalez-Rosillo, K.J. Kim, Y. Zhu, Z.D. Hood, J.L.M. Rupp, Processing thin but robust electrolytes for solid-state batteries, Nat Energy 6 (2021) 227–239. https://doi.org/10.1038/s41560-020-00759-5.

[35] N. Boaretto, I. Garbayo, S. Valiyaveettil-SobhanRaj, A. Quintela, C. Li, M. Casas-Cabanas, F. Aguesse, Lithium solid-state batteries: State-of-the-art and challenges for materials, interfaces and processing, J Power Sources 502 (2021). https://doi.org/10.1016/j.jpowsour.2021.229919.

[36] W. Zaman, K.B. Hatzell, Processing and manufacturing of next generation lithium-based all solid-state batteries, Curr Opin Solid State Mater Sci 26 (2022). https://doi.org/10.1016/j.cossms.2022.101003.

[37] S. Zhang, Z. Li, L. Cai, Y. Li, V.G. Pol, Enabling safer, ultralong lifespan all-solid-state Li-organic batteries, Chemical Engineering Journal 416 (2021) 129171. https://doi.org/10.1016/J.CEJ.2021.129171.

[38] B.S. Vishnugopi, E. Kazyak, J.A. Lewis, J. Nanda, M.T. McDowell, N.P. Dasgupta, P.P. Mukherjee, Challenges and Opportunities for Fast Charging of Solid-State Lithium Metal Batteries, ACS Energy Lett 6 (2021) 3734–3749. https://doi.org/10.1021/ACSENERGYLETT.1C01352/ASSET/IMAGES/MEDIUM/NZ1C01352_M005.GIF.

[39] X. Chen, Z. Guan, F. Chu, Z. Xue, | Feixiang Wu, Y. Yu, Air-stable inorganic solid-state electrolytes for high energy density lithium batteries: Challenges, strategies, and prospects, (2021). https://doi.org/10.1002/inf2.12248.

[40] C. Wang, K. Fu, S.P. Kammampata, D.W. McOwen, A.J. Samson, L. Zhang, G.T. Hitz, A.M. Nolan, E.D. Wachsman, Y. Mo, V. Thangadurai, L. Hu, Garnet-Type Solid-State Electrolytes: Materials, Interfaces, and Batteries, Chem Rev 120 (2020) 4257–4300. https://doi.org/10.1021/acs.chemrev.9b00427.

[41] L.J. Deiner, C.A.G. Bezerra, T.G. Howell, A.S. Powell, Digital Printing of Solid-State Lithium-Ion Batteries, Adv Eng Mater 21 (2019). https://doi.org/10.1002/adem.201900737.

[42] Q. Zhao, S. Stalin, C.Z. Zhao, L.A. Archer, Designing solid-state electrolytes for safe, energy-dense batteries, Nat Rev Mater 5 (2020) 229–252. https://doi.org/10.1038/s41578-019-0165-5.

[43] J.C. Bachman, S. Muy, A. Grimaud, H.H. Chang, N. Pour, S.F. Lux, O. Paschos, F. Maglia, S. Lupart, P. Lamp, L. Giordano, Y. Shao-Horn, Inorganic Solid-State Electrolytes for Lithium Batteries: Mechanisms and Properties Governing Ion Conduction, Chem Rev 116 (2016) 140–162. https://doi.org/10.1021/acs.chemrev.5b00563.

[44] N.J. Taylor, J. Sakamoto, Solid-state batteries: Unlocking lithium's potential with ceramic solid electrolytes, | American Ceramic Society Bulletin 98 (n.d.). www.ceramics.org (accessed April 12, 2024).

[45] G.E. Blomgren, The Development and Future of Lithium Ion Batteries, J Electrochem Soc 164 (2017) A5019–A5025. https://doi.org/10.1149/2.0251701jes.

[46] K.B. Hatzell, Y. Zheng, Prospects on large-scale manufacturing of solid state batteries, MRS Energy and Sustainability 8 (2021) 33–39. https://doi.org/10.1557/s43581-021-00004-w.

[47] Y. Huang, The discovery of cathode materials for lithium-ion batteries from the view of interdisciplinarity, Interdisciplinary Materials 1 (2022). https://doi.org/10.1002/idm2.12048.

[48] X.-B. Cheng, R. Zhang, C.-Z. Zhao, F. Wei, J.-G. Zhang, Q. Zhang, X.B. Cheng, R. Zhang, C.Z. Zhao, F. Wei, Q. Zhang, J.-G. Zhang, A Review of Solid Electrolyte Interphases on Lithium Metal Anode, (2015). https://doi.org/10.1002/advs.201500213.

[49] J.G. Kim, B. Son, S. Mukherjee, N. Schuppert, A. Bates, O. Kwon, M.J. Choi, H.Y. Chung, S. Park, A review of lithium and non-lithium based solid state batteries, J Power Sources 282 (2015) 299–322. https://doi.org/10.1016/j.jpowsour.2015.02.054.

[50] A.J. Samson, K. Hofstetter, S. Bag, V. Thangadurai, A bird's-eye view of Li-stuffed garnet-type Li7La3Zr2O12 ceramic electrolytes for advanced all-solid-state Li batteries, Energy Environ Sci 12 (2019). https://doi.org/10.1039/c9ee01548e.

[51] L. Cheng, H. Hou, S. Lux, R. Kostecki, R. Davis, V. Zorba, A. Mehta, M. Doeff, Enhanced lithium ion transport in garnet-type solid state electrolytes, J Electroceram 38 (2017) 168–175. https://doi.org/10.1007/s10832-017-0080-3.

[52] S. Cao, S. Song, X. Xiang, Q. Hu, C. Zhang, Z. Xia, Y. Xu, W. Zha, J. Li, P.M. Gonzale, Y.H. Han, F. Chen, Modeling, preparation, and elemental doping of Li7La3Zr2O12 garnet-type solid electrolytes: A review, Journal of the Korean Ceramic Society 56 (2019) 111–129. https://doi.org/10.4191/kcers.2019.56.2.01.

[53] A. Kim, S. Woo, M. Kang, H. Park, B. Kang, Research Progresses of Garnet-Type Solid Electrolytes for Developing All-Solid-State Li Batteries, Front Chem 8 (2020). https://doi.org/10.3389/fchem.2020.00468.

[54] P.M. Gonzalez Puente, S. Song, S. Cao, L.Z. Rannalter, Z. Pan, X. Xiang, Q. Shen, F. Chen, Garnet-type solid electrolyte: Advances of ionic transport performance and its application in all-solid-state batteries, Journal of Advanced Ceramics 10 (2021). https://doi.org/10.1007/s40145-021-0489-7.

[55] F. Shen, W. Guo, D. Zeng, Z. Sun, J. Gao, J. Li, B. Zhao, B. He, X. Han, A Simple and Highly Efficient Method toward High-Density Garnet-Type LLZTO Solid-State Electrolyte, Cite This: ACS Appl. Mater. Interfaces 12 (2020) 30319. https://doi.org/10.1021/acsami.0c04850.

[56] Densification of Ta-Doped Garnet-Type Li 6.75 La 3 Zr 1.75 Ta 0.25 O 12 Solid Electrolyte Materials by Sintering in a Lithium-Rich Air Atmosphere, (2019). https://doi.org/10.1149/2.1031915jes.

[57] X. Huang, Y. Lu, Z. Song, T. Xiu, M.E. Badding, Z. Wen, Preparation of dense Ta-LLZO/MgO composite Li-ion solid electrolyte: Sintering, microstructure, performance and the role of MgO, Journal of Energy Chemistry 39 (2019) 8–16. https://doi.org/10.1016/j.jechem.2019.01.013.

[58] M. Ihrig, T.P. Mishra, W.S. Scheld, G. Häuschen, W. Rheinheimer, M. Bram, M. Finsterbusch, O. Guillon, Li7La3Zr2O12 solid electrolyte sintered by the ultrafast high-temperature method, J Eur Ceram Soc 41 (2021) 6075–6079. https://doi.org/10.1016/J.JEURCERAMSOC.2021.05.041.

[59] F. Okur, H. Zhang, D.T. Karabay, K. Muench, A. Parrilli, A. Neels, W. Dachraoui, M.D. Rossell, C. Cancellieri, L.P.H. Jeurgens, K. V. Kravchyk, M. V. Kovalenko, Intermediate-Stage Sintered LLZO Scaffolds for Li-Garnet Solid-State Batteries, Adv Energy Mater 13 (2023). https://doi.org/10.1002/aenm.202203509.

[60] W. Xia, B. Xu, H. Duan, Y. Guo, H. Kang, H. Li, H. Liu, Ionic Conductivity and Air Stability of Al-Doped Li7La3Zr2O12 Sintered in Alumina and Pt Crucibles, ACS Appl Mater Interfaces 8 (2016) 5335–5342. https://doi.org/10.1021/acsami.5b12186.

[61] A. Kern, P.J. McGinn, Ultrafast high-temperature sintering of Li7La3Zr1.75Nb0.25Al0.15O12 (LLZO), J Eur Ceram Soc 42 (2022) 7501–7507. https://doi.org/10.1016/J.JEURCERAMSOC.2022.08.054.

[62] X. Tao, L. Yang, J. Liu, Z. Zang, P. Zeng, C. Zou, L. Yi, X. Chen, X. Liu, X. Wang, Preparation and performances of gallium-doped LLZO electrolyte with high ionic conductivity by rapid ultra-high-temperature sintering, J Alloys Compd 937 (2023) 168380. https://doi.org/10.1016/J.JALLCOM.2022.168380.

[63] S. Li, S.Q. Zhang, L. Shen, Q. Liu, J. Bin Ma, W. Lv, Y.B. He, Q.H. Yang, Progress and Perspective of Ceramic/Polymer Composite Solid Electrolytes for Lithium Batteries, Advanced Science 7 (2020). https://doi.org/10.1002/advs.201903088.

[64] X. Chen, Z. Guan, F. Chu, Z. Xue, F. Wu, Y. Yu, Air-stable inorganic solid-state electrolytes for high energy density lithium batteries: Challenges, strategies, and prospects, InfoMat 4 (2022). https://doi.org/10.1002/inf2.12248.

[65] S. Yu, R.D. Schmidt, R. Garcia-Mendez, E. Herbert, N.J. Dudney, J.B. Wolfenstine, J. Sakamoto, D.J. Siegel, Elastic Properties of the Solid Electrolyte Li7La3Zr2O12 (LLZO), Chemistry of Materials 28 (2016). https://doi.org/10.1021/acs.chemmater.5b03854.

[66] Y. Zhu, J.G. Connell, S. Tepavcevic, P. Zapol, R. Garcia-Mendez, N.J. Taylor, J. Sakamoto, B.J. Ingram, L.A. Curtiss, J.W. Freeland, D.D. Fong, N.M. Markovic, Dopant-Dependent Stability of Garnet Solid Electrolyte Interfaces with Lithium Metal, Adv Energy Mater 9 (2019). https://doi.org/10.1002/aenm.201803440.

[67] T. Thompson, J. Wolfenstine, J.L. Allen, M. Johannes, A. Huq, I.N. David, J. Sakamoto, Tetragonal vs. cubic phase stability in Al-free Ta doped Li 7La3Zr2O12 (LLZO), J Mater Chem A Mater 2 (2014) 13431–13436. https://doi.org/10.1039/C4TA02099E.

[68] E. Ilina, E. Lyalin, M. Vlasov, A. Kabanov, K. Okhotnikov, E. Sherstobitova, M. Zobel, Structural Features and the Li-Ion Diffusion Mechanism in Tantalum-Doped Li7La3Zr2O12Solid Electrolytes, ACS Appl Energy Mater 5 (2022) 2959–2967. https://doi.org/10.1021/acsaem.1c03632.

[69] S. Umesh, V.K. Jayaraman, A.S. Prakash, Elucidating the Importance of Quaternary Dopants in Stabilizing Cubic LLZO at Low Temperature, Journal of Physical Chemistry C 128 (2024) 985–993. https://doi.org/10.1021/acs.jpcc.3c05362.

[70] L.J. Miara, W.D. Richards, Y.E. Wang, G. Ceder, First-Principles Studies on Cation Dopants and Electrolyte|Cathode Interphases for Lithium Garnets, Chemistry of Materials 27 (2015) 4040–4047. https://doi.org/10.1021/acs.chemmater.5b01023.

[71] Y. Liu, R. Zhang, J. Wang, Y. Wang, Current and future lithium-ion battery manufacturing, Cell Press (2021). https://doi.org/10.1016/j.isci.

[72] V. Wenzel, H. Nirschl, D. Nötzel, Challenges in Lithium-Ion-Battery Slurry Preparation and Potential of Modifying Electrode Structures by Different Mixing Processes, Energy Technology 3 (2015) 692–698. https://doi.org/10.1002/ente.201402218.

[73] F. Zhang, M. Wei, V. V. Viswanathan, B. Swart, Y. Shao, G. Wu, C. Zhou, 3D printing technologies for electrochemical energy storage, Nano Energy 40 (2017) 418–431. https://doi.org/10.1016/j.nanoen.2017.08.037.

[74] P. Chang, H. Mei, S. Zhou, K.G. Dassios, L. Cheng, 3D printed electrochemical energy storage devices, J Mater Chem A Mater 7 (2019) 4230–4258. https://doi.org/10.1039/c8ta11860d.

[75] Z. Lyu, G.J.H. Lim, J.J. Koh, Y. Li, Y. Ma, J. Ding, J. Wang, Z. Hu, J. Wang, W. Chen, Y. Chen, Design and Manufacture of 3D-Printed Batteries, Joule 5 (2021) 89–114. https://doi.org/10.1016/j.joule.2020.11.010.

[76] B. Trembacki, E. Duoss, G. Oxberry, M. Stadermann, J. Murthy, Mesoscale Electrochemical Performance Simulation of 3D Interpenetrating Lithium-Ion Battery Electrodes, J Electrochem Soc 166 (2019) A923–A934. https://doi.org/10.1149/2.0031906JES/XML.

[77] U. Gulzar, C. Glynn, C. O'Dwyer, Additive manufacturing for energy storage: Methods, designs and material selection for customizable 3D printed batteries and supercapacitors, Curr Opin Electrochem 20 (2020) 46–53. https://doi.org/10.1016/j.coelec.2020.02.009.

[78] C. Zhu, T. Liu, F. Qian, W. Chen, S. Chandrasekaran, B. Yao, Y. Song, E.B. Duoss, J.D. Kuntz, C.M. Spadaccini, M.A. Worsley, Y. Li, 3D printed functional nanomaterials for electrochemical energy storage, Nano Today 15 (2017) 107–120. https://doi.org/10.1016/j.nantod.2017.06.007.

[79] S. Tagliaferri, A. Panagiotopoulos, C. Mattevi, Direct ink writing of energy materials, Mater Adv 2 (2021) 540–563. https://doi.org/10.1039/d0ma00753f.

[80] K.S. Pandya, S.S. Shindalkar, B. Kandasubramanian, Breakthrough to the pragmatic evolution of direct ink writing: progression, challenges, and future, Progress in Additive Manufacturing (2023). https://doi.org/10.1007/s40964-023-00399-7.

[81] A. Chen, C. Qu, Y. Shi, F. Shi, Manufacturing Strategies for Solid Electrolyte in Batteries, Front Energy Res 8 (2020). https://doi.org/10.3389/fenrg.2020.571440.

[82] X. Ang, J.Y. Tey, W.H. Yeo, K.P.Y. Shak, A review on metallic and ceramic material extrusion method: Materials, rheology, and printing parameters, J Manuf Process 90 (2023) 28–42. https://doi.org/10.1016/j.jmapro.2023.01.077.

[83] K.; Xu, D.; Li, E.; Shang, A Heating-Assisted Direct Ink Writing Method for Preparation of PDMS Cellular Structure with High Manufacturing Fidelity, (2022). https://doi.org/10.3390/polym14071323.

[84] K. Fu, Y. Wang, C. Yan, Y. Yao, Y. Chen, J. Dai, S. Lacey, Y. Wang, J. Wan, T. Li, Z. Wang, Y. Xu, L. Hu, Graphene Oxide-Based Electrode Inks for 3D-Printed Lithium-Ion Batteries, Advanced Materials 28 (2016) 2587–2594. https://doi.org/10.1002/adma.201505391.

[85] J.F. Valera-Jiménez, J.C. Pérez-Flores, M. Castro-García, J. Canales-Vázquez, Development of full ceramic electrodes for lithium-ion batteries via desktop-fused filament fabrication and further sintering, Appl Mater Today 25 (2021). https://doi.org/10.1016/j.apmt.2021.101243.

[86] K. Sztymela, M. Bienia, F. Rossignol, S. Mailley, S. Ziesche, J. Varghese, M. Cerbelaud, Fabrication of modern lithium ion batteries by 3D inkjet printing: opportunities and challenges, Heliyon 8 (2022). https://doi.org/10.1016/j.heliyon.2022.e12623.

[87] H.Y. Jun, S.J. Kim, C.H. Choi, Ink formulation and printing parameters for inkjet printing of two dimensional materials: A mini review, Nanomaterials 11 (2021). https://doi.org/10.3390/nano11123441.

[88] D.S. Kolchanov, I. Mitrofanov, A. Kim, Y. Koshtyal, A. Rumyantsev, E. Sergeeva, A. Vinogradov, A. Popovich, M.Y. Maximov, Inkjet Printing of Li-Rich Cathode Material for Thin-Film Lithium-Ion Microbatteries, Energy Technology 8 (2020). https://doi.org/10.1002/ente.201901086.

[89] J. Schnell, T. Günther, T. Knoche, C. Vieider, L. Köhler, A. Just, M. Keller, S. Passerini, G. Reinhart, All-solid-state lithium-ion and lithium metal batteries – paving the way to large-scale production, J Power Sources 382 (2018) 160–175. https://doi.org/10.1016/j.jpowsour.2018.02.062.

[90] K. Wudy, S. Sapishchuk, J. Hofmann, J. Schmidt, F. Konwitschny, H.C. Töpper, R. Daub, Polymer-based separator for all-solid-state batteries produced by additive manufacturing, J Appl Polym Sci 140 (2023). https://doi.org/10.1002/app.53690.

[91] N. Boaretto, I. Garbayo, S. Valiyaveettil-SobhanRaj, A. Quintela, C. Li, M. Casas-Cabanas, F. Aguesse, Lithium solid-state batteries: State-of-the-art and challenges for materials, interfaces and processing, J Power Sources 502 (2021). https://doi.org/10.1016/j.jpowsour.2021.229919.

[92] Y. Liu, R. Zhang, J. Wang, Y. Wang, iScience Perspective Current and future lithium-ion battery manufacturing, (n.d.). https://doi.org/10.1016/j.isci.

[93] M.N. Rahaman, Ceramic processing and sintering, second edition, 2017. https://doi.org/10.1201/9781315274126.

[94] B. Dai, M. Zhou, K. Liu, B. He, B. Xiang, L. Kong, The molding of the ceramic solid electrolyte sheet prepared by tape casting, in: J Phys Conf Ser, Institute of Physics, 2023. https://doi.org/10.1088/1742-6596/2566/1/012102.

[95] A. Parejiya, M.B. Dixit, D. Parikh, R. Amin, R. Essehli, J. Li, D.L. Wood, I. Belharouak, Understanding slurry formulations to guide solution-processing of solid electrolytes, J Power Sources 544 (2022). https://doi.org/10.1016/j.jpowsour.2022.231894.

[96] Y. Duan, J. Zhang, X. Li, Y. Shi, J. Xie, D. Jiang, Optimization of the tape casting process for the development of high performance silicon nitride substrate, Int J Appl Ceram Technol 14 (2017) 712–718. https://doi.org/10.1111/ijac.12679.

[97] M. Yu, J. Zhang, X. Li, H. Liang, H. Zhong, Y. Li, Y. Duan, D.L. Jiang, X. Liu, Z. Huang, Optimization of the tape casting process for development of high performance alumina ceramics, Ceram Int 41 (2015) 14845–14853. https://doi.org/10.1016/j.ceramint.2015.08.010.

[98] F. Shen, M.B. Dixit, W. Zaman, N. Hortance, B. Rogers, K.B. Hatzell, Composite Electrode Ink Formulation for All Solid-State Batteries, J Electrochem Soc 166 (2019) A3182–A3188. https://doi.org/10.1149/2.0141914jes.

[99] Z. Liu, D.D.L. Chung, Burnout of the Organic Vehicle in an Electrically Conductive Thick-Film Paste, 2004.

[100] A. Kraytsberg, Y. Ein-Eli, Conveying Advanced Li-ion Battery Materials into Practice The Impact of Electrode Slurry Preparation Skills, Adv Energy Mater 6 (2016). https://doi.org/10.1002/aenm.201600655.

[101] R.F. Conley, Practical Dispersion: A Guide to Understanding and Formulating Slurries, (1996) 464. https://www.wiley.com/en-ca/Practical+Dispersion%3A+A+Guide+to+Understanding+and+Formulating+Slurries-p-9780471186403 (accessed April 12, 2024).

[102] J. Zhang, M. Yarahmadi, L. Cabezas, M. Serra, S. Elizalde, J.M. Cabrera, L. Llanes, G. Fargas, Robocasting of dense 8Y zirconia parts: Rheology, printing, and mechanical

properties, J Eur Ceram Soc 43 (2023) 2794–2804. https://doi.org/10.1016/j.jeurceramsoc.2022.11.042.

[103] T. Chen, A. Sun, C. Chu, H. Wu, J. Wang, J. Wang, Z. Li, J. Guo, G. Xu, Rheological behavior of titania ink and mechanical properties of titania ceramic structures by 3D direct ink writing using high solid loading titania ceramic ink, J Alloys Compd 783 (2019) 321–328. https://doi.org/10.1016/j.jallcom.2018.12.334.

[104] Y. yun Li, L. tu Li, B. Li, Direct write printing of three-dimensional ZrO2 biological scaffolds, Mater Des 72 (2015) 16–20. https://doi.org/10.1016/j.matdes.2015.02.018.

[105] I.K. Jones, Z.M. Seeley, N.J. Cherepy, E.B. Duoss, S.A. Payne, Direct ink write fabrication of transparent ceramic gain media, Opt Mater (Amst) 75 (2018) 19–25. https://doi.org/10.1016/j.optmat.2017.10.005.

[106] Z. Lu, Y. Xia, K. Miao, S. Li, L. Zhu, H. Nan, J. Cao, D. Li, Microstructure control of highly oriented short carbon fibres in SiC matrix composites fabricated by direct ink writing, Ceram Int 45 (2019) 17262–17267. https://doi.org/10.1016/j.ceramint.2019.05.283.

[107] B. Coppola, C. Tardivat, S. Richaud, J.M. Tulliani, L. Montanaro, P. Palmero, 3D printing of dense and porous alkali-activated refractory wastes via Direct Ink Writing (DIW), J Eur Ceram Soc 41 (2021) 3798–3808. https://doi.org/10.1016/j.jeurceramsoc.2021.01.019.

[108] K. Zhu, D. Yang, Z. Yu, Y. Ma, S. Zhang, R. Liu, J. Li, J. Cui, H. Yuan, Additive manufacturing of SiO2–Al2O3 refractory products via Direct Ink Writing, Ceram Int 46 (2020) 27254–27261. https://doi.org/10.1016/j.ceramint.2020.07.210.

[109] X. Huang, Y. Lu, H. Guo, Z. Song, T. Xiu, M.E. Badding, Z. Wen, None-Mother-Powder Method to Prepare Dense Li-Garnet Solid Electrolytes with High Critical Current Density, (2018). https://doi.org/10.1021/acsaem.8b00976.

[110] M. Rosen, R. Ye, M. Mann, S. Lobe, M. Finsterbusch, O. Guillon, D. Fattakhova-Rohlfing, Controlling the lithium proton exchange of LLZO to enable reproducible processing and performance optimization †, (2021). https://doi.org/10.1039/d0ta11096e.

[111] W. Lu, T. Wang, M. Xue, C. Zhang, Improved Li6.5La3Zr1.5Nb0.5O12 electrolyte and effects of atmosphere exposure on conductivities, J Power Sources 497 (2021). https://doi.org/10.1016/j.jpowsour.2021.229845.

[112] Y. Kim, A. Yoo, R. Schmidt, A. Sharafi, H. Lee, J. Wolfenstine, J. Sakamoto, Electrochemical stability of Li 6.5 La 3 Zr 1.5 M 0.5 O 12 (M = Nb or Ta) against metallic lithium, Front Energy Res 4 (2016). https://doi.org/10.3389/fenrg.2016.00020.

[113] J. Li, Z. Liu, W. Ma, H. Dong, K. Zhang, R. Wang, Low-temperature synthesis of cubic phase Li 7 La 3 Zr 2 O 12 via sol-gel and ball milling induced phase transition, (2018). https://doi.org/10.1016/j.jpowsour.2018.11.040.

[114] K. Tadanaga, R. Takano, T. Ichinose, S. Mori, A. Hayashi, M. Tatsumisago, Low temperature synthesis of highly ion conductive Li7La 3Zr2O12-Li3BO3 composites, Electrochem Commun 33 (2013) 51–54. https://doi.org/10.1016/j.elecom.2013.04.004.

[115] E. Yi, W. Wang, J. Kieffer, R.M. Laine, Key parameters governing the densification of cubic-Li7La3Zr2O12 Li+ conductors, J Power Sources 352 (2017) 156–164. https://doi.org/10.1016/j.jpowsour.2017.03.126.

[116] K. Kim, S.-H. Yang, M. Young Kim, M. Sung Lee, J. Lim, D. Rye Chang, H.-S. Kim, Cubic phase behavior and lithium ion conductivity of Li 7 La 3 Zr 2 O 12 prepared by co-precipitation synthesis for all-solid batteries, Journal of Industrial and Engineering Chemistry 36 (2016) 279–283. https://doi.org/10.1016/j.jiec.2016.02.016.

[117] Y. Xiao, Y. Wang, S.H. Bo, J.C. Kim, L.J. Miara, G. Ceder, Understanding interface stability in solid-state batteries, Nat Rev Mater 5 (2020). https://doi.org/10.1038/s41578-019-0157-5.

[118] K. Gao, M. He, Y. Li, Y. Zhang, J. Gao, X. Li, Z. Cui, Z. Zhan, T. Zhang, Preparation of high-density garnet thin sheet electrolytes for all-solid-state Li-Metal batteries by tape-casting technique, J Alloys Compd 791 (2019) 923–928. https://doi.org/10.1016/j.jallcom.2019.03.409.

[119] H. Zhang, F. Okur, C. Cancellieri, L.P.H. Jeurgens, A. Parrilli, D.T. Karabay, M. Nesvadba, S. Hwang, A. Neels, M. V. Kovalenko, K. V. Kravchyk, Bilayer Dense-Porous Li7La3Zr2O12 Membranes for High-Performance Li-Garnet Solid-State Batteries, Advanced Science 10 (2023). https://doi.org/10.1002/advs.202205821.

[120] Z. Fu, L. Zhang, J.E. Gritton, G. Godbey, T. Hamann, Y. Gong, D. Mcowen, E. Wachsman, Probing the Mechanical Properties of a Doped Li 7 La 3 Zr 2 O 12 Garnet Thin Electrolyte for

Solid-State Batteries, Cite This: ACS Appl. Mater. Interfaces 12 (2020). https://doi.org/10.1021/acsami.0c01681.

[121] A. Paolella, W. Zhu, G. Bertoni, S. Savoie, Z. Feng, H. Demers, V. Gariepy, G. Girard, E. Rivard, N. Delaporte, A. Guerfi, H. Lorrmann, C. George, K. Zaghib, Discovering the Influence of Lithium Loss on Garnet Li7La3Zr2O12Electrolyte Phase Stability, ACS Appl Energy Mater 3 (2020). https://doi.org/10.1021/acsaem.9b02401.

[122] Y. Chen, E. Rangasamy, C.R. Dela Cruz, C. Liang, K. An, A study of suppressed formation of low-conductivity phases in doped Li7La3Zr2O12 garnets by in situ neutron diffraction, J Mater Chem A Mater 3 (2015) 22868–22876. https://doi.org/10.1039/c5ta04902d.

[123] R.P. Rao, W. Gu, N. Sharma, V.K. Peterson, M. Avdeev, S. Adams, In Situ Neutron Diffraction Monitoring of Li7La3Zr2O12 Formation: Toward a Rational Synthesis of Garnet Solid Electrolytes, Australia Chem. Mater 01 (2015) 41. https://doi.org/10.1021/acs.chemmater.5b00149.

[124] G. Han, B. Kinzer, R. Garcia-Mendez, H. Choe, J. Wolfenstine, J. Sakamoto, Correlating the effect of dopant type (Al, Ga, Ta) on the mechanical and electrical properties of hot-pressed Li-garnet electrolyte, J Eur Ceram Soc 40 (2020). https://doi.org/10.1016/j.jeurceramsoc.2019.12.054.

[125] H. Salimkhani, A. Yurum, S.A. Gursel, A glance at the influence of different dopant elements on Li7La3Zr2O12 garnets, Ionics (Kiel) 27 (2021). https://doi.org/10.1007/s11581-021-04152-4.

[126] J. Košir, S. Mousavihashemi, B.P. Wilson, E.L. Rautama, T. Kallio, Comparative analysis on the thermal, structural, and electrochemical properties of Al-doped Li7La3Zr2O12 solid electrolytes through solid state and sol-gel routes, Solid State Ion 380 (2022). https://doi.org/10.1016/j.ssi.2022.115943.

[127] D.O. Shin, K. Oh, K.M. Kim, K.Y. Park, B. Lee, Y.G. Lee, K. Kang, Synergistic multi-doping effects on the Li7La3Zr2O12 solid electrolyte for fast lithium ion conduction, Sci Rep 5 (2015). https://doi.org/10.1038/srep18053.

[128] B. Xu, H. Duan, W. Xia, Y. Guo, H. Kang, H. Li, H. Liu, Multistep sintering to synthesize fast lithium garnets, J Power Sources 302 (2016) 291–297. https://doi.org/10.1016/j.jpowsour.2015.10.084.

[129] Y. Li, A.M. Prabhu, T.S. Choksi, P. Canepa, H 2 O and CO 2 surface contamination of the lithium garnet Li 7 La 3 Zr 2 O 12 solid electrolyte , J Mater Chem A Mater 10 (2022) 4960–4973. https://doi.org/10.1039/d1ta10228a.

[130] K. Liu, J.T. Ma, C.A. Wang, Excess lithium salt functions more than compensating for lithium loss when synthesizing Li6.5La3Ta0.5Zr 1.5O12 in alumina crucible, J Power Sources 260 (2014) 109–114. https://doi.org/10.1016/j.jpowsour.2014.02.065.

[131] S. Ohta, S. Komagata, J. Seki, T. Saeki, S. Morishita, T. Asaoka, Short communication All-solid-state lithium ion battery using garnet-type oxide and Li3BO3 solid electrolytes fabricated by screen-printing, J Power Sources 238 (2013) 53–56. https://doi.org/10.1016/j.jpowsour.2013.02.073.

[132] H. Xie, C. Li, W.H. Kan, M. Avdeev, C. Zhu, Z. Zhao, X. Chu, D. Mu, F. Wu, Consolidating the grain boundary of the garnet electrolyte LLZTO with Li3BO3 for high-performance LiNi0.8Co0.1Mn0.1O2/LiFePO4 hybrid solid batteries, J Mater Chem A Mater 7 (2019) 20633–20639. https://doi.org/10.1039/c9ta03263k.

[133] Y. Li, Y. Cao, X. Guo, Influence of lithium oxide additives on densification and ionic conductivity of garnet-type Li6.75La3Zr 1.75Ta0.25O12 solid electrolytes, Solid State Ion 253 (2013) 76–80. https://doi.org/10.1016/j.ssi.2013.09.005.

[134] S. Ohta, J. Seki, Y. Yagi, Y. Kihira, T. Tani, T. Asaoka, Co-sinterable lithium garnet-type oxide electrolyte with cathode for all-solid-state lithium ion battery, J Power Sources 265 (2014) 40–44. https://doi.org/10.1016/j.jpowsour.2014.04.065.

[135] Y. Tang, Z. Luo, T. Liu, P. Liu, Z. Li, A. Lu, Effects of B2O3 on microstructure and ionic conductivity of Li6.5La3Zr1.5Nb0.5O12 solid electrolyte, Ceram Int 43 (2017) 11879–11884. https://doi.org/10.1016/j.ceramint.2017.06.035.

[136] Z. Zhang, A.R. Gonzalez, K.L. Choy, Boron Nitride Enhanced Garnet-Type (Li6.25Al0.25La3Zr2O12) Ceramic Electrolyte for an All-Solid-State Lithium-Ion Battery, ACS Appl Energy Mater 2 (2019). https://doi.org/10.1021/acsaem.9b01431.

[137] W. Zhang, C. Sun, Effects of CuO on the microstructure and electrochemical properties of garnet-type Li6.3La3Zr1.65W0.35O12 solid electrolyte, Journal of Physics and Chemistry of Solids 135 (2019). https://doi.org/10.1016/j.jpcs.2019.109080.

[138] X. Huang, C. Shen, K. Rui, J. Jin, M. Wu, X. Wu, Z. Wen, Influence of La2Zr2O7 Additive on Densification and Li+ Conductivity for Ta-Doped Li7La3Zr2O12 Garnet, JOM 68 (2016) 2593–2600. https://doi.org/10.1007/s11837-016-2065-0.

[139] M. Wood, X. Gao, R. Shi, T.W. Heo, J.A. Espitia, E.B. Duoss, B.C. Wood, J. Ye, Exploring the relationship between solvent-assisted ball milling, particle size, and sintering temperature in garnet-type solid electrolytes, J Power Sources 484 (2021). https://doi.org/10.1016/J.JPOWSOUR.2020.229252.

[140] Y. Ren, H. Deng, R. Chen, Y. Shen, Y. Lin, C.W. Nan, Effects of Li source on microstructure and ionic conductivity of Al-contained Li6.75La3Zr1.75Ta0.25O12 ceramics, J Eur Ceram Soc 35 (2015) 561–572. https://doi.org/10.1016/J.JEURCERAMSOC.2014.09.007.

[141] K.K. Fu, Y. Gong, B. Liu, Y. Zhu, S. Xu, Y. Yao, W. Luo, C. Wang, S.D. Lacey, J. Dai, Y. Chen, Y. Mo, E. Wachsman, L. Hu, Toward garnet electrolyte–based Li metal batteries: An ultrathin, highly effective, artificial solid-state electrolyte/metallic Li interface, Sci Adv 3 (2017). https://doi.org/10.1126/SCIADV.1601659.

[142] F. Shen, M.B. Dixit, X. Xiao, K.B. Hatzell, Effect of Pore Connectivity on Li Dendrite Propagation within LLZO Electrolytes Observed with Synchrotron X-ray Tomography, ACS Energy Lett 3 (2018) 1056–1061. https://doi.org/10.1021/acsenergylett.8b00249.

[143] H. Zhang, F. Okur, B. Pant, M. Klimpel, S. Butenko, D.T. Karabay, A. Parrilli, A. Neels, Y. Cao, K. V. Kravchyk, M. V. Kovalenko, Garnet-Based Solid-State Li Batteries with High-Surface-Area Porous LLZO Membranes, ACS Appl Mater Interfaces (2023). https://doi.org/10.1021/acsami.3c14422.

[144] E. Yi, W. Wang, J. Kieffer, R.M. Laine, Flame made nanoparticles permit processing of dense, flexible, Li+ conducting ceramic electrolyte thin films of cubic-Li7La3Zr2O12 (c-LLZO), J Mater Chem A Mater 4 (2016). https://doi.org/10.1039/c6ta04492a.

[145] H. Li, Y. Liu, Y. Liu, Q. Zeng, K. Hu, Z. Lu, J. Liang, Effect of debinding temperature under an argon atmosphere on the microstructure and properties of 3D-printed alumina ceramics, Mater Charact 168 (2020). https://doi.org/10.1016/j.matchar.2020.110548.

[146] E.J. Cheng, A. Sharafi, J. Sakamoto, Intergranular Li metal propagation through polycrystalline Li6.25Al0.25La3Zr2O12 ceramic electrolyte, Electrochim Acta 223 (2017) 85–91. https://doi.org/10.1016/j.electacta.2016.12.018.

[147] L. Cheng, W. Chen, M. Kunz, K. Persson, N. Tamura, G. Chen, M. Doeff, Effect of surface microstructure on electrochemical performance of garnet solid electrolytes, ACS Appl Mater Interfaces 7 (2015) 2073–2081. https://doi.org/10.1021/am508111r.

[148] Z. Fu, D. McOwen, L. Zhang, Y. Gong, Y. Ren, J.E. Gritton, G. Godbey, J. Dai, L. Hu, E. Wachsman, Predicting the flexural strength of Li-ion-conducting garnet type oxide for solid-state-batteries, Journal of the American Ceramic Society 103 (2020) 5186–5195. https://doi.org/10.1111/jace.17177.

[149] R.A. Jonson, E. Yi, F. Shen, M.C. Tucker, Optimization of Tape Casting for Fabrication of Li 6.25 Al 0.25 La 3 Zr 2 O 12 Sheets, (n.d.). https://doi.org/10.1021/acs.energyfuels.1c00566.

[150] X. Huang, Z. Song, T. Xiu, M.E. Badding, Z. Wen, Sintering, micro-structure and Li + conductivity of Li 7−x La 3 Zr 2−x Nb x O 12 / MgO (x = 0.2-0.7) Li-Garnet composite ceramics, (2018). https://doi.org/10.1016/j.ceramint.2018.09.133.

[151] P. Adeli, J.D. Bazak, K.H. Park, I. Kochetkov, A. Huq, G.R. Goward, L.F. Nazar, Boosting Solid-State Diffusivity and Conductivity in Lithium Superionic Argyrodites by Halide Substitution, Angewandte Chemie - International Edition 58 (2019). https://doi.org/10.1002/anie.201814222.

Appendix

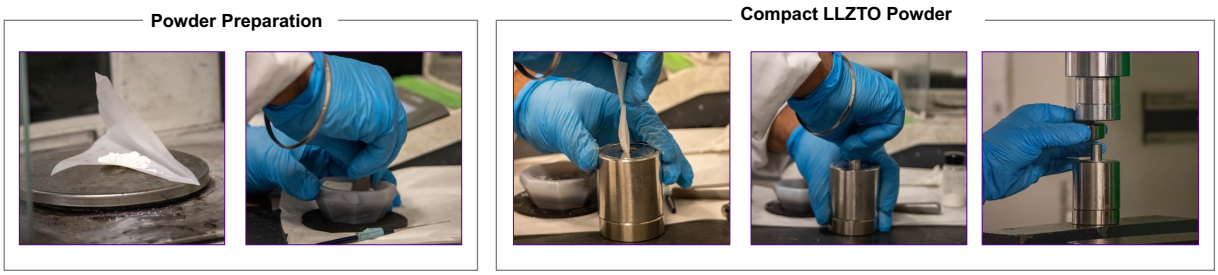

Figure A1: Optical images of powder preparation, and compaction using uniaxial dry pressing to create a bulk LLZTO pellet.

Figure A2: Optical images of sintered LLZTO bulk pellet with uneven sintering (left) and broken brittle bulk pellet (right).

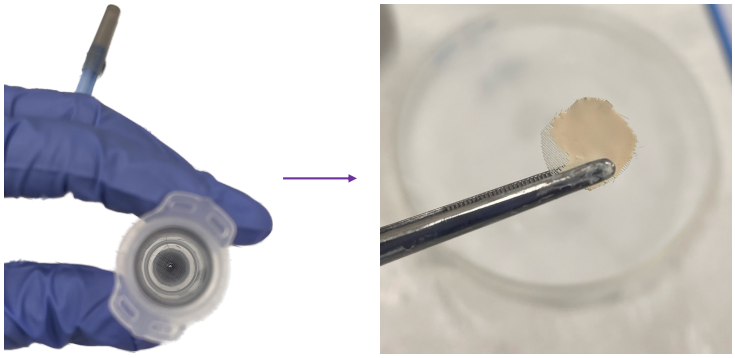

Figure A3: Optical images of 250 µm mesh placed within the syringe to filter large agglomerates (left) and used mesh (right).

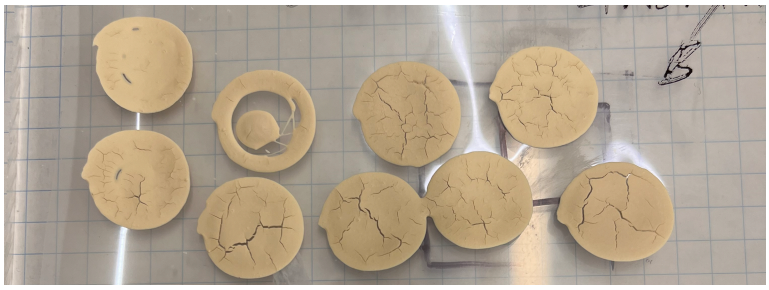

Figure A4: Optical images printed ceramic electrolytes cracked during drying.

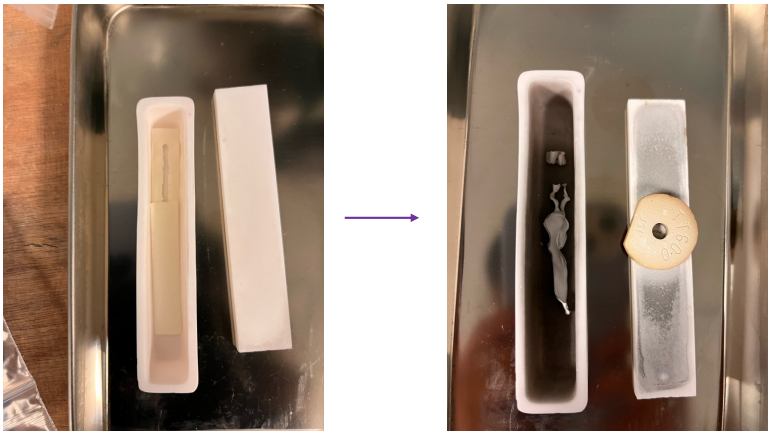

Figure A5: Optical images of LLZTO rectangular green body sheet (left) and sintered LLZTO rectangular sheet (right) in an alumina boat crucible. Photographs show significant warping of the thin sheets. The black contamination in/on alumina crucible is possible contamination from other materials in the tube furnace.

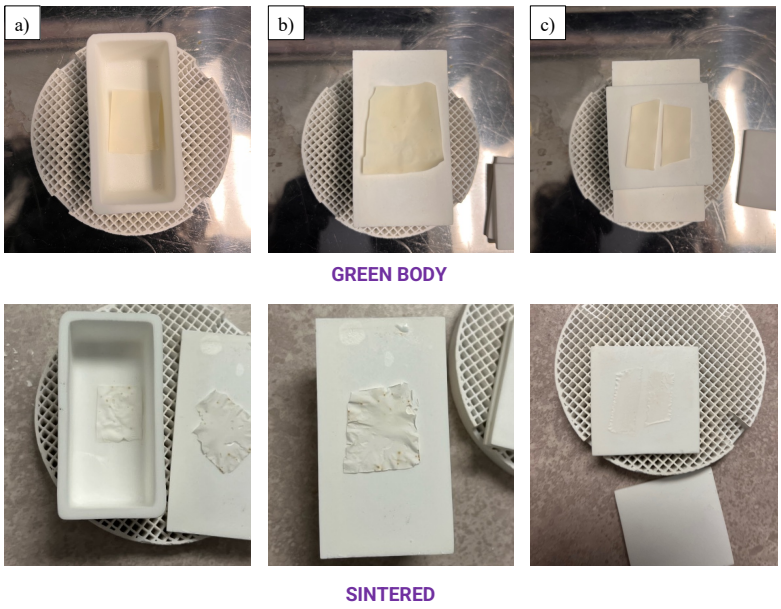

Figure A6: Optical images of LLZTO rectangular green body sheets a) placed within MgO crucible, and b-c) sandwiched between MgO plate. Warping is noticed due to small spaces between MgO plates. Thinner sheets can be seen adhering to MgO plate due to reactions between MgO plate and LLZTO SE (c).

Figure A7: Optical images of warping and cracking LLZO solid electrolyte sintering challenges. A flatter ceramic is observed after implementing a pressing and cutting step to pack solid particles together and cutting thinner edges out.

Figure A8: Optical image of MgO sandwich sintering technique within the 12mL MgO crucible.

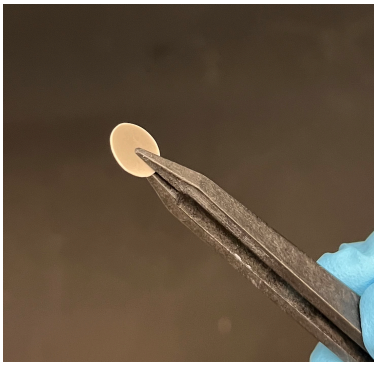

Figure A9: Optical images of sintered LLZTO ceramic electrolyte.